Disordered Fermi-Pasta-Ulam-Tsingou Lattices and q-Statistics

Zulkarnain

A thesis submitted for the degree of
Doctor of Philosophy

School of Mathematics, Statistics and Actuarial Science
University of Essex
October 2023

I would like to dedicate this PhD thesis to my loving parents,
my wife, my son, and my daughter

Declaration

The work in this thesis is based on research carried out with my supervisors Dr Chris G. Antonopoulos at the Department of Mathematical Sciences, University of Essex, United Kingdom and Prof Hadi Susanto at the Department of Mathematics, Khalifa University, United Arab Emirates. No part of this thesis has been submitted elsewhere for any other degree or qualification, and it is all my own work, unless referenced, in the text.

Zulkarnain
February 2024

Acknowledgements

First and foremost, I praise the Almighty Allah, the most beneficent and most merciful, whose guidance and blessings have been a source of strength to accomplish this thesis.

I would like to extend my deepest gratitude to my dedicated thesis supervisors, Dr Chris Antonopoulos and Prof Hadi Susanto, for their unwavering guidance, invaluable insights, and continuous support throughout my research journey. Their expertise and mentorship have been instrumental in shaping this thesis. Besides thanking my supervisors, I would like to thank Dr Murat Akman, Chair of the Supervisory Panel Board, for his consistent encouragement and insightful feedback, which have ensured that my research remained on a productive course. My sincere thanks also goes to my internal examiner Prof. Abdellah Salhi and my external examiner Dr. Helen Christodoulidi, for the advice, kindness and constructive questions.

I am fortunate to have some amazing friends, to whom I am indebted for their help and support through the highs and lows that are an inevitable part of research. Particular thanks go to Abdullahi M Jingi, Garga, Huseyin Yildirim, and Anthony Miller. I would also like to thank Rifqy Hakimi, M Izwan Heroza, *mas* Arief, and *Pak* Roman Cahaya for their help and warm brotherhood, which made our stay in the lovely city of Colchester more delightful.

Next, I must express my sincere thanks and respect to my parents, for their boundless love and unlimited support. Above all, the most heartfelt gratitude is to my beloved wife , Wice Purwani Suci, for her total moral support, passion and companionship.

I extend my sincere appreciation to BPPLN Dikti for providing financial support, which made it possible for me to pursue my academic endeavours and complete this thesis.

Publications

Most of the work of this thesis has been published or is going to be submitted for publication.

- Parts of Chapter 3 in this thesis have been published in :
  Zulkarnain, H. Susanto, C. G. Antonopoulos. Energy-recurrence breakdown and chaos in disordered Fermi–Pasta–Ulam–Tsingou lattices. *Chaos, Solitons and Fractals*, vol. 165, p. 112850, 2022.
- Parts of Chapter 4 in this thesis have been submitted to :
  Zulkarnain, H. Susanto, C. G. Antonopoulos. Disordered FPUT-α Hamiltonian lattices: Recurrence breakdown and chaotic behavior. Submitted to *Chaos, Solitons and Fractals*.

Contents

Chapter 1

Introduction

1.1 Fermi-Pasta-Ulam-Tsingou (FPUT) lattices

The Fermi-Pasta-Ulam-Tsingou (FPUT) recurrence phenomenon refers to an unexpected observation made during a numerical experiment in the early 1950s by physicists Enrico Fermi, John Pasta, and Stanislaw Ulam with Maria Tsingou's help. The FPUT experiment was conducted at the Los Alamos National Laboratory as an attempt to understand how energy is shared among the different modes of a vibrating one-dimensional lattice. It was conducted using the MANIAC (Mathematical Analyzer, Numerical Integrator, and Computer), which was one of the earliest digital computers, specifically designed for scientific calculations [1].

Fermi et al. initially aimed at exploring the problem of thermalisation and energy equipartition in an idealised lattice system. They considered a one-dimensional chain of particles connected by nonlinear springs. They hypothesised that the system, when given sufficient time to evolve, would exhibit the phenomenon of equipartition of energy, where the energy would be evenly distributed among all normal modes of vibration, resembling thermal equilibrium.

To their surprise, when they performed numerical simulations of the FPUT system, they found that the energy did not evenly distribute among the modes as expected. Instead, the energy showed complex behaviour, with occasional periods of recurrence where the system revisited its initial state, resembling the phenomenon of a recurrence or return of the initial conditions.

The recurrence phenomenon observed in the FPUT system challenged the prevailing notion at the time that systems with many degrees of freedom would naturally approach thermal equilibrium and exhibit energy equipartition. Energy equipartition is a principle in statistical mechanics that states, for a system in thermal equilibrium, the average energy is equally distributed among all degrees of freedom. Energy equipartition is expected over long periods if the system is ergodic. Ergodic behaviour refers to a property of a dynamic system where, over time, the system explores and visits all possible states with equal probability. In an ergodic system, time averages of observables are equal to their ensemble averages. The unexpected result sparked significant interest and debate within the scientific community [2–4]. The recurrence observed in the FPUT system shows that the system periodically returns to a state where energy is localised in specific modes rather than being uniformly distributed.

The phenomenon of recurrence in the Fermi-Pasta-Ulam-Tsingou (FPUT) lattice was explained by Zabusky and Kruskal [5] in real space. They demonstrated that by considering the continuum limit of the FPUT lattice, the integrable Korteweg-de Vries (KdV) equation can be derived. This derivation provided insights into the underlying dynamics that lead to the recurrence behaviour observed in the FPUT system.

When energy is introduced into a specific normal mode with a wave number k, it corresponds to initialising the system with a sinusoidal initial condition in real space. As time progresses, the state of the system evolves and breaks into a series of localised solutions, known as solitons. These solitons are self-reinforcing waves that maintain their shape and move through the system without dissipating or dispersing.

In the FPUT lattice, the solitons interact with the fixed ends or boundaries of the system. When a soliton reaches a boundary, it reflects or bounces back, eventually returning to its initial position. This interaction with the boundaries gives rise to the recurrence phenomenon observed in the FPUT system. The solitons, after bouncing back, continue to propagate and interact with each other, leading to complex dynamics and recurring patterns in the system.

Further investigations into the FPUT recurrence phenomenon revealed that the nonlinearity of the interparticle interactions played a crucial role in the system's behaviour. The FPUT system exhibited a rich dynamics with the coexistence of regular and chaotic motion. The FPUT lattice system exhibits chaotic behaviour under certain conditions. Chaos in a dynamical system refers to the sensitivity of the system's dynamics to small changes in initial conditions, leading to unpredictable and highly divergent trajectories over time.

The chaotic nature of the FPUT lattice system was unexpected, as it initially seemed to suggest the possibility of reaching thermal equilibrium. However, the recurrence phenomenon observed in the system indicated a more intricate dynamics that goes beyond simple periodic behaviour. Chaos in the FPUT lattice arises due to the interplay between nonlinearities, multiple degrees of freedom, and energy exchange among different modes. In [6, 7], the behaviour of the FPUT lattice system was examined under varying energy levels and different initial conditions.

The chaotic behaviour of the FPUT system has been extensively studied using numerical computations of chaotic indicators, such as Lyapunov exponents [8] and Smaller Alignment Index (SALI) [9]. They are commonly employed to characterise and quantify the chaotic properties of the system.

The FPUT lattice system also displays the intriguing phenomenon of super recurrence, where the system exhibits recurrence behaviour on significantly longer timescales than those observed in standard recurrence patterns. This phenomenon was reported by M. Tsingou, who was involved in the original FPUT experiment [10]. The research presented in [11] expands upon the previous work and investigates the breakdown of super recurrences as the initial energy and corresponding nonlinear parameters are systematically increased. They find that for the FPUT-α lattice, the super-recurrences break down while the lattice is still in the metastable state, a temporary state that the system can assume during its evolution that is not in thermal equilibrium but can persist for an extended period before eventually transitioning to a different state.

The lifetime of a metastable state in the FPUT lattice system can vary depending on several factors, including the system's energy, the initial conditions, and the nonlinearities present in the system [12]. In this state, the FPUT-α system can be considered as a perturbation of the integrable and regular Toda lattice [13].

1.2 q-Statistics

In the study of dynamical systems, one approach to understanding their behaviour is through statistical analysis. The behaviour of a dynamical system can be characterised statistically by examining the distribution of a relevant statistical variable that is generated from the system's trajectories. By analysing the distribution of this statistical variable, we can gain information about the behaviour and properties of the system. The distribution describes how the values of the statistical variable are spread out or distributed over a range of possible values.

The statistical distribution plays a crucial role in understanding the properties of a dynamical system. In certain systems, the statistical variable derived from the trajectories of the system can exhibit a normal distribution, commonly known as a Gaussian distribution or a bell curve. This phenomenon arises due to the mixing and ergodic nature of the system [14].

The Central Limit Theorem [15] provides further insight into this behaviour. It states that when a system is mixing, the statistical variable generated from its trajectory can be treated as a random variable. As a result, for a large number of trajectories, the probability distribution of this random variable approximates a Gaussian function.

However, in other cases, the distribution may deviate from a normal distribution and exhibit non-Gaussian features. These deviations can indicate the presence of complex dynamics and show a sign of nonergodicity. For this system, the distribution is well approximated by a q-Gaussian distribution [14, 16–19].

1.3 Thesis overview

The two primary goals of this thesis are (a) to investigate the FPUT-α system with variability and their chaotic behaviour, and (b) to investigate the chaotic dynamics of the standard map using q-statistics.

In chapter 2, we provide an overview of previous research related to these topics and present the numerical tools that will be utilised in subsequent chapters. In chapter 3, we examine the influence of variability in the nonlinear coupling terms of the FPUT-α system to the localisation of normal mode energy and the occurrence of blow-up solutions within a finite time. Through the application of multiple time-scale expansions, we derived a two normal-mode approximation to explain energy recurrence breakdown and solution blow-up in finite time beyond a certain variability threshold. This study is followed in chapter 4 by introducing the variability in the FPUT-α Hamiltonian and study the system at a fixed energy level. By maintaining the Hamiltonian function of the system, we are able to initiate the system at the same energy level while varying the degree of variability up to 100%.

In Chapter 5, our focus turns to understanding the chaos exhibited by the standard map by analysing the distribution of a probability distribution function derived from the system's trajectories. We examine various chaotic properties of the standard map through this approach. Specifically, we investigate trajectories originating from both the stability island and the chaotic sea regions. To identify the probability distribution function of these trajectories, we employ the q-Gaussian distribution. This distribution offers a suitable framework for characterising the complex behaviour observed in chaotic systems. To obtain the parameters of the distribution, we develop a procedure that utilises a genetic algorithm. This algorithm allows us to solve a multi-objective optimisation problem, enabling us to determine the optimal parameters that best describe the probability distribution function of the trajectories. We conclude our study in Chapter 6 where we also discuss future work.

Chapter 2

Literature review

2.1 Hamiltonian systems

A Hamiltonian system is a dynamical system governed by Hamilton's equations of motion. It is a mathematical formalism developed by Hamilton to describe the evolution of physical systems where their energy is being conserved in time. A Hamiltonian system's behaviour can be described by its Hamiltonian function H. This function captures its total energy, typically expressed as generalised coordinates and moments.

Mechanical systems are a subset of Hamiltonian system that can be defined as the sum of kinetic and potential energies when energy is conserved, where each term depends on generalised coordinates $\boldsymbol{q}(t)$ and momenta $\boldsymbol{p}(t)$, as follow

$$H(t,\boldsymbol{q}(t),\boldsymbol{p}(t)) = T(\boldsymbol{q}(t),\boldsymbol{p}(t)) + V(\boldsymbol{q}(t)). \tag{2.1}$$

The generalised coordinates q represent independent variables which define the configuration of a system, such as position or angle. Moments represent conjugate variables associated with generalised coordinates that reflect its velocity properties.

To analyse the Hamiltonian system, one needs to study the corresponding Hamilton's equations of motion. These equations consist of coupled first-order ordinary differential equations which govern the time evolution of generalised coordinates and momenta, given by

$$\frac{d\boldsymbol{q}}{dt} = \frac{\partial H}{\partial \boldsymbol{p}}$$
$$\frac{d\boldsymbol{p}}{dt} = -\frac{\partial H}{\partial \boldsymbol{q}}$$

where $\boldsymbol{q} = (q_1, q_2, \ldots, q_N)$, $\boldsymbol{p} = (p_1, p_2, \ldots, p_N)$ are called the position and momentum, respectively, and $H = H(t, \boldsymbol{q}, \boldsymbol{p})$ is the Hamiltonian function. These equations describe how coordinates and momenta change over time to form the trajectory in phase space, where every point represents one state of a system. We also define N as the degree of freedom of the Hamiltonian system (2.1). The phase space of a Hamiltonian system can be conceptualised as a multi-dimensional space whereby each individual point corresponds to a distinct combination of coordinates and momenta. The time evolution of the system can be represented by a trajectory or orbit within the phase space. A Hamiltonian system characterised by N degrees of freedom exhibits a phase space dimension of $2N$.

Hamiltonian systems exhibit various important properties, such as conservation of energy and symplecticity, that stem from their mathematical structure. This makes the Hamiltonian framework particularly effective at studying conservative systems such as those in classical and celestial mechanics.

If the Hamiltonian H does not depend explicitly on t (autonomous system), then its value along any trajectories is constant. Indeed, direct calculations using the chain rule give

$$\begin{aligned}\frac{dH}{dt} &= \frac{\partial H}{d\boldsymbol{q}}\frac{d\boldsymbol{q}}{dt} + \frac{\partial H}{d\boldsymbol{p}}\frac{d\boldsymbol{p}}{dt} \\ &= \frac{\partial H}{d\boldsymbol{q}}\frac{\partial H}{d\boldsymbol{p}} + \frac{\partial H}{d\boldsymbol{p}}\left(-\frac{\partial H}{d\boldsymbol{q}}\right) = 0.\end{aligned}$$

Therefore, $H(\boldsymbol{q}(0),\boldsymbol{p}(0)) = H(\boldsymbol{q}(t),\boldsymbol{p}(t)) = E$, where E is called the energy of the system.

Hamiltonian systems find many uses across disciplines such as physics, engineering and applied mathematics. They play a fundamental role in understanding the dynamics of many physical systems ranging from simple harmonic oscillators to those with many degrees of freedom.

2.2 Coupled oscillators

One-dimensional (1D) systems of coupled oscillators refer to an assembly of oscillators arranged linearly along one dimension that interact with their nearest neighbors. Such systems often serve as simplified models to study how coupled oscillators influence physical phenomena. Each oscillator can be described by its position and momentum, denoted q_i and p_i, for oscillators 1 through n, using equations of motion from either Hamiltonian formalism or Newton's laws of motion.

These equations of motion describe how the positions q_i and momenta p_i of oscillators change with time, taking into account interactions with neighboring oscillators. Solving these equations allows us to study various phenomena related to system behaviour such as propagation of waves, energy transfer or synchronisation phenomena in detail.

The 1D n coupled-oscillator system serves as a simplified model to better understand more complex systems such as vibrating strings, crystal lattices or coupled pendulums. This gives insight into phenomena like wave propagation, resonance and collective behaviour caused by interactions among oscillators, which has applications across disciplines, such as physics, engineering and materials science.

2.2.1 Systems of linear coupled oscillators

We consider the mass-spring system of N identical particles of mass m connected by springs with equal spring constant k. The Hamiltonian function of the system is

$$H(q,p) = \sum_{j=0}^{N} \frac{p_j^2}{2m} + \sum_{j=0}^{N} \frac{k}{2}\left(q_{j+1} - q_j\right)^2 = E,$$

where the two endpoints are kept fixed, i.e. $p_0 = 0$, $x_0 = x_{N+1} = 0$, and E is the constant energy of the system. The equations of motion are given by

$$\ddot{q}_j = \left(q_{j-1} - 2q_j + q_{j+1}\right), \tag{2.2}$$

where we have taken $k/m = 1$ for simplicity.

Introducing the following transformations

$$\boldsymbol{q} = A\boldsymbol{Q}, \quad \boldsymbol{p} = A\boldsymbol{P}, \tag{2.3}$$

where $\boldsymbol{q} = [q_1\, q_2\, \ldots\, q_N]^T$, $\boldsymbol{p} = [p_1\, p_2\, \ldots\, p_N]^T$, $\boldsymbol{Q} = [Q_1\, Q_2\, \ldots\, Q_N]^T$, $\boldsymbol{P} = [P_1\, P_2\, \ldots\, P_N]^T$, and

$$A = \sqrt{\frac{2}{N+1}} \begin{bmatrix} \sin\left(\frac{\pi}{N+1}\right) & \sin\left(\frac{2\pi}{N+1}\right) & \ldots & \sin\left(\frac{N\pi}{N+1}\right) \\ \sin\left(\frac{2\pi}{N+1}\right) & \sin\left(\frac{4\pi}{N+1}\right) & \ldots & \sin\left(\frac{2N\pi}{N+1}\right) \\ \vdots & \vdots & \ddots & \vdots \\ \sin\left(\frac{N\pi}{N+1}\right) & \sin\left(\frac{2N\pi}{N+1}\right) & \ldots & \sin\left(\frac{N^2\pi}{N+1}\right) \end{bmatrix},$$

Eq. (2.2) can be written as

$$A\ddot{\boldsymbol{Q}} = SA\boldsymbol{Q}, \tag{2.4}$$

where

$$S = \begin{bmatrix} -2 & 1 & 0 & \ldots & 0 \\ 1 & -2 & 1 & & 0 \\ \vdots & & \ddots & & \vdots \\ 0 & 0 & \ldots & 1 & -2 \end{bmatrix}. \tag{2.5}$$

According to [20], the eigenvalues λ_k of matrix S given in Eq. (2.5), in decreasing order are

$$\lambda_k = -4\sin^2\left(\frac{k\pi}{N+1}\right),\ k = 1, 2, \cdots, N.$$

By direct computations, it can be shown that

$$SA = AD, \tag{2.6}$$

where

$$D = \begin{bmatrix} \lambda_1 & 0 & \dots & 0 \\ 0 & \lambda_2 & & 0 \\ \vdots & & \ddots & \vdots \\ 0 & 0 & \dots & \lambda_N \end{bmatrix}.$$

Therefore, using Eq. (2.6) in the equations of motion (2.4), we obtain

$$\ddot{\boldsymbol{Q}} = D\boldsymbol{Q}. \tag{2.7}$$

Note that Eq. (2.7) is a system of uncoupled harmonic oscillators and can be solved analytically as it is a linear system of ordinary differential equations. This simplification is made possible due to the transformation given in Eq. (2.3). This transformation is known as normal mode transformation and plays an important rule in studying the one-dimensional lattices. It is worth noting that Eq. (2.7) admits the Hamiltonian function

$$H = \frac{1}{2}\sum_{k=1}^{N}\left(P_k^2 + \omega_k^2 Q_k^2\right),$$

where

$$\omega_k = 2\sin\left(\frac{k\pi}{2(N+1)}\right),\ k = 1,2,\cdots,N.$$

Variables P_k and Q_k are called the normal mode coordinates, and ω_k are the normal mode frequencies. Moreover, we can also define the normal mode energy for mode k as

$$E_k = \frac{1}{2}\left(P_k^2 + \omega_k^2 Q_k^2\right).$$

Hence, the total energy of the system is equal to the sum of the energies from each individual modes.

In Chapters 3 and 4, our focus will be on the examination of normal mode energy within a particular Hamiltonian system, namely the Fermi-Pasta-Ulam-Tsingou-α (FPUT-α) system. We will delve into the details of this system to better understand its normal mode energy behaviour.

2.3 Symplectic integrators

The sum of the projected areas on the N $(p_i, q_i), i = 1, \ldots, N$ planes is preserved by the flow of a Hamiltonian system with N degrees of freedom. This structure is called symplectic structure and defined by the non-degenerate closed 2-form

$$\omega = d\mathbf{p} \wedge d\mathbf{q},$$

which is also known as the wedge product [21]. The wedge product of two arbitrary vectors $\mathbf{u}, \mathbf{v}$ of the phase space is defined by the operation

$$\mathbf{u} \wedge \mathbf{v} = (\mathbf{u}\mathbf{J}, \mathbf{v}),$$

where

$$\boldsymbol{J} = \begin{bmatrix} 0 & \boldsymbol{I} \\ -\boldsymbol{I} & 0 \end{bmatrix}.$$

with $\mathbf{0}$ and the unitary matrix $\mathbf{I}$ are $N \times N$ blocks. Matrix J is known as the standard symplectic matrix. A canonical transformation $\mathcal{T} : X \to X$ on a $2N$-dimensional manifold X with coordinates $\mathbf{x} = (\mathbf{q}, \mathbf{p})$ is a transformation which satisfies

$$(D\mathcal{T})^T \mathbf{J} D\mathcal{T} = \mathbf{J},$$

where $D\mathcal{T}$ is the Jacobian matrix of $\mathcal{T}$ and T denotes the transpose operation [21].

Symplectic integrators are numerical integration methods designed to preserve the symplectic structures of Hamiltonian systems derived from Hamilton's equations of motion. Such conservative systems feature energy conservation dynamics. To obtain a symplectic integrator, we need to find a canonical transformation which takes a set of variables $(\mathbf{p}_0, \mathbf{q}_0)$ at $t = 0$, to another set $(\mathbf{p}, \mathbf{q})$ at time t.

Standard numerical integration methods such as Runge-Kutta [22] may introduce errors that grow in time and compromise long-term simulation accuracy, whereas symplectic integrators aim to maintain important properties of Hamiltonian systems such as energy conservation and phase space volume preservation through long-term simulation.

Symplectic integrators ensure this preservation through specific algorithms designed to take advantage of Hamiltonian systems' underlying symplectic structure and maintain their symplecticity, so as to maintain close proximity between solution paths in phase space and true trajectories.

Symplectic integrators offer numerous advantages over classical methods for modeling Hamiltonian systems such as improved long-term accuracy, the preservation of important physical properties, and long-term simulation without significant energy drift or phase space distortion.

It is important to take into account that although symplectic integrators provide advantages when simulating Hamiltonian systems of the form $H = T + V$, where T is the kinetic and V the potential energies, their accuracy may not compare favourably with non-symplectic methods when simulating general dynamical systems which are not Hamiltonian. Therefore, the integration method chosen will be determined by the type of the system that needs to be simulated.

Consider the autonomous Hamiltonian function which can be expressed as

$$H(\boldsymbol{p},\boldsymbol{q}) = T(\boldsymbol{p}) + V(\boldsymbol{q}), \tag{2.8}$$

where $T(\boldsymbol{p})$ is the kinetic energy, $V(\boldsymbol{q})$ is the potential energy, and

$$\boldsymbol{q} = (q_1, q_2, \ldots, q_N), \quad \boldsymbol{p} = (p_1, p_2, \ldots, p_N),$$

are the generalised coordinates and momenta, respectively. Hamilton's equations of motion can be written as

$$\frac{d\boldsymbol{x}}{dt} = \boldsymbol{J}\frac{\partial H}{\partial \boldsymbol{x}}, \tag{2.9}$$

where

$$\boldsymbol{J} = \begin{bmatrix} 0 & \boldsymbol{I} \\ -\boldsymbol{I} & 0 \end{bmatrix},$$

with $\boldsymbol{I}$ is the identity matrix and $\boldsymbol{x} = (\boldsymbol{q}, \boldsymbol{p})$. The Poisson bracket in the standard form is defined as

$$\{u, v\} = \frac{\partial u}{\partial q_i}\frac{\partial v}{\partial p_i} - \frac{\partial u}{\partial p_i}\frac{\partial v}{\partial q_i}. \tag{2.10}$$

Therefore, by using the chain rule for derivative, the equations of motion, which is given by Eq. (2.9), become

$$\begin{aligned} \frac{d\boldsymbol{x}}{dt} &= \frac{\partial \boldsymbol{x}}{\partial \boldsymbol{q}}\frac{d\boldsymbol{q}}{dt} + \frac{\partial \boldsymbol{x}}{\partial \boldsymbol{p}}\frac{d\boldsymbol{p}}{dt} \\ &= \frac{\partial \boldsymbol{x}}{\partial \boldsymbol{q}}\frac{\partial H}{\partial \boldsymbol{p}} - \frac{\partial \boldsymbol{x}}{\partial \boldsymbol{p}}\frac{\partial H}{d\boldsymbol{q}} \\ &= \{\boldsymbol{x}, H\} \end{aligned} \tag{2.11}$$

Introducing the differential operator

$$D_H \boldsymbol{x} = \{\boldsymbol{x}, H\},$$

Eq. (2.11) becomes

$$\frac{d\boldsymbol{x}}{dt} = D_H \boldsymbol{x},$$

which can be integrated formally from $t = 0$ to $t = \tau$ to obtain

$$\boldsymbol{x} = \exp(\tau D_H)\, \boldsymbol{x}_0.$$

When the Hamiltonian has the form of Eq. (2.8), we note that

$$D_H = D_T + D_V,$$

where

$$D_T \boldsymbol{x} = \{\boldsymbol{x}, T(\boldsymbol{p})\},$$

$$D_V \boldsymbol{x} = \{\boldsymbol{x}, V(\boldsymbol{q})\}.$$

Hence, the formal solution becomes

$$\boldsymbol{x} = \exp\left(\tau\left(D_T + D_V\right)\right)\boldsymbol{x}_0. \tag{2.12}$$

The differential operators D_T and D_V are, in general, non commutative operators. To solve Eq. (2.12), we seek a set of real numbers a_i, b_i, $i = 1, 2, \cdots, k$ such that

$$\exp\left(\tau\left(D_T + D_V\right)\right) = \prod_{i=1}^{k} \exp\left(a_i \tau D_T\right) \exp\left(b_i \tau D_V\right) + O\left(\tau^{n+1}\right)$$

Therefore, we have

$$\boldsymbol{x} = \prod_{i=1}^{k} \exp\left(a_i \tau D_T\right) \exp\left(b_i \tau D_V\right) \boldsymbol{x}_0 + O\left(\tau^{n+1}\right), \tag{2.13}$$

for a particular integer n [23]. In this context, n is called the order of the symplectic integrator. The approximation to Eq. (2.13) is then given by

$$\boldsymbol{x} = \prod_{i=1}^{k} \exp\left(a_i \tau D_T\right) \exp\left(b_i \tau D_V\right) \boldsymbol{x}_0, \tag{2.14}$$

which is exact up to order n ($O(\tau^n)$). It should be noted that the value of k is not necessarily the same as n in Eq. (2.14). For $n = 1$ or the first-order symplectic integrator, the coefficients are $a_1 = b_1 = 1$. This integrator is known as the symplectic Euler method [24]. The second-order method is called the Verlet method [24] with $a_1 = a_2 = 1/2, b_1 = 1$ and $b_2 = 0$. The third-order method was obtained in [25] with

$$a_1 = \frac{1}{24}, \quad a_2 = \frac{3}{4}, \quad a_3 = -\frac{1}{24}, \quad b_1 = \frac{2}{3}, \quad b_2 = -\frac{2}{3}, \quad b_3 = 1.$$

Yoshida in [26] proposed a procedure to obtain the coefficients of the integrator with even orders up to 8th order. For easy reference, the coefficients for the fourth order integrator are given by

$$\begin{aligned} a_1 &= \tfrac{1}{2(2-2^{1/3})}, \quad a_2 = \tfrac{1-2^{1/3}}{2(2-2^{1/3})}, \quad a_3 = a_2, \quad a_4 = a_1, \\ b_1 &= \tfrac{1}{2-2^{1/3}}, \quad b_2 = -\tfrac{2^{1/3}}{2-2^{1/3}}, \quad b_3 = 0, \quad b_4 = b_1. \end{aligned} \tag{2.15}$$

Next, we explain how to compute the solutions to Eq. (2.14). Since

$$\begin{aligned} D_T\boldsymbol{x} &= \{\boldsymbol{x}, T\} \\ &= \frac{\partial \boldsymbol{x}}{\partial q_i}\frac{\partial T}{\partial p_i} - \frac{\partial \boldsymbol{x}}{\partial p_i}\frac{\partial T}{\partial q_i} \\ &= (\dot{q}_i, 0) \end{aligned}$$

and

$$\begin{aligned} D_T^2\boldsymbol{x} &= \{\{\boldsymbol{x},T\},T\} \\ &= \{(\dot{q}_i,0),T\} \\ &= (0,0) \end{aligned}$$

for all $\boldsymbol{x}$, we conclude that

$$D_T^j\boldsymbol{x} = 0 \tag{2.16}$$

for all $j \geq 2$. Similarly, we also have

$$D_V^j\boldsymbol{x} = 0 \tag{2.17}$$

for all $j \geq 2$. By using Eqs. (2.16) and (2.17) in the Taylor series expansions of $\exp(a_i\tau D_T)$ and $\exp(b_i\tau D_V)$, respectively, we get

$$\begin{aligned} \exp(a_i\tau D_T) &= 1 + a_i\tau D_T, \\ \exp(b_i\tau D_V) &= 1 + b_i\tau D_V. \end{aligned}$$

Therefore, Eq. (2.13) can be numerically calculated by applying sequentially two transformations at each step i in the expansion of Eq. (2.14), which evolves the initial vector $\boldsymbol{x}_j = (\boldsymbol{q}_j, \boldsymbol{p}_j)$ at time t_j to its final state $\boldsymbol{x}_{j+1} = (\boldsymbol{q}_{j+1}, \boldsymbol{p}_{j+1})$ at time $t_{j+1} = t_j + \tau$ according to the following steps: We first set $\boldsymbol{q}_j^{old} = \boldsymbol{q}_j$ and $\boldsymbol{p}_j^{old} = \boldsymbol{p}_j$, then we perform the following computations

$$\boldsymbol{q}_{j+1}^{new} = \boldsymbol{q}_j^{old} + a_i\tau\left(\frac{dT}{d\boldsymbol{p}}\right)_{\boldsymbol{p}=\boldsymbol{p}_j^{old}} \tag{2.18}$$

$$\boldsymbol{p}_{j+1}^{new} = \boldsymbol{p}_j^{old} - b_i\tau\left(\frac{dV}{d\boldsymbol{q}}\right)_{\boldsymbol{q}=\boldsymbol{q}_{j+1}^{new}} \tag{2.19}$$

for $i = 1,2,\ldots,k$, replacing $\boldsymbol{q}_j^{old}$ and $\boldsymbol{p}_j^{old}$ with $\boldsymbol{q}_{j+1}^{new}$ and $\boldsymbol{p}_{j+1}^{new}$, respectively, after each i. In Algorithm 1, we present the algorithm for the symplectic integrator that will be used throughout this work. In particular, we use the fourth-order symplectic integration where the coefficients are given in Eq. (2.15).

Algorithm 1 Symplectic integrator.

Input: Hamiltonian function $H = T + V$, initial condition $(\boldsymbol{q}_0, \boldsymbol{p}_0)$, integration step size τ, final integration time T, symplectic integrator coefficients (a_i, b_i), $i = 1,2,\ldots,k$

Output: Time evolution of $(\boldsymbol{q}_j, \boldsymbol{p}_j)$.

```
$\boldsymbol{q}_0^{old} \leftarrow \boldsymbol{q}_0$
$\boldsymbol{p}_0^{old} \leftarrow \boldsymbol{p}_0$
for $j = 0$ to $\frac{T}{\tau} - 1$ do
    for $i = 1$ to $k$ do
        compute
            $\boldsymbol{q}_{j+1}^{new} = \boldsymbol{q}_j^{old} + a_i\tau\left(\frac{dT}{d\boldsymbol{p}}\right)_{\boldsymbol{p}=\boldsymbol{p}_j^{old}}$
        compute
            $\boldsymbol{p}_{j+1}^{new} = \boldsymbol{p}_j^{old} - b_i\tau\left(\frac{dV}{d\boldsymbol{q}}\right)_{\boldsymbol{q}=\boldsymbol{q}_{j+1}^{new}}$
        $\boldsymbol{q}_j^{old} \leftarrow \boldsymbol{q}_{j+1}^{new}$
        $\boldsymbol{p}_j^{old} \leftarrow \boldsymbol{p}_{j+1}^{new}$
    end for
    $\boldsymbol{q}_{j+1} \leftarrow \boldsymbol{q}_{j+1}^{new}$
    $\boldsymbol{p}_{j+1} \leftarrow \boldsymbol{p}_{j+1}^{new}$
    $\boldsymbol{q}_{j+1}^{old} \leftarrow \boldsymbol{q}_{j+1}$
    $\boldsymbol{p}_{j+1}^{old} \leftarrow \boldsymbol{p}_{j+1}$
end for
```

2.4 Chaotic indicators

Dynamical systems employ chaotic indicators as measures or quantities that provide information about their disordered nature, which typically manifests itself through extreme sensitivity to initial conditions, irregular and unpredictable motion, and the absence of long-term regular patterns. Chaotic indicators serve to measure and identify chaos in dynamical systems. They provide insight into its inherent unpredictability by providing information about its complex behaviour.

In this PhD thesis, we use two chaotic indicators, namely the maximum Lyapunov exponent (mLE) and the Smaller Alignment Index (SALI). Both of these indicators depend on the evolution of deviation vectors, which are governed by variational equations. Therefore, we will begin with a discussion of the variational equations of a Hamiltonian system. Then, we will give a brief overview of mLE and SALI, as well as the algorithm to compute them. We also discuss the numerical method for calculating the mLE and SALI. We present in the following the extraction from [27].

2.4.1 Variational equations

We consider an autonomous Hamiltonian system with N degrees of freedom which can be written as

$$H(\boldsymbol{q},\boldsymbol{p}) = E, \tag{2.20}$$

where $\boldsymbol{q} = (q_1,q_2,\ldots,q_N$ and $\boldsymbol{p} = (p_1,p_2,\ldots,p_N)$ represent the generalised coordinates and momenta, respectively, and E is the fixed energy of the system. We can define a trajectory in the $2N$ dimensional phase space $\mathcal{S}$ of this system by a vector

$$\boldsymbol{x}(t) = (\boldsymbol{q}(t), \boldsymbol{p}(t)) \tag{2.21}$$

where $x_i = q_i$, $x_{i+N} = p_i, i = 1, 2, \ldots, N$. The trajectory evolves in the phase space $\mathcal{S}$ according to Hamilton's equations of motion, which in matrix form can be written as

$$\dot{\boldsymbol{x}} = \boldsymbol{f}(\boldsymbol{x}) = \begin{bmatrix} \frac{\partial H}{\partial \boldsymbol{p}} & -\frac{\partial H}{\partial \boldsymbol{q}} \end{bmatrix}^T = \boldsymbol{J}_{2N} \cdot \boldsymbol{DH}, \tag{2.22}$$

with $\boldsymbol{q} = (q_1(t), q_2(t), \ldots, q_N(t)), \boldsymbol{p} = (p_1(t), p_2(t), \ldots, p_N(t))$, and

$$\boldsymbol{DH} = \begin{bmatrix} \frac{\partial H}{\partial q_1} & \frac{\partial H}{\partial q_2} \cdots \frac{\partial H}{\partial q_N} & \frac{\partial H}{\partial p_1} & \frac{\partial H}{\partial p_2} \cdots \frac{\partial H}{\partial p_N} \end{bmatrix}^T .$$

The matrix $\boldsymbol{J}_{2N}$ is given by

$$\boldsymbol{J}_{2N} = \begin{bmatrix} \boldsymbol{0}_N & \boldsymbol{I}_N \\ -\boldsymbol{I}_N & \boldsymbol{0}_N \end{bmatrix},$$

where $\boldsymbol{I}_N$ is the $N \times N$ identity matrix and $\boldsymbol{0}_N$ the $N \times N$ matrix with all its element equal to zero.

The solution to Eq. (2.22) is formally written as

$$\boldsymbol{x}(t) = \Phi^t(\boldsymbol{x}(0)),$$

for $\Phi^t : \mathcal{S} \to \mathcal{S}$. Let $\mathcal{T}_{\boldsymbol{x}}\mathcal{S}$ denotes the tangent space of the phase space $\mathcal{S}$. Let $\boldsymbol{w}$ denote the deviation vectors for a particular orbit of a dynamical system which evolve on the tangent space $\mathcal{T}_{\boldsymbol{x}}\mathcal{S}$. Let $d_{\boldsymbol{x}}\Phi^t$ denote the linear mapping which maps the tangent space of $\mathcal{S}$ at point $\boldsymbol{x}$ onto the tangent space at point $\Phi^t(\boldsymbol{x})$ so that

$d_{\boldsymbol{x}}\Phi^t : \mathcal{T}_{\boldsymbol{x}}\mathcal{S} \to \mathcal{T}_{\Phi^t(\boldsymbol{x})}\mathcal{S}$ is given by

$$\boldsymbol{w}(t) = d_{\boldsymbol{x}}\Phi^t \boldsymbol{w}(0),$$

where $\boldsymbol{w}(0), \boldsymbol{w}(t)$ are deviation vectors with respect to the reference orbit at times $t = 0$ and $t > 0$, respectively. For the Hamiltonian (2.20), an initial deviation vector $\boldsymbol{w}(0) = (\delta q_1(0), \cdots, \delta q_N(0), \delta p_1(0), \cdots, \delta p_N(0))$ from the solution $\boldsymbol{x}(t)$ in Eq. (2.21) evolves on the tangent space $\mathcal{T}_{\boldsymbol{x}}\mathcal{S}$ according to the following equations

$$\begin{aligned}\dot{\boldsymbol{w}} &= \boldsymbol{Df}(\boldsymbol{x}(t)) \cdot \boldsymbol{w} \\ &= \frac{\partial \boldsymbol{f}}{\partial \boldsymbol{x}}(\boldsymbol{x}(t)) \cdot \boldsymbol{w} \\ &= \left[\boldsymbol{J}_{2N} \cdot \boldsymbol{D}^2\boldsymbol{H}(\boldsymbol{x}(t))\right] \cdot \boldsymbol{w} \\ &= \boldsymbol{A}(t) \cdot \boldsymbol{w},\end{aligned} \tag{2.23}$$

where $\boldsymbol{D}^2\boldsymbol{H}(\boldsymbol{x}(t))$ is the Hessian matrix of the Hamiltonian (2.20) calculated at the reference orbit $\boldsymbol{x}(t)$ in Eq. (2.21). Equation (2.23) is called the variational equations of Hamiltonian (2.20) [27]. Furthermore, the variational equations (2.23) can be considered as the Hamiltonian equations of motion corresponding to the Hamiltonian function

$$H_V(\boldsymbol{\delta q}, \boldsymbol{\delta p}) = \frac{1}{2}\sum_{j=1}^{N} \delta p_i^2 + \frac{1}{2}\sum_{j,k}^{N} \boldsymbol{D^2V(q(t))}_{jk}\delta q_j \delta q_k. \tag{2.24}$$

The Hamiltonian function H_V provided in Eq. (2.24) is called the tangent dynamics Hamiltonian (TDH).

2.4.2 Lyapunov exponents

The Lyapunov exponents (LCEs) are asymptotic measures that characterise the average rate of growth (or shrinking) of infinitesimally close orbits of a dynamical system. Their concept was introduced by Lyapunov in the late 19th centuries when studying the stability of non-stationary solutions of ordinary differential equations [28], and has been widely employed in studying dynamical systems since then [29, 30]. All Lyapunov exponents are zero for regular orbits and there is at least one positive Lyapunov exponent for chaotic orbits. Indeed, an orbit can have at most n different Lyapunov exponents where n is the dimension of the phase- or state-space of a dynamical system. The set of all Lyapunov exponents is called the Lyapunov spectrum [30]. For a dynamical system which satisfies the Multiplicative Ergodic Theorem [27], the n possibly nondistinct Lyapunov exponents can be ordered in descending order $\lambda_1 \geq \lambda_2 \geq \cdots \geq \lambda_n$ and it is sufficient to compute only the maximal Lyapunov exponent λ_1 to determine whether the system is chaotic.

In any dynamical systems, it has been shown in [31] that at least one Lyapunov exponent vanishes. Furthermore, in the case of autonomous Hamiltonian systems of N degrees of freedom, the set of LCEs consists of pairs of values having opposite signs [32]

$$\lambda_i = -\lambda_{2N-i+1},\ i = 1,2,\ldots,N. \tag{2.25}$$

Therefore, for Hamiltonian systems at least two LCEs vanish, i.e.

$$\lambda_N = \lambda_{N+1} = 0,$$

and the sum of all LCEs is zero, i.e.

$$\sum_{i=1}^{2N} \lambda_i = 0,$$

because of Eq. (2.25).

To compute the Lyapunov exponents, we follow the evolution of the orbit $\boldsymbol{x}(t)$ and the unitary initial deviation vectors $\boldsymbol{w}(0)$ which respectively satisfy the equations of motion (2.22) and variational equations (2.23). The p-largest Lyapunov exponents λ_p, $p = 1, \ldots, 2N$ are approximated for $t \to \infty$ by

$$X_p(t) = \frac{1}{t} \sum_i \ln \gamma_{pi},$$

where ln is the natural logarithm. Hence,

$$\lambda_p = \lim_{t \to \infty} X_p(t) = \lim_{t \to \infty} \frac{1}{t} \sum_i \ln \gamma_{pi}.$$

In this context, γ_{pi}, $p = 1, \ldots, 2N$, $i = 1, \ldots,$ are the norms of the deviation vectors, which are orthogonalised successively at every time step h. In the case of regular orbits, the maximum Lyapunov exponent $\lambda_1(t)$ tends to zero following a power law t^{-1}, while it converges to a nonzero positive value in the case of chaotic orbits.

In this work, we calculate only the value of the maximum Lyapunov exponent, as this is sufficient to discriminate between regular and chaotic trajectories. We follow the standard method as described in [27] and present the procedure for computing the mLE in Algorithm 2.

To compute mLE, we follow the evolution of a trajectory starting at the initial point $\mathbf{x}(0) = (x_1(0),\ldots,x_N(0),q_1(0),\ldots,q_N(0))$, that evolves according to Hamilton's equations of motion

$$\dot{\mathbf{x}} = \mathbf{f}(\mathbf{x}) = \begin{bmatrix} \frac{\partial H}{\partial \mathbf{p}} & -\frac{\partial H}{\partial \mathbf{q}} \end{bmatrix}^T,$$

and the evolution of a deviation vector

$$\mathbf{w}(0) = (\delta x_1(0),\delta x_2(0),\ldots,\delta x_N(0),\delta q_1(0),\delta q_2(0),\ldots,\delta q_N(0)),$$

that evolves according to the variational equation

$$\dot{\mathbf{w}} = \frac{\partial \mathbf{f}}{\partial \mathbf{x}}(\mathbf{x}(t)) \cdot \mathbf{w}.$$

Then, mLE is defined as

$$\lambda = \lim_{t\to\infty} \frac{1}{t} \ln \frac{\|\mathbf{w}(t)\|}{\|\mathbf{w}(0)\|},$$

If mLE converges to zero following the law $1/t$ in a log log plot, then the trajectory is regular, whereas if it converges to a positive value in time, then the trajectory is chaotic [27].

2.4.3 The Smaller Alignment Index (SALI)

The Smaller Alignment Index (SALI) is an efficient chaotic indicator based on the evolution of two initially distinct unit deviation vectors of an orbit [6, 9, 33–35]. The

Algorithm 2 Numerical computation of the maximum Lyapunov exponent.

```
Input: Hamiltonian function $H = T + V$, initial condition $\boldsymbol{x}_0 = (\boldsymbol{q}_0, \boldsymbol{p}_0)$, initial deviation vector $\boldsymbol{w}_0 = (\delta\boldsymbol{q}_0, \delta\boldsymbol{p}_0)$, integration step size $\tau$, maximum integration time $T$, symplectic integrator coefficients $(a_i, b_i)$, $i = 1, 2, \dots, k$
Output: Time evolution of maximum Lyapunov exponent (mLE) value $X_k$
Set flag $\leftarrow 0$, $s \leftarrow 0$, and $k \leftarrow 1$
while flag = 0 do
    Evolve the orbit $\boldsymbol{x}_{k-1}$ to $\boldsymbol{x}_k$ and the deviation vector $\boldsymbol{w}_{k-1}$ to $\boldsymbol{w}_k$
    Set $\alpha_k \leftarrow \|\boldsymbol{w}_k\|$
    Compute the mLE $X = \frac{1}{k\tau} \sum_{i=1}^{k} \ln \alpha_i$
    Normalise deviation vector $\boldsymbol{w}_k \leftarrow \boldsymbol{w}_k / \alpha_k$
    Set $k \leftarrow k + 1$
    if k$\tau > T$ or $X_{k-1} < 10^{-16}$ then
        Set flag $\leftarrow 1$
    end if
end while
```

variational equations govern the time evolution of these two deviation vectors as in the LCEs computations. SALI checks the possible coincidence of two normalised deviation vectors $\boldsymbol{w}_1(t)$ and $\boldsymbol{w}_2(t)$ without the orthogonalisation process as in the LCEs computations and is numerically computed at every time step by [33, 34]

$$\mathrm{SALI}(t) = \min\{\|\hat{\boldsymbol{w}}_1(t) + \hat{\boldsymbol{w}}_2(t)\|, \|\hat{\boldsymbol{w}}_1(t) - \hat{\boldsymbol{w}}_2(t)\|\},$$

where $\hat{\boldsymbol{w}}_i(t) = \frac{\boldsymbol{w}_i(t)}{\|\boldsymbol{w}_i(t)\|}$, $i = 1, 2$. If the two initial unit deviation vectors are orthogonal, then $\mathrm{SALI}(0) = \sqrt{2}$. Therefore, $0 \leq \mathrm{SALI}(t) \leq \sqrt{2}$ for all t.

In the case of regular orbits, SALI fluctuates around some non-zero value because the two deviation vectors tend to the tangent space of the torus, following a t^{-1} time evolution in log-log scale and having in general 2 different directions [34]. In contrast, the SALI for chaotic orbits tends to zero exponentially fast and the rate of this decrease is related to the two largest LCEs of the system [35], i.e.

$$\mathrm{SALI} \approx c e^{-(\lambda_1 - \lambda_2)}, \tag{2.26}$$

where c is a positive constant.

To compute SALI, we follow the time evolution of an initial condition and two unit deviation vectors $\mathbf{w}_1(0)$, $\mathbf{w}_2(0)$ which are initially orthogonal to each other. Then, SALI is defined by

$$\mathrm{SALI}(t) = \min\{\|\hat{\mathbf{w}}_1(t) - \hat{\mathbf{w}}_2(t)\|, \|\hat{\mathbf{w}}_1(t) + \hat{\mathbf{w}}_2(t)\|\},$$

where $\hat{\mathbf{w}}_i(t) = \frac{\mathbf{w}_i(t)}{\|\mathbf{w}_i(t)\|}$, $i = 1,2$, are the two normalized deviation vectors at time t. SALI approaches zero exponentially fast in time (as a function of the largest or 2 largest Lyapunov exponents) as in Eq. (2.26) for chaotic trajectories and non-zero, positive, values for regular trajectories [6, 9, 35]. We employ Algorithm 3 to compute numerically the SALI for a trajectory of a dynamical system, as demonstrated in [6, 9, 29].

Algorithm 3 Numerical computation of Smaller Alignment Index (SALI).

```
Input: Hamiltonian function $H = T + V$, initial condition $\boldsymbol{x}_0 = (\boldsymbol{q}_0, \boldsymbol{p}_0)$, two initial
    deviation vectors $\boldsymbol{w}_0^{(1)} = (\delta\boldsymbol{q}_0^{(1)}, \delta\boldsymbol{p}_0^{(1)})$ and $\boldsymbol{w}_0^{(2)} = (\delta\boldsymbol{q}_0^{(2)}, \delta\boldsymbol{p}_0^{(2)})$, integration step
    size $\tau$, maximum integration time $T$, symplectic integrator coefficients $(a_i, b_i)$,
    $i = 1, 2, \cdots, k$
Output: Time evolution of SALI value $S_k$
Set flag $\leftarrow 0$, $s \leftarrow 0$, and $k \leftarrow 1$
while flag = 0 do
    Evolve the orbit $\boldsymbol{x}_{k-1}$ to $\boldsymbol{x}_k$, the deviation vectors $\boldsymbol{w}_{k-1}^{(1)}$ to $\boldsymbol{w}_k^{(1)}$ and $\boldsymbol{w}_{k-1}^{(2)}$ to $\boldsymbol{w}_k^{(2)}$
    Normalize deviation vectors $\boldsymbol{w}_k^{(1)} \leftarrow \boldsymbol{w}_k^{(1)}/\|\boldsymbol{w}_k^{(1)}\|$ and $\boldsymbol{w}_k^{(2)} \leftarrow \boldsymbol{w}_k^{(2)}/\|\boldsymbol{w}_k^{(2)}\|$
    Compute the SALI $S_k = \min\{\|\boldsymbol{w}_k^{(1)} + \boldsymbol{w}_k^{(2)}\|, \|\boldsymbol{w}_k^{(1)} - \boldsymbol{w}_k^{(2)}\|\}$
    Set $k \leftarrow k + 1$
    if $k\tau > T$ or $S_{k-1} < 10^{-16}$ then
        Set flag $\leftarrow 1$
    end if
end while
```

2.4.4 Numerical integration of variational equations

The evolution of a deviation vector which is governed by the variational equations depends on a particular orbit. Therefore, the variational equations should be integrated simultaneously with the equations of motion. Indeed, any non-symplectic numerical integration algorithm can be used for the integration of Eqs. (2.22) and (2.23) as one system. One can use the general purpose Runge-Kutta 4th order and DOP853 integrators [36], which is an explicit non-symplectic Runge-Kutta 8th order, to integrate the equations of motion and the variational equations. One main issue with these non-symplectic integrators is that they produce relative energy errors that grow in time. This will affect the quality of the solution to the equations of motion and variational equations. In some cases, it will lead to the wrong classification of the chaotic behaviour of an orbit. To overcome this drawback, we opted in this PhD thesis to use the symplectic integrator method, provided by Yoshida's symplectic integrator scheme, to achieve the desired relative energy error bounded by choosing a suitable integrator order.

Consider the set of Eqs. (2.22) and (2.23) as one system of differential equations

$$\dot{\boldsymbol{q}} = \boldsymbol{p}, \tag{2.27}$$

$$\dot{\boldsymbol{p}} = -\frac{\partial V(\boldsymbol{q})}{\partial \boldsymbol{q}}, \tag{2.28}$$

$$\dot{\boldsymbol{\delta q}} = \boldsymbol{\delta p}, \tag{2.29}$$

$$\dot{\boldsymbol{\delta p}} = -\boldsymbol{D}^2 V(\boldsymbol{q})\boldsymbol{\delta q}. \tag{2.30}$$

Two approaches for solving Eqs. (2.27)-(2.30), i.e. the tangent dynamics Hamiltonian constant coefficient (TDHcc) method and the tangent map (TM) method, are explained in [37].

In the TDHcc method we initially integrate Eqs. (2.27)-(2.28) in the interval $[t_i, t_{i+1}]$, where $t_{i+1} = t_i + \Delta t, i = 0, 1, \ldots$, and Δt is the integration step size, to obtain the time evolution of the orbit $\boldsymbol{x}(t_i) = (\boldsymbol{q}(t_i), \boldsymbol{p}(t_i))$. At the same interval, the Hessian $\boldsymbol{D}^2 V(\boldsymbol{q}(t))$ is approximated by $\boldsymbol{D}^2 V(\boldsymbol{q}(t_i))$. Therefore, Eqs. (2.29)-(2.30) which are actually the equations of motion of the TDH (2.24), can be integrated by any symplectic integration scheme.

System (2.27)-(2.30) can be written as

$$\dot{\boldsymbol{Q}} = \boldsymbol{P},$$

$$\dot{\boldsymbol{P}} = \boldsymbol{F}(\boldsymbol{Q}),$$

with $\boldsymbol{Q} = (\boldsymbol{q}, \boldsymbol{\delta q})$, $\boldsymbol{P} = (\boldsymbol{p}, \boldsymbol{\delta p})$, and $\boldsymbol{F}(\boldsymbol{Q})$ is a vector with coordinates

$$F_i = \begin{cases} -\frac{\partial V(\boldsymbol{q})}{\partial q_i} & \text{for} \quad 1 \leq i \leq N, \\ -\sum\limits_{k=1}^{N} \frac{\partial^2 V(\boldsymbol{q})}{\partial q_i \partial q_k} \delta q_k & \text{for} \quad N < i \leq 2N. \end{cases}$$

The dynamics of any general variable $U(\boldsymbol{Q}, \boldsymbol{P})$ is given by

$$\begin{aligned} \dot{U}(\boldsymbol{Q}, \boldsymbol{P}) &= \sum_{i=1}^{2N} \left[\frac{\partial U(\boldsymbol{Q}, \boldsymbol{P})}{\partial Q_i} \dot{Q}_i + \frac{\partial U(\boldsymbol{Q}, \boldsymbol{P})}{\partial P_i} \dot{P}_i \right] \\ &= \left(\sum_{i=1}^{2N} \left[P_i \frac{\partial}{\partial Q_i} \dot{Q}_i + F_i \frac{\partial}{\partial P_i} \dot{P}_i \right] \right) U(\boldsymbol{Q}, \boldsymbol{P}) \\ &= (L_A + L_B)\, U(\boldsymbol{Q}, \boldsymbol{P}). \end{aligned} \tag{2.31}$$

According to [38], if a first order system of differential equations has the form

$$\dot{X} = (L_A + L_B)X, \tag{2.32}$$

where L_A and L_B are differential operators for which the two systems $\dot{X} = L_A X$ and $\dot{X} = L_B X$ are integrable, then the symplectic integration schemes can be applied to Eq. (2.32). Therefore, the system (2.27)-(2.30) can be integrated by the symplectic integrator since Eq. (2.31) satisfies Eq. (2.32). In analogy to Eqs. (2.18)-(2.19), the solution to Eqs. (2.27)-(2.30) for the initial vector $\boldsymbol{x}_j = (\boldsymbol{q}_j, \boldsymbol{p}_j)$ and initial deviation vector $\boldsymbol{w}_j = (\delta \boldsymbol{q}_j, \delta \boldsymbol{p}_j)$ at time t_j to its final state $\boldsymbol{x}_{j+1} = (\boldsymbol{q}_{j+1}, \boldsymbol{p}_{j+1})$ and deviation vector $\boldsymbol{w}_{j+1} = (\delta \boldsymbol{q}_{j+1}, \delta \boldsymbol{p}_{j+1})$ at time t_{j+1} is obtained by the following transformations

$$\boldsymbol{q}_{j+1}^{new} = \boldsymbol{q}_j^{old} + a_i \tau \left(\frac{dT}{d\boldsymbol{p}} \right)_{\boldsymbol{p} = \boldsymbol{p}_j^{old}}, \tag{2.33}$$

$$\boldsymbol{\delta q}_{j+1}^{new} = \boldsymbol{\delta q}_j^{old} + a_i \tau \left(\frac{\partial H_V}{\partial \boldsymbol{\delta p}} \right)_{\boldsymbol{\delta p} = \boldsymbol{\delta p}_j^{old}}, \tag{2.34}$$

$$\boldsymbol{p}_{j+1}^{new} = \boldsymbol{p}_j^{old} - b_i \tau \left(\frac{dV}{d\boldsymbol{q}} \right)_{\boldsymbol{q} = \boldsymbol{q}_{j+1}^{new}}, \tag{2.35}$$

$$\boldsymbol{\delta p}_{j+1}^{new} = \boldsymbol{\delta p}_j^{old} - b_i \tau \left(\frac{\partial H_V}{\partial \boldsymbol{\delta q}} \right)_{\boldsymbol{\delta q} = \boldsymbol{\delta q}_{j+1}^{new}}. \tag{2.36}$$

Equations (2.33)-(2.36) which solve simultaneously Hamilton's equations of motion (2.27)-(2.28) and the variational equations (2.29)-(2.30) are called the tangent map (TM) method. We implement the numerical integration of the variational equation according to Algorithm 4.

Next we apply different integration schemes to integrate the equations of motion and the variational equations to study each method's efficiency. In particular, we use Yoshida's 4th order integrator in both TDHcc and TM methods to study the

Algorithm 4 Numerical integration of the variational equations.

```
Input: Hamiltonian function $H = T + V$, tangent dynamic Hamiltonian given by Eq. (2.24), initial orbit $\boldsymbol{x}_0 = (\boldsymbol{q}_0, \boldsymbol{p}_0)$, initial deviation vector $\boldsymbol{w}_0 = (\delta\boldsymbol{q}_0, \delta\boldsymbol{p}_0)$, integration step size $\tau$, maximum integration time $T$, symplectic integrator coefficients $(a_i, b_i)$, $i = 1, 2, \ldots, k$
Output: Time evolution of $(\boldsymbol{q}_j, \boldsymbol{p}_j, \delta\boldsymbol{q}_j, \delta\boldsymbol{p}_j)$
$\boldsymbol{q}_0^{old} \leftarrow \boldsymbol{q}_0$ and $\boldsymbol{p}_0^{old} \leftarrow \boldsymbol{p}_0$
$\delta\boldsymbol{q}_0^{old} \leftarrow \delta\boldsymbol{q}_0$ and $\delta\boldsymbol{p}_0^{old} \leftarrow \delta\boldsymbol{p}_0$
for $j = 0$ to $\frac{T}{\tau} - 1$ do
    for $i = 1$ to $k$ do
        compute
            $\boldsymbol{q}_{j+1}^{new} = \boldsymbol{q}_j^{old} + a_i \tau \left( \frac{dT}{d\boldsymbol{p}} \right)_{\boldsymbol{p} = \boldsymbol{p}_j^{old}}$
            $\boldsymbol{\delta q}_{j+1}^{new} = \boldsymbol{\delta q}_j^{old} + a_i \tau \left( \frac{\partial H_V}{\partial \boldsymbol{\delta p}} \right)_{\boldsymbol{\delta p} = \boldsymbol{\delta p}_j^{old}}$
        compute
            $\boldsymbol{p}_{j+1}^{new} = \boldsymbol{p}_j^{old} - b_i \tau \left( \frac{dV}{d\boldsymbol{q}} \right)_{\boldsymbol{q} = \boldsymbol{q}_{j+1}^{new}}$
            $\boldsymbol{\delta p}_{j+1}^{new} = \boldsymbol{\delta p}_j^{old} - b_i \tau \left( \frac{\partial H_V}{\partial \boldsymbol{\delta q}} \right)_{\boldsymbol{\delta q} = \boldsymbol{\delta q}_{j+1}^{new}}$
        $\boldsymbol{q}_j^{old} \leftarrow \boldsymbol{q}_{j+1}^{new}$ and $\boldsymbol{p}_j^{old} \leftarrow \boldsymbol{p}_{j+1}^{new}$
        $\delta\boldsymbol{q}_j^{old} \leftarrow \delta\boldsymbol{q}_{j+1}^{new}$ and $\delta\boldsymbol{p}_j^{old} \leftarrow \delta\boldsymbol{p}_{j+1}^{new}$
    end for
    $\boldsymbol{q}_{j+1} \leftarrow \boldsymbol{q}_{j+1}^{new}$ and $\boldsymbol{p}_{j+1} \leftarrow \boldsymbol{p}_{j+1}^{new}$
    $\boldsymbol{q}_{j+1}^{old} \leftarrow \boldsymbol{q}_{j+1}$ and $\boldsymbol{p}_{j+1}^{old} \leftarrow \boldsymbol{p}_{j+1}$
    $\delta\boldsymbol{q}_{j+1} \leftarrow \delta\boldsymbol{q}_{j+1}^{new}$ and $\delta\boldsymbol{p}_{j+1} \leftarrow \delta\boldsymbol{p}_{j+1}^{new}$
    $\delta\boldsymbol{q}_{j+1}^{old} \leftarrow \delta\boldsymbol{q}_{j+1}$ and $\delta\boldsymbol{p}_{j+1}^{old} \leftarrow \delta\boldsymbol{p}_{j+1}$
end for
```

well-known 2D Hénon-Heiles system [39] described by the Hamiltonian

$$H = \frac{1}{2}\left(p_x^2 + p_y^2\right) + \frac{1}{2}\left(x^2 + y^2\right) + x^2 y - \frac{1}{3}y^3, \tag{2.37}$$

where x, y are the coordinates and p_x, p_y the conjugate momenta. The system describes the motion of stars orbiting around a galactic center, with the assumption that this motion occurs in a two-dimensional plane. Moreover, we integrate the equations of motion and variational equations of this system by the classic 4th order Runge-Kutta method and the DOP853 integrator [36] for comparison. We consider some regular and chaotic orbits of the Hénon-Heiles system (2.37) in Table 2.1 and calculate their mLE and SALI to investigate the performance of various integration schemes. The results are verified by checking how well they approximate the following theoretically known properties:

- The mLE tends to zero following a power law for regular orbits while it converges to nonzero value in the case of chaotic orbits.
- SALI is constant for regular orbits and tends to zero following the law (2.26) for chaotic orbits.

In our computations, we set the constant Hamiltonian value at $H = 0.125$ (which is also the constant energy of the system) and consider several orbits where the initial conditions (x, y, p_x, p_y) are given in Table 2.1. We also take the integration step size $\tau = 0.01$ for all integrators and set the relative and absolute error $\delta = 10^{-5}$ for the DOP853 method. Yoshida's fourth order symplectic integrator is used to integrate the equations of motions and the variational equations using the TDHcc and the TM methods.

Orbit	Initial Condition	Characteristic
R1	$(0, 0.1, 0.267, 0)$	Regular
R2	$(0, 0.4, 0.3, 0)$	Regular
R3	$(0, 0.5, 0.144, -0.25)$	Regular
C1	$(0, 0.52, 0.232, 0.14)$	Chaotic
C2	$(0, -0.38, 0.17, -0.2)$	Chaotic
C3	$(0, -0.1, 0.488, -0.03)$	Chaotic

Table 2.1: Initial conditions for the Hénon-Heiles system (2.37).

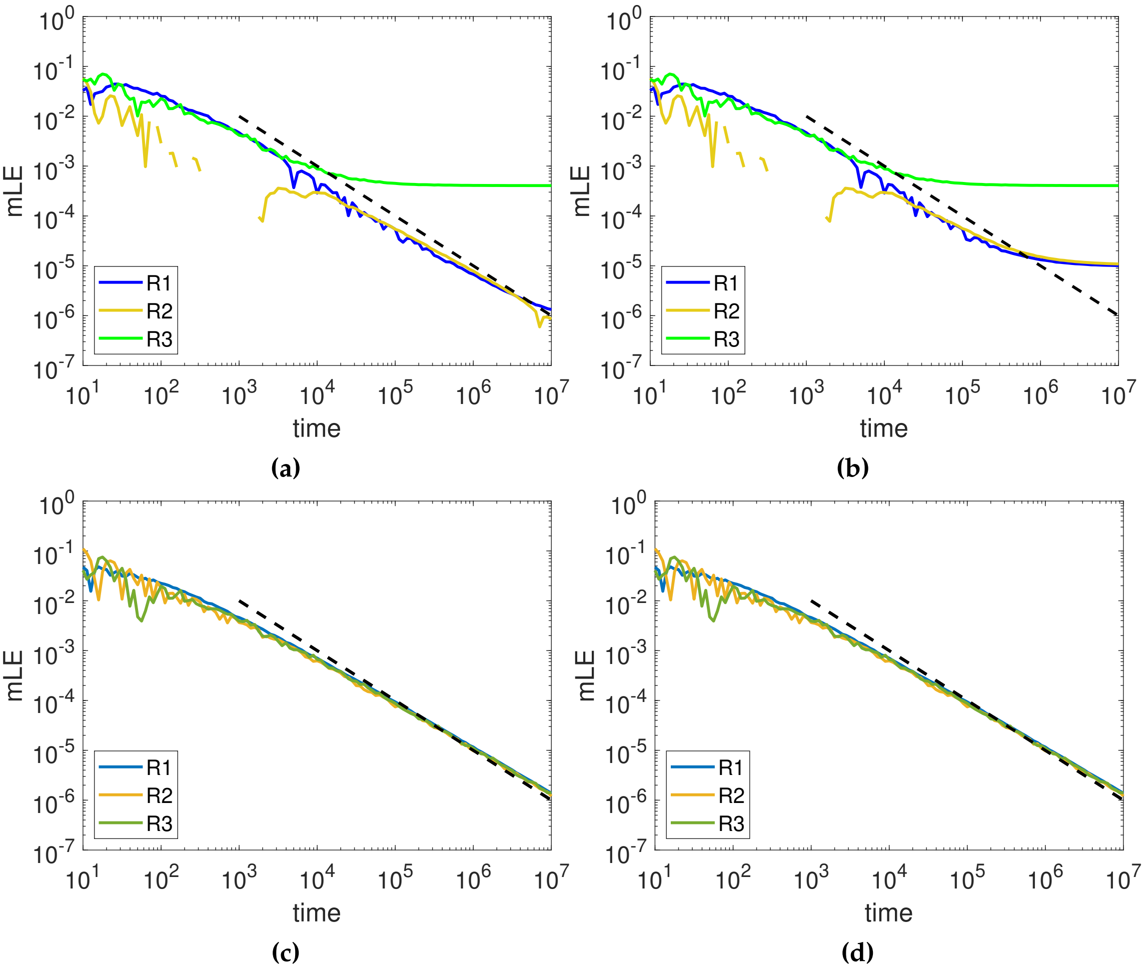

Figure 2.1. The time evolution of the mLCE for regular orbits of the Hénon-Heiles system. The equations of motion and the variational equations are solved by (a) the Runge-Kutta 4th order method, (b) the TDHcc method, (c) the TM method, (d) the DOP853 method. Note that the black-dashed line is the law $1/t$ and is a guide to the eye. Note also that all axes are in logarithmic scale.

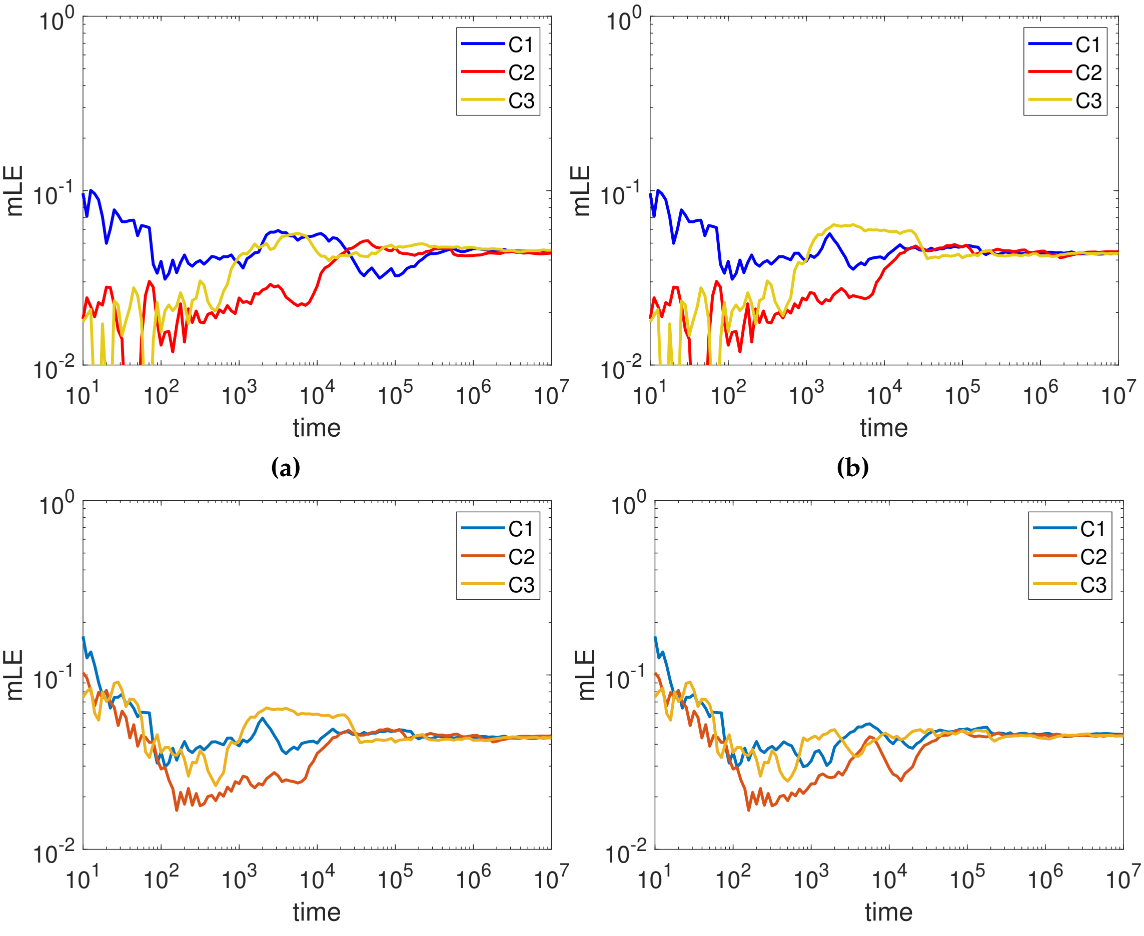

(a) (b)

(c) (d)

Figure 2.2. The time evolution of the mLE for chaotic orbits of the Hénon-Heiles system. The equations of motion and the variational equations are solved by (a) the Runge-Kutta 4th order method, (b) the TDHcc method, (c) the TM method, (d) the DOP853 method. Note that all axes are in logarithmic scale.

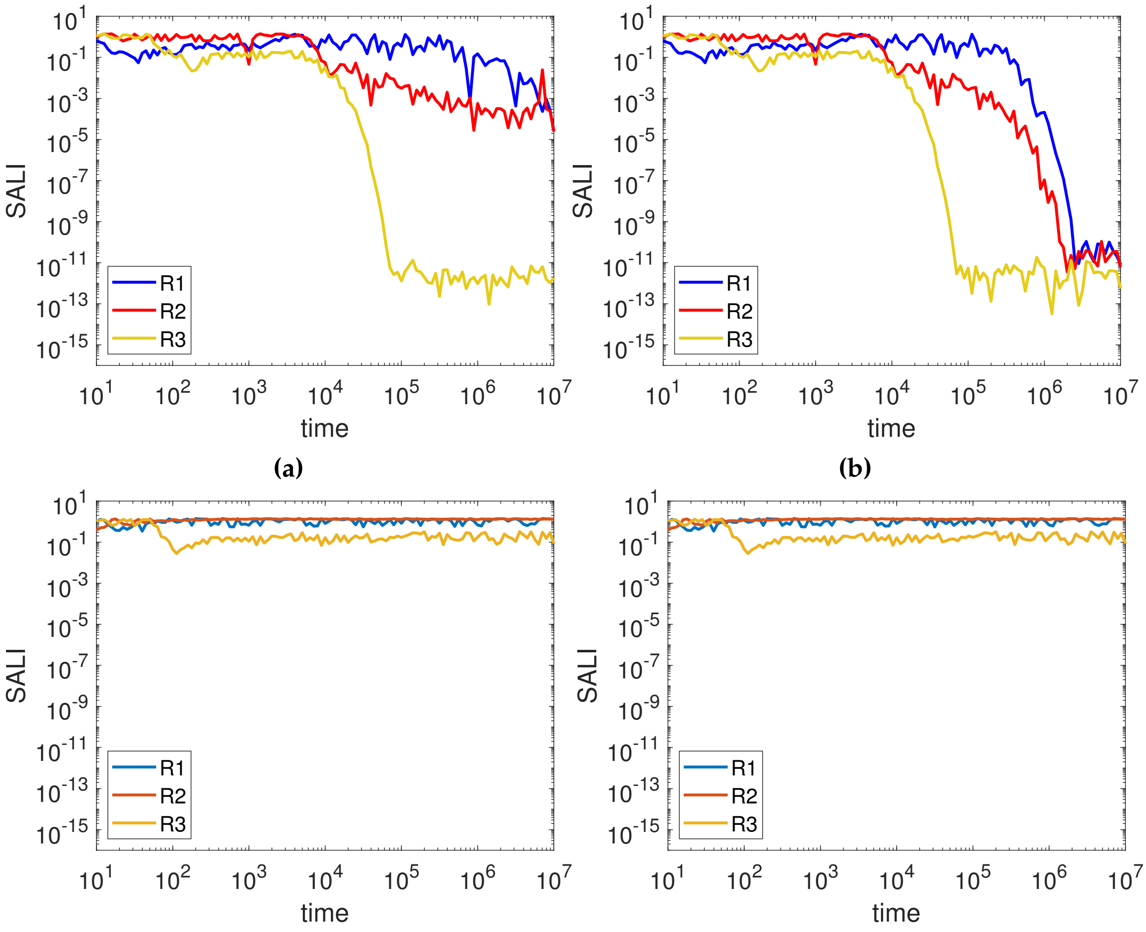

(a) **(b)**

(c) **(d)**

Figure 2.3. The time evolution of the SALI for regular orbits of the Hénon-Heiles system. The equations of motion and the variational equations are solved by (a) the Runge-Kutta 4th order method, (b) the TDHcc method, (c) the TM method, (d) the DOP853 method. Note that all axes are in logarithmic scale.

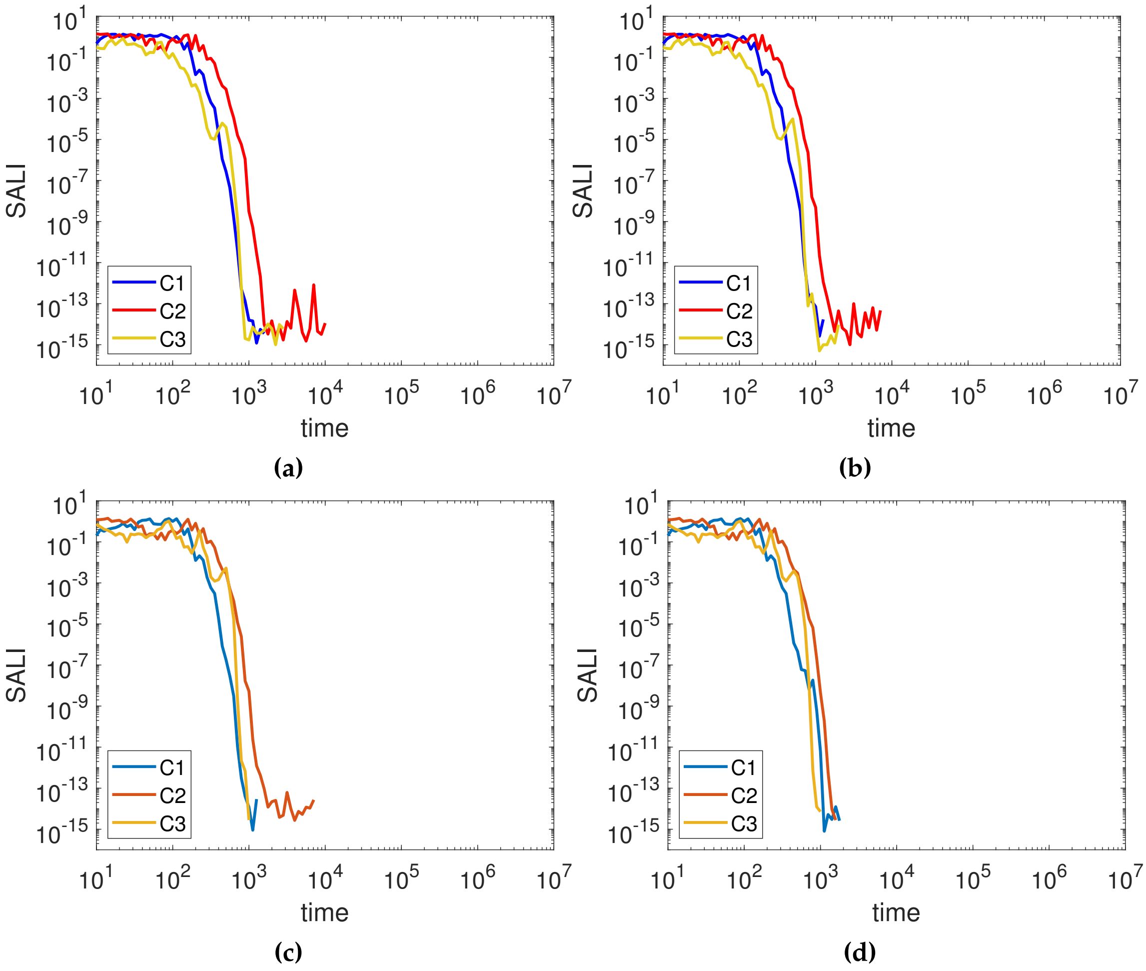

Figure 2.4. The time evolution of the SALI for chaotic orbits of the Hénon-Heiles system. The equations of motion and the variational equations are solved by (a) the Runge-Kutta 4th order method, (b) the TDHcc method, (c) the TM method, (d) the DOP853 method. Note that all axes are in logarithmic scale.

In Fig. 2.1 we see that the TM method and the DOP853 method successfully evaluate the mLE of all three different regular orbits. The computed mLE tends to zero following a t^{-1} law until the final integration time $t = 10^7$. However, the Runge-Kutta 4th order method and the TDHcc method failed to demonstrate this behaviour. The orbit R3 in Fig. 2.1(a) levels off after $t = 10^4$ which indicates the chaotic nature of this orbit. It means that the Runge-Kutta 4th order method leads to the wrong classification of a regular orbit as a chaotic. Furthermore, all regular orbits are classified as chaotic orbits by the TDHcc method as shown in Fig. 2.1(b). This problem where one wrongly classifies the regular orbits as chaotic orbits occur not only from the computation of mLE, but also from the computation of the SALI as we can see in Fig. 2.3. Therefore, the TM method and the DOP853 method are the best options to integrate the equations of motion and variational equations when studying Hamiltonian systems.

Although only the TM and the DOP853 methods produced correct results characterising regular orbits, it is worth noting that all methods gave practically similar results for chaotic orbits. Figure 2.2 shows the mLE converging to nonzero values for chaotic orbits for all methods. Moreover, SALI decreases exponentially to zero in Fig. 2.4 which indicates the orbits are chaotic.

In this PhD thesis, two methods are employed for evolving different types of systems. The Tangent Map method is used for Hamiltonian systems, and the DOP853 for non-Hamiltonian systems.

The Tangent Map method is a numerical integration technique specifically designed for Hamiltonian systems. As explained before, it is based on the idea of tracking the evolution of a point in the tangent space of the phase space of the system. By propagating the tangent vector along with the system trajectory, it provides an accurate and efficient way to simulate the Hamiltonian dynamics.

On the other hand, the DOP853 method is utilised when dealing with non-Hamiltonian systems. This method is a high-order adaptive integrator that can handle stiff and non-stiff differential equations. It offers excellent accuracy and stability, making it suitable for accurately evolving the orbit and variational equation of non-Hamiltonian systems.

2.5 The Fermi-Pasta-Ulam-Tsingou system

Fermi, Pasta and Ulam conducted a numerical simulation in 1953 with Tsingou's assistance to investigate the rate of approach to energy equipartition in a dynamical system that describes a one-dimensional particle chain with nonlinear forces between particles - known as an FPUT lattice with fixed ends [1]. Their expectation was that quadratic forces would allow the continuous energy transfer from the initially excited first normal mode to higher normal modes that would led to thermalisation or mixing. Instead, energy exchange only occurred among certain few modes before returning back down within one percent of its initial value so that the system appeared nearly periodic. This recurrence phenomena were confirmed over a longer period of time following the work in [10, 11]. They observed the appearence of super recurrence, in which more energy returned to the initially excited mode.

The Hamiltonian function of the FPUT-α system is given by

$$H(x,p) = \frac{1}{2}\sum_{j=0}^{N} p_j^2 + \sum_{j=0}^{N} \frac{1}{2}\left(x_{j+1} - x_j\right)^2 + \frac{\alpha}{3}\left(x_{j+1} - x_j\right)^3 = E, \tag{2.38}$$

with fixed boundary conditions $x_0 = x_{N+1} = 0$ and $p_0 = 0$. Here, E is the total energy of the system. By viewing the FPUT$-\alpha$ lattice as a model of particles coupled with springs, $x_j(t)$ represents the relative displacement of the jth-particle from its equilibrium position at any time t and $p_j(t)$ its corresponding conjugate momentum at any time t. The equations of motion of Hamiltonian (2.38) follow as

$$\ddot{x}_j = (x_{j+1} - x_j) + (x_{j-1} - x_j) + \alpha\left((x_{j+1} - x_j)^2 - (x_j - x_{j-1})^2\right). \tag{2.39}$$

Using the linear normal-mode transformations

$$\boldsymbol{x} = A\boldsymbol{Q}, \tag{2.40}$$

$$\boldsymbol{p} = A\boldsymbol{P}, \tag{2.41}$$

where $\boldsymbol{x} = [x_1\, x_2\, \dots\, x_N]^T$, $\boldsymbol{p} = [p_1\, p_2\, \dots\, p_N]^T$,$\boldsymbol{Q} = [Q_1\, Q_2\, \dots\, Q_N]^T$, $\boldsymbol{P} = [P_1\, P_2\, \cdots\, P_N]^T$, and

$$A = \sqrt{\frac{2}{N+1}} \begin{bmatrix} \sin\left(\frac{\pi}{N+1}\right) & \sin\left(\frac{2\pi}{N+1}\right) & \dots & \sin\left(\frac{N\pi}{N+1}\right) \\ \sin\left(\frac{2\pi}{N+1}\right) & \sin\left(\frac{4\pi}{N+1}\right) & \dots & \sin\left(\frac{2N\pi}{N+1}\right) \\ \vdots & \vdots & \ddots & \vdots \\ \sin\left(\frac{N\pi}{N+1}\right) & \sin\left(\frac{2N\pi}{N+1}\right) & \dots & \sin\left(\frac{N^2\pi}{N+1}\right) \end{bmatrix}. \tag{2.42}$$

we can rewrite the Hamiltonian function (2.38) as

$$H = \frac{1}{2}\sum_{k=1}^{N}\left(P_k^2 + \omega_k^2 Q_k^2\right) + \alpha H_3(Q_1, Q_2, \cdots, Q_N),$$

for some nonlinear function H_3, where

$$\omega_k = 2\sin\left(\frac{k\pi}{2(N+1)}\right). \tag{2.43}$$

Furthermore, the normal mode energy of mode k is defined as

$$E_k = \frac{1}{2}\left(P_k^2 + \omega_k^2 Q_k^2\right).$$

Note that according to this definition, the sum of normal-mode energies $\sum_{k=1}^{N} E_k$ is exactly the same as the Hamiltonian energy E only for linear lattices with $\alpha = 0$. Nonetheless, it serves as a good approximation for relatively small nonlinear strengths α where energy contributions from coupled modes are negligible. Using Eqs. (2.40)-(2.41) in (2.39), we obtain the equations of motion in normal-mode coordinates as

$$\ddot{\boldsymbol{Q}} = D\boldsymbol{Q} + A^{-1}\boldsymbol{F}(\boldsymbol{Q}), \tag{2.44}$$

where

$$D = \begin{bmatrix} -\omega_1^2 & 0 & \cdots & 0 \\ 0 & -\omega_2^2 & & 0 \\ \vdots & & \ddots & \vdots \\ 0 & 0 & \cdots & -\omega_N^2 \end{bmatrix}, \quad \boldsymbol{F}(\boldsymbol{Q}) = \begin{bmatrix} f_1(\boldsymbol{Q}) \\ f_2(\boldsymbol{Q}) \\ \vdots \\ f_N(\boldsymbol{Q}) \end{bmatrix}.$$

and A^{-1} denotes the inverse of matrix A given in Eq. (10).

Fermi, Pasta, Ulam and Tsingou [1] excited a single mode, i.e. the first normal mode with $k = 1$, and let the energy slowly drift to other modes. They opted for the initial condition

$$p_i = 0, \tag{2.45a}$$

$$x_i = \sin\left(\frac{\pi i}{N+1}\right),\ i = 1,\dots,N. \tag{2.45b}$$

They expected to observe the thermalisation of energy predicted by Boltzmann-Gibbs (BG) statistical mechanics and wanted to measure the thermalisation rate of this system. Surprisingly, their numerical experiment showed that after 157 periods of the mode $k = 1$ (first linear normal mode) almost all energy was back to the first mode. Figures (2.5)-(2.6) show respectively the normal-mode energy for the first four modes of the FPUT-α system (2.39) with $N = 32$ and $N = 64$.

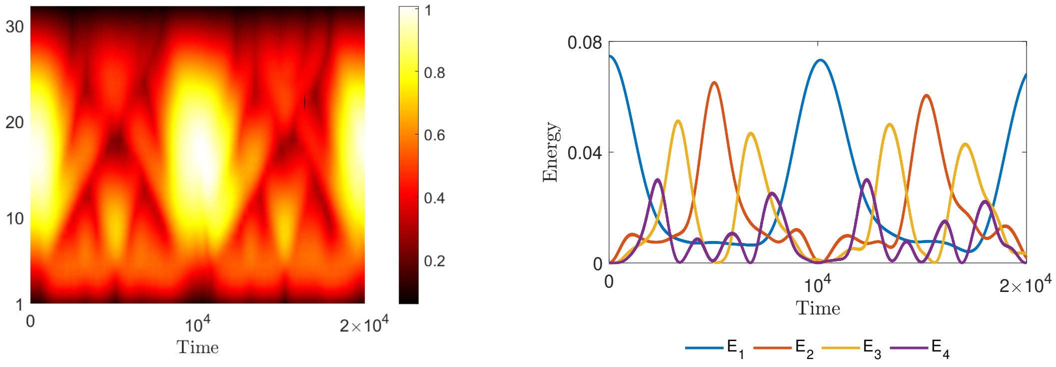

(a) **(b)**

Figure 2.5. FPUT recurrences of the Hamiltonian system (2.38). (a) Dynamics of $x_j(t)$ using the initial condition in (2.45), where $E = 0.07471$. Panel (a) shows the top view of the oscillation envelope of $x_j(t)$ in time. (b) Energy of the first four normal modes in the dynamics shown in panel (a). Note in panel (b) how almost all of the energy returns to the first normal mode at around $t = 10^4$, i.e., the appearance of an FPUT recurrence. Here we have used $N = 32$ in the computations in both panels. The range of values in the vertical axis in panel (a) is between 1 and $N = 32$.

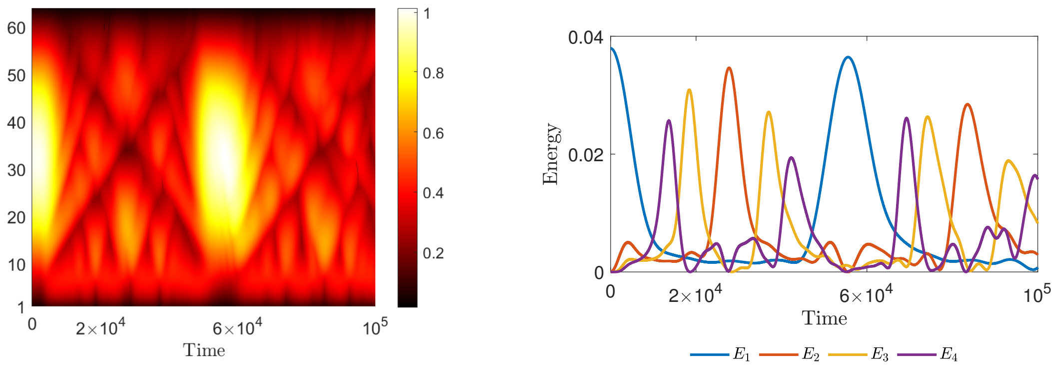

(a) (b)

Figure 2.6. FPUT recurrences of the Hamiltonian system (2.38). (a) Dynamics of $x_j(t)$ using the initial condition in (2.45), where $E = 0.03795$. Panel (a) shows the top view of the oscillation envelope of $x_j(t)$ in time. (b) Energy of the first four normal modes in the dynamics shown in panel (a). Note in panel (b) how almost all of the energy returns to the first normal mode at around $t = 6 \times 10^4$, i.e., the appearance of an FPUT recurrence. Here we have used $N = 64$ in the computations in both panels. The range of values in the vertical axis in panel (a) is between 1 and $N = 64$.

2.6 Statistical mechanics

2.6.1 Boltzmann-Gibbs statistics

Boltzmann-Gibbs statistics provides a framework that help us describe systems in an equilibrium state, where mixing and ergodic properties prevail. This equilibrium state is underpinned by the Central Limit Theorem, ensuring the convergence of statistical properties. A defining feature of Boltzmann-Gibbs statistics is the emergence of exponential and Gaussian distributions, which arise from maximising the Boltzmann-Gibbs entropy. These distributions encapsulate the probabilistic behaviour of equilibrium systems, reflecting the underlying principles of statistical mechanics.

The Boltzmann-Gibbs entropy for a set of W possible discrete states is given by [40]

$$S_{BG} = -k \sum_{i=1}^{W} p_i \ln p_i, \tag{2.46}$$

with

$$\sum_{i=1}^{W} p_i = 1.$$

and where k is a positive constant. Here, p_i is the probability of the system occupying the i-th microstate. Equation (2.46) can be written as

$$S_{BG} = -k\langle \ln p_i \rangle = k\langle \ln 1/p_i \rangle, \tag{2.47}$$

where $\langle x \rangle = \sum_{i=1}^{W} p_i(x)$ is the standard mean value. For a particular case of equal probabilities, where $p_i = 1/W$, $\forall i$ (since there are W possible microstates), Eq. (2.46) becomes

$$S_{BG} = k \ln W. \tag{2.48}$$

The formula in Eq. (2.48) is engraved on Boltzmann's tombstone in his honour.

The BG entropy for continuous-states system is given by

$$S_{BG} = -\int_{-\infty}^{\infty} p(x) \ln p(x) dx,$$

where

$$\int_{-\infty}^{\infty} p(x)dx = 1. \tag{2.49}$$

Consider the case where the mean value of the x variable is 0. In this case, we might know the mean value of the squared variable

$$\int_{-\infty}^{\infty} x^2 p(x)dx = X^{(2)}. \tag{2.50}$$

In order to use the Lagrange method to obtain the optimising distribution, we define

$$\Phi(p) = -\int_{-\infty}^{\infty} p(x)\ln p(x)dx - \alpha\int_{-\infty}^{\infty} p(x)dx - \beta\int_{-\infty}^{\infty} x^2 p(x)dx.$$

Imposing the condition $d\Phi(p)/dp = 0$, we obtain

$$1 + \ln p + \beta x^2 = 0,$$

where Eq. (2.49) is used to eliminate the Lagrange parameter α, hence

$$p = e^{-1-\beta x^2}. \tag{2.51}$$

By using Eq. (2.51) in Eq. (2.49), we have

$$\int_{-\infty}^{\infty} e^{-\beta x^2}\, dx = e,$$

therefore

$$p = \frac{e^{-\beta x^2}}{\int_{-\infty}^{\infty} e^{-\beta x^2} dx} = \sqrt{\frac{\beta}{\pi}} e^{-\beta x^2}. \tag{2.52}$$

Furthermore, by using (2.52) in (2.50) we have

$$X^{(2)} = \frac{1}{2\beta},$$

hence

$$p = \frac{e^{-x^2/(2X^{(2)})}}{\sqrt{2\pi X^{(2)}}}. \tag{2.53}$$

Equation (2.53) gives the connection between Gaussian distributions and BG entropy.

2.6.2 Tsallis entropy

One way to explain the idea behind Tsallis entropy, which is a generalisation of BG entropy, is by considering the differential equation

$$\frac{dy}{dx} = y^q, \tag{2.54}$$

with $y(0) = 1$ and $q \in \mathbb{R}$ [40]. The solution to Eq. (2.54) is given by

$$y = (1 + (1-q)x)^{1/(1-q)}, \tag{2.55}$$

where its inverse function is given by

$$y = \frac{x^{1-q}-1}{1-q}, \; x > 0. \tag{2.56}$$

From Eqs. (2.55) and (2.56), we define the q-exponential and the q-logarithm as

$$e_q^x = (1+(1-q)x)^{1/(1-q)},$$

and

$$\ln_q x = \frac{x^{1-q}-1}{1-q}, \; x > 0. \tag{2.57}$$

Note that for $q = 1$, we have $e_q^x = e^x$ and $\ln_q x = \ln x$.

The BG entropy can be generalised by the following formula [41]

$$S_q = k \ln_q W$$

where $S_1 = S_{BG}$. Moreover, Eq. (2.47) can also be generalised by

$$S_q = k\langle \ln_q(1/p_i)\rangle. \tag{2.58}$$

Using Eq. (2.57) in Eq. (2.58), we obtain

$$S_q = k\frac{1-\sum_{i=1}^{W} p_i^q}{q-1}. \tag{2.59}$$

The formula in Eq. (2.59) is known as Tsallis entropy [40, 41].

Now consider the entropic optimisation case similar to what we did previously for the BG entropy. For continuous systems, Eq. (2.59) takes the form

$$S_q = k\frac{1-\int_{-\infty}^{\infty}(p(x))^q dx}{q-1},$$

with

$$\int_{-\infty}^{\infty} p(x)dx = 1.$$

Consider the case where the q-mean value of the x variable is 0. Then, we might know the q-mean value of the squared variable

$$\int_{-\infty}^{\infty} x^2 P(x)dx = X_q^{(2)},$$

where

$$P(x) = \frac{(p(x))^q}{\int_{-\infty}^{\infty} p(s)ds}.$$

In order to use the Lagrange method to obtain the optimising distribution, we define

$$\Phi(p) = \frac{1-\int_{-\infty}^{\infty}(p(x))^q\, dx}{q-1} - \alpha\int_{-\infty}^{\infty} p(x)dx - \beta_q\frac{\int_{-\infty}^{\infty} x^2(p(x))^q dx}{\int_{-\infty}^{\infty}(p(x))^q dx}.$$

Imposing the condition $d\Phi(p)/dp = 0$, we obtain

$$p_{\mathrm{opt}}(x) = \frac{e_q^{-\beta'_q x^2}}{\int_{-\infty}^{\infty} e_q^{-\beta' s^2} ds}, \tag{2.60}$$

with

$$\beta'_q = \frac{\beta_q}{1 + (1-q)\beta_q X_q^{(2)}}.$$

The probability distribution function (2.60) is known as a q-Gaussian. It is connected to S_q entropy in the same way Gaussians are connected to S_{BG}.

In general, the q-Gaussian function can be written as [42]

$$G_q(\beta, x) = \frac{\sqrt{\beta}}{C_q} e_q^{-\beta x^2},$$

where

$$C_q = \begin{cases} \dfrac{2\sqrt{\pi}\,\Gamma\left(\frac{1}{1-q}\right)}{(3-q)\sqrt{1-q}\,\Gamma\left(\frac{3-q}{2(1-q)}\right)}, & -\infty < q < 1, \\ \sqrt{\pi}, & q = 1, \\ \dfrac{\sqrt{\pi}\,\Gamma\left(\frac{3-q}{2(q-1)}\right)}{\sqrt{q-1}\,\Gamma\left(\frac{1}{q-1}\right)}, & 1 < q < 3. \end{cases}$$

Here, C_q is the normalisation factor and β is a parameter which charaterises the width of the q-Gaussian distribution function [42, 43].

The q-Gaussian distribution is a prominent probability distribution that arises in various systems, as demonstrated in [14, 16, 42]. This distribution proves especially useful when addressing systems characterised by significant correlations among the random variables, where the limiting distribution deviates from the standard Gaussian distribution. In Chapter 5 we will study the standard map with different parameter values which exhibit chaotic and regular behaviour.

Chapter 3

Variability in the nonlinear coupling terms of the FPUT-α lattices

A one-dimensional lattice system with variability refers to a mathematical or physical model consisting of a linear arrangement of nodes or sites, where each node exhibits some form of uncertainty or diversity in its properties or characteristics. This system is often studied in the context of statistical physics [44], condensed matter physics [45], or mathematical modeling [46].

In a one-dimensional lattice, the nodes are arranged sequentially along a line, forming a chain-like structure. The variability in this system typically arises from differences in the properties or states of the individual nodes. These properties can include energy levels, spin orientations, particle densities, or other relevant parameters depending on the specific context of the study [47].

The variability in a one-dimensional lattice can have a significant impact on the overall behaviour and properties of the system. It introduces disorder or inhomogeneity into an otherwise ordered structure, leading to interesting and often complex phenomena. The presence of variability can affect the system's thermodynamic properties [48], phase transitions [49], and transport phenomena [50].

Various mathematical and computational techniques can be employed to investigate one-dimensional lattice systems with variability. These techniques may include statistical mechanics [44], Monte Carlo simulations [51, 52], exact diagonalisation methods [53], or other approaches suitable for capturing the system's behaviour and analysing its properties.

In a one-dimensional lattice system, disorder can manifest in various forms. It can arise from disordered potentials, as seen in the Anderson model [54]. Random interactions between neighboring particles [55], imperfections in crystal structures [56], or the presence of heterogeneous particle chains with different masses, sizes, or interaction potentials [57] are additional sources of disorder within the system.

This chapter focuses on the investigation of one-dimensional lattice systems with heterogeneity, specifically the FPUT-α system featuring variability in the nonlinear coupling terms. Observing the FPUT-α system at low energy reveals that it closely resembles the Toda model [13]. However, when we depart from the Toda model (increasing variability), the system's behaviour is expected to diverge from the integrable and recurrent characteristics of the Toda model. This chapter provides an analytical and numerical investigation to validate this expectation. Additionally, we explore the system's chaotic behaviour by examining the effect of varying the strength of variability.

3.1 Variability in the FPUT-α lattices

Nelson et al. [57] numerically showed that the recurrences in the FPUT system could be weakened if one introduced tolerances into each particle. Moreover, the recurrences will disappear for large enough tolerance and the energy will be localised. In their study, the tolerances are incorporated into the system in several scenarios based on manufacturing constraints. Here, we study the case where the variability is incorporated in the nonlinear terms only, therefore the equations of motion become

$$\begin{aligned} \ddot{x}_j =& (x_{j+1} - x_j) + (x_{j-1} - x_j) \\ &+ \alpha\Big((v_{j+1}x_{j+1} - v_j x_j)^2 - (v_j x_j - v_{j-1}x_{j-1})^2\Big), \end{aligned} \tag{3.1}$$

for some random number v_j. The variabilities or the tolerance values v_i's are generated randomly from a Gaussian distribution. For τ% tolerance, the values of v_i are drawn from a Gaussian distribution with a mean of 1 and a standard deviation of $\sigma = 1/3 \times 0.01\tau$. Therefore, the values of v_i lie within the interval $[1 - 0.01\tau, 1 + 0.01\tau]$.

In Fig. 3.1 we show the first four modes of normal mode energy of $N = 64$ particles for four different tolerance, i.e. 0%, 1%, 5%, and 10%. We can observe that tolerance has the effect of destroying the recurrence. We can notice a minor drop in the second peak of E_1 with a rather modest tolerance, namely 1%. As tolerance increases, less energy returns to the first normal-mode and the system distributes energy with more additional normal-modes. When we increase the tolerance, energy localisation occurs, and the energy is concentrated only on the originally excited mode, i.e. the first normal-mode.

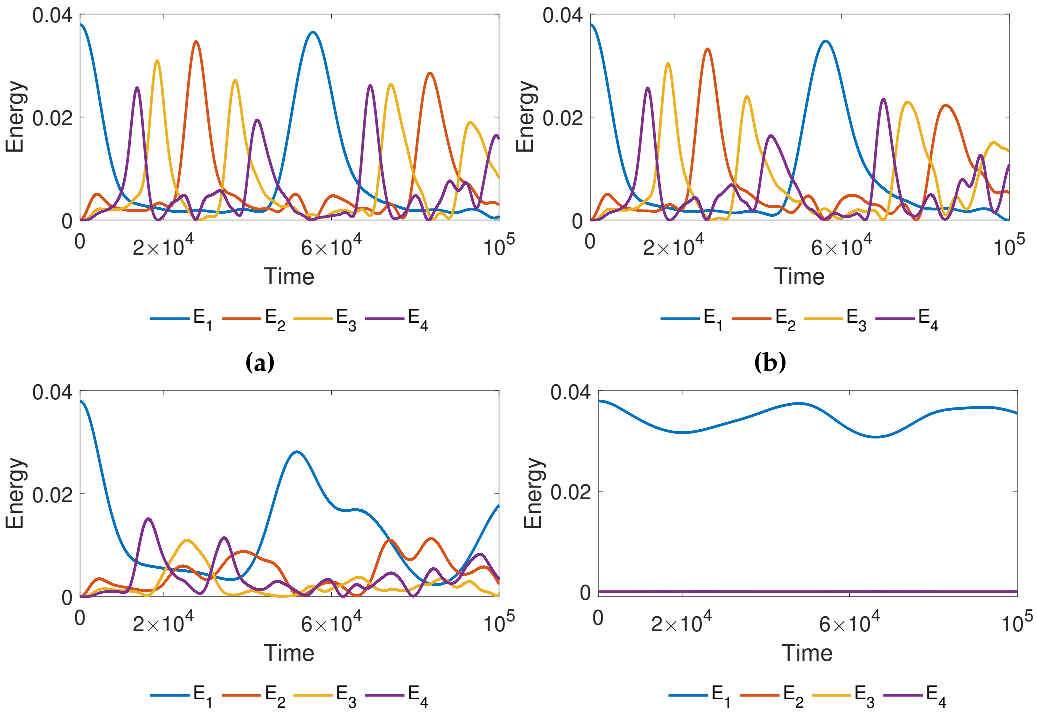

(a) (b)

(c) (d)

Figure 3.1. The normal mode energy with (a) 0% tolerance, (b) 1% tolerance, (c) 5% tolerance, and (d) 10% tolerance for $N = 64$ particles.

The equations of motion (3.1) in the normal mode coordinates follow as

$$\ddot{\mathbf{Q}} = D\mathbf{Q} + A^{-1}\widehat{\mathbf{F}}(\mathbf{Q}), \tag{3.2}$$

for some nonlinear, vector-function $\widehat{\mathbf{F}}(\mathbf{Q})$ that depends on τ, which is different to $\mathbf{F}(\mathbf{Q})$ in Eq. (2.44) in the absence of variability. The initial conditions then become $Q_1(0) = \sqrt{(N+1)/2}$, $Q_k(0) = 0$, $k = 2,3,\ldots,N$, and $\dot{Q}_k = 0$, $k = 1,2,\ldots,N$.

3.2 A two normal-mode system and bifurcation analysis

The recurrences suggest that most of the normal mode coordinates are zero. Therefore, we can approximate system (3.2) by considering only the first few modes while taking all other modes equal to zero. Figure 3.2 shows the normal mode energy obtained from the solutions of the equation of motion (3.2) using different number of modes without variability (i.e. 0% tolerance) for $N = 64$ particles. Moreover, Figs. 3.3-3.4 show the normal mode energy of different number of modes where the variability is incorporated in the equation of motion (3.2). From Figs. 3.2-3.4, we can see that we can still observe the recurrences and the breakdown when we increase the tolerance for the FPUT-α system even if we only use a few modes. Therefore, we approximate Eq. (3.2) by taking $Q_k(0) = 0$, $k = 3, 4, \ldots, N$ and obtain the following system

$$\ddot{Q}_1 = -\omega_1^2 Q_1 + \epsilon\Big(A_1 Q_1^2 + A_2 Q_2^2 + A_3 Q_1 Q_2\Big), \tag{3.3}$$

$$\ddot{Q}_2 = -\omega_2^2 Q_2 + \epsilon\Big(B_1 Q_1^2 + B_2 Q_2^2 + B_3 Q_1 Q_2\Big), \tag{3.4}$$

where $\omega_2 = 2\omega_1 + \epsilon$, $\epsilon \ll 1$, A_i, $B_i \in \mathbb{R}$, $i = 1, 2, 3$. In the next section, we solve Eqs. (3.3)-(3.4) using multiple-time scale approximation [58]. It is worth noting that the Poincaré-Lindstedt series has been employed to study the FPUT system without disorder in [59]. We compare the multiple-time scale approximation and the Poincaré-Lindstedt series method by solving the Duffing equation using both methods in the Appendix. Our calculation indicates that both methods are

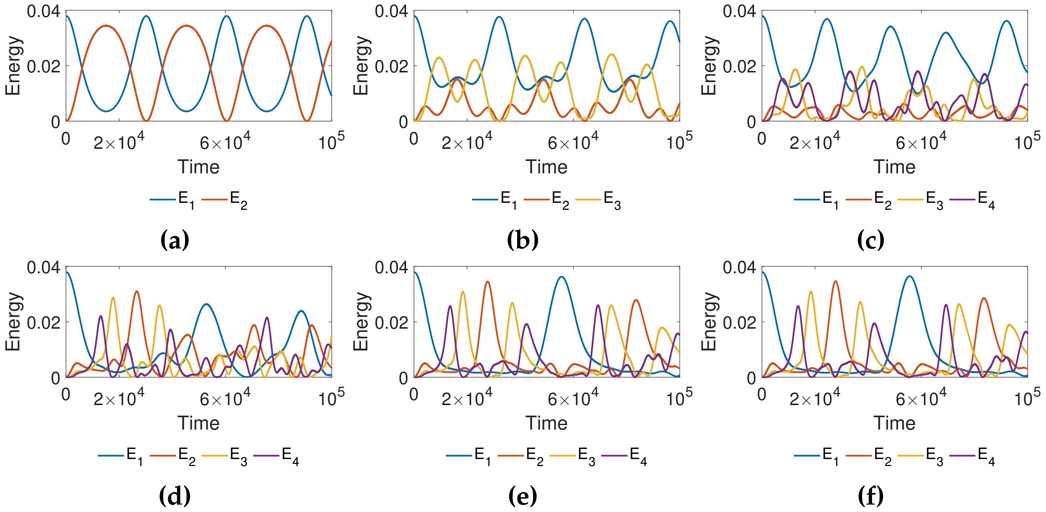

(a) (b) (c)

(d) (e) (f)

Figure 3.2. The normal mode energy of system (3.2) for $N = 64$ particles with 0% tolerance for (a) 2 modes, (b) 3 modes, (c) 4 modes, (d) 8 modes, (e) 16 modes, and (f) 32 modes.

equivalent. Therefore, we expect that both methods will give us the same result when we apply to the disordered FPUT system.

3.2.1 Multiple-time scale approximation

Assume the approximate solutions to Eqs. (3.3)-(3.4) are given by the following asymptotic series

$$Q_1 = X_0(t,T) + \epsilon X_1(t,T) + \cdots,$$

$$Q_2 = Y_0(t,T) + \epsilon Y_1(t,T) + \cdots,$$

where $T = \epsilon t$ is the slow time variable in multiple-time scale expansions [58]. Using the chain rule, we have

$$\begin{aligned}\frac{dQ_1}{dt} &= \left(\frac{\partial X_0}{\partial t} + \frac{\partial X_0}{\partial T}\frac{dT}{dt}\right) + \epsilon\left(\frac{\partial X_1}{\partial t} + \frac{\partial X_1}{\partial T}\frac{dT}{dt}\right),\\ &= \frac{\partial X_0}{\partial t} + \epsilon\left(\frac{\partial X_0}{\partial T} + \frac{\partial X_1}{\partial t}\right) + \mathcal{O}(\epsilon^2),\end{aligned}$$

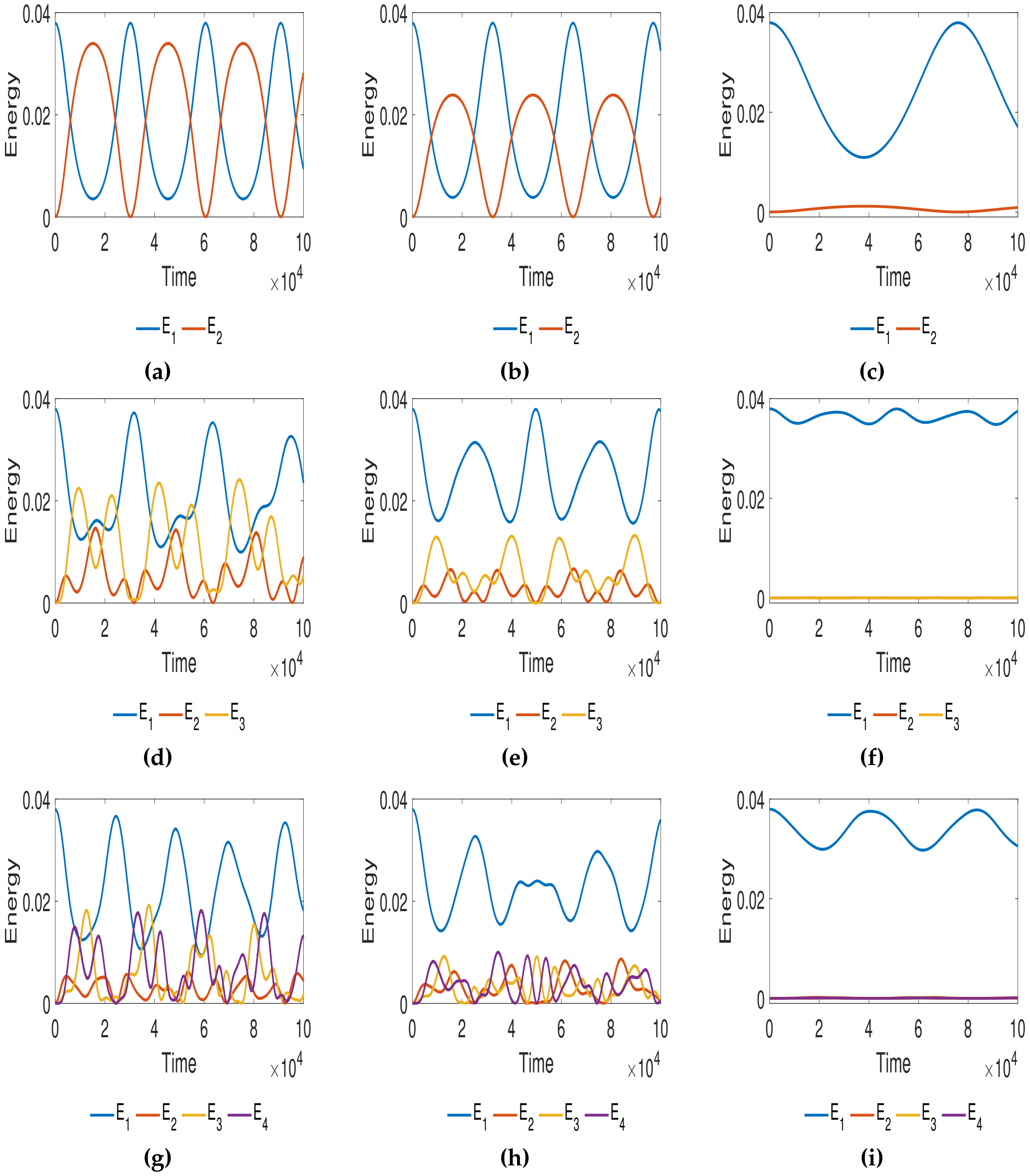

(a) **(b)** **(c)**

(d) **(e)** **(f)**

(g) **(h)** **(i)**

Figure 3.3. The normal mode energy with 1% tolerance, 5% tolerance, and 10% tolerance for (a)-(c) 2 modes, (d)-(f) 3 modes, and (g)-(i) 4 modes.

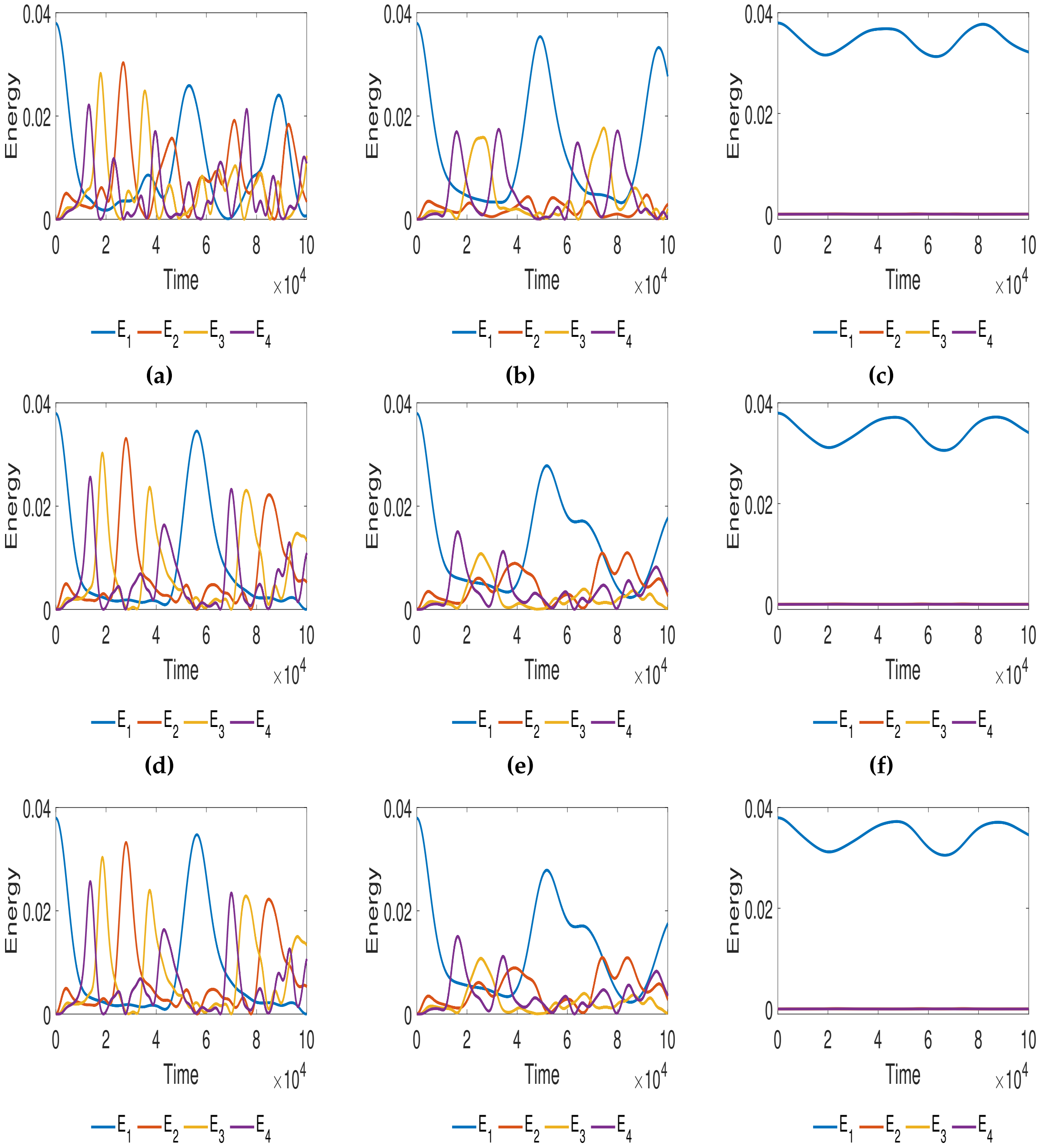

(a) (b) (c)

(d) (e) (f)

(g) (h) (i)

Figure 3.4. The normal mode energy with 1% tolerance, 5% tolerance, and 10% tolerance for (a)-(c) 8 modes, (d)-(f) 16 modes, and (g)-(i) 32 modes.

Furthermore, differentiating with respect to t again gives

$$\frac{d^2Q_1}{dt^2}=\frac{\partial^2 X_0}{\partial t^2}+\epsilon\left(2\frac{\partial^2 X_0}{\partial T\partial t}+\frac{\partial^2 X_1}{\partial t^2}\right)+O(\epsilon^2). \tag{3.5}$$

Following similar procedures, we also have

$$\frac{d^2Q_2}{dt^2}=\frac{\partial^2 Y_0}{\partial t^2}+\epsilon\left(2\frac{\partial^2 Y_0}{\partial T\partial t}+\frac{\partial^2 Y_1}{\partial t^2}\right)+O(\epsilon^2). \tag{3.6}$$

Substituting Eqs. (3.5) and (3.6) into Eqs. (3.3) and (3.4) and collecting powers of ϵ gives

$$\frac{\partial^2 X_0}{\partial t^2}=-\omega_1^2 X_0, \tag{3.7}$$

$$\frac{\partial^2 Y_0}{\partial t^2}=-\omega_2^2 Y_0, \tag{3.8}$$

$$2\frac{\partial^2 X_0}{\partial T\partial t}+\frac{\partial^2 X_1}{\partial t^2}=-\omega_1^2 X_1+A_1X_0^2+A_2Y_0^2+A_3X_0Y_0, \tag{3.9}$$

$$2\frac{\partial^2 Y_0}{\partial T\partial t}+\frac{\partial^2 Y_1}{\partial t^2}=-\omega_2^2 Y_1+B_1X_0^2+B_2Y_0^2+B_3X_0Y_0. \tag{3.10}$$

The general solutions to Eqs. (3.7) and (3.8) are given by

$$X_0=q_1(T)e^{i\omega_1 t}+q_1^*(T)e^{-i\omega_1 t}, \tag{3.11}$$

$$Y_0=q_2(T)e^{i\omega_2 t}+q_2^*(T)e^{-i\omega_2 t}. \tag{3.12}$$

Using Eqs. (3.11) and (3.12) in Eq. (3.9), we have

$$
\begin{aligned}
&2i\omega_1 e^{i\omega_1 t}\frac{dq_1}{dT} - 2i\omega_1 e^{-i\omega_1 t}\frac{dq_1^*}{dT} + \frac{\partial^2 X_1}{\partial t^2} = -\omega_1^2 X_1 \\
&+ A_1\left({q_1}^2 e^{2i\omega_1 t} + 2q_1 q_1^* + {q_1}^{*2} e^{-2i\omega_1 t}\right) \\
&+ A_2\left({q_2}^2 e^{2i\omega_2 t} + 2q_2 q_2^* + {q_2}^{*2} e^{-2i\omega_2 t}\right) \\
&+ A_3\left(q_1 q_2 e^{i(\omega_1+\omega_2)t} + q_1 q_2^* e^{i(\omega_1-\omega_2)t} + q_1^* q_2 e^{-i(\omega_1-\omega_2)t} + q_1^* q_2^* e^{-i(\omega_1+\omega_2)t}\right).
\end{aligned}
\tag{3.13}
$$

Equation (3.13) will give solutions that grow in time, unless we set

$$
2i\omega_1 \frac{dq_1}{dT} = A_3 q_1^* q_2 e^{iT}. \tag{3.14}
$$

Similarly, substituting Eqs. (3.11) and (3.12) into Eq. (3.10) gives

$$
\begin{aligned}
&2i\omega_2 e^{i\omega_2 t}\frac{dq_2}{dT} - 2i\omega_2 e^{-i\omega_2 t}\frac{dq_2^*}{dT} + \frac{\partial^2 Y_1}{\partial t^2} = -\omega_2^2 Y_1 \\
&+ B_1\left({q_1}^2 e^{2i\omega_1 t} + 2q_1 q_1^* + {q_1}^{*2} e^{-2i\omega_1 t}\right) \\
&+ B_2\left({q_2}^2 e^{2i\omega_2 t} + 2q_2 q_2^* + {q_2}^{*2} e^{-2i\omega_2 t}\right) \\
&+ B_3\left(q_1 q_2 e^{i(\omega_1+\omega_2)t} + q_1 q_2^* e^{i(\omega_1-\omega_2)t} + q_1^* q_2 e^{-i(\omega_1-\omega_2)t} + q_1^* q_2^* e^{-i(\omega_1+\omega_2)t}\right).
\end{aligned}
\tag{3.15}
$$

Following similar procedures as above, Eq. (3.15) gives

$$
2i\omega_2 \frac{dq_2}{dT} = B_1 q_1^2 e^{-iT}. \tag{3.16}
$$

Expressing q_1 and q_2 in polar form as $q_1 = q_1(T)e^{iT}$ and $q_2 = q_2(T)e^{iT}$, then

$$\frac{dq_1}{dT} = \frac{dq_1(T)}{dT}e^{iT} + iq_1(T)e^{iT}, \tag{3.17}$$

$$\frac{dq_2}{dT} = \frac{dq_2(T)}{dT}e^{iT} + iq_2(T)e^{iT}. \tag{3.18}$$

Using Eqs. (3.17) and (3.18) in Eqs. (3.14) and (3.16), we have the following system

$$i\frac{dq_1(T)}{dT} = q_1(T) + \widetilde{A}q_1^*q_2 \tag{3.19}$$

$$i\frac{dq_2(T)}{dT} = q_2(T) + \widetilde{B}q_1^2 \tag{3.20}$$

where $\widetilde{A} = \frac{A_3}{2\omega_1}$ and $\widetilde{B} = \frac{B}{2\omega_2}$. The initial conditions of Eqs. (3.19)-(3.20) are

$$q_1(0) = \frac{Q_1(0)}{2}, \tag{3.21}$$

$$q_2(0) = 0. \tag{3.22}$$

We note that parameters $\tilde{A}$ and $\tilde{B}$ depend on τ.

In Fig. 3.5, we plot these parameters as a function of τ for $N = 64$ particles and 100 realisations. These realisations have been computed by fixing τ and then opting for 100 sets of $N = 64$ randomly generated numbers from the Gaussian distribution with mean 1 and standard deviation $\sigma = 1/3 \times 0.01\tau$. Therefore, the v_js in the 100 sets lie in the interval $[1-0.01\tau, 1+0.01\tau]$. As we can see in panel (a), $\tilde{A}$ is positive for all τ, whereas $\tilde{B}$ changes sign at around $\tau = 10\%$. Particularly, $\tilde{B}$ starts positive for small τ values before it becomes negative at around $\tau = 10\%$. By using polynomial regression, we have been able to fit the mean of the 100 realisations in panel (b) by the function $\tilde{B} \approx -0.00893\tau^2 - 0.000084\tau + 0.90728$, with a sum of square errors (SSE) of 3.46×10^{-19}. This allowed us to estimate with good accuracy the threshold for the percentage of variability where $\tilde{B}$ changes sign and found to be given by $\tau_c \approx 10.0749\%$ as $\tilde{B}(\tau_c) = 0$. In Sec. 3.2.2, we show that when $\tilde{B} < 0$, that is for $\tau > \tau_c$, trajectories of Eqs. (2.39) may blow up in finite time.

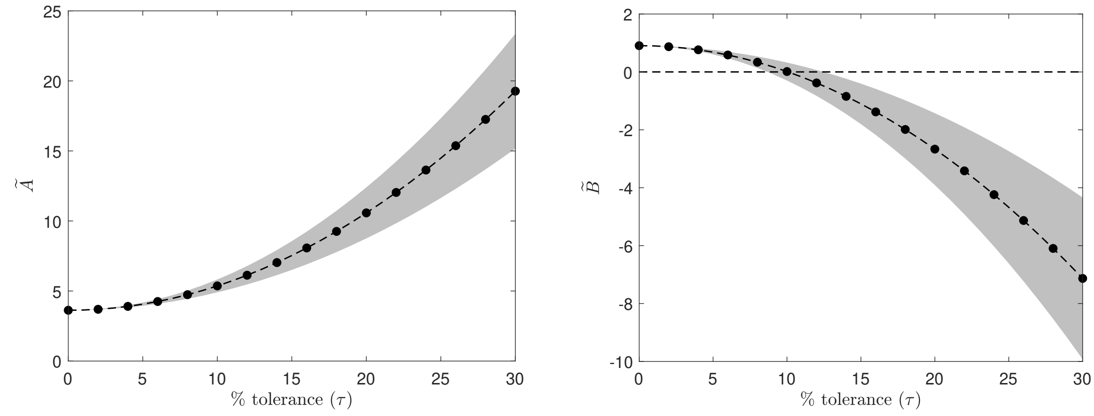

(a) **(b)**

Figure 3.5. Plot of $\tilde{A}$ (in panel (a)) and $\tilde{B}$ (in panel (b)) as a function of the tolerance obtained numerically for $N = 64$. The dash-dotted curve is the mean value over 100 realisations of the same percentage of variability (see the discussion in the text), while the lengths of the shaded regions are two standard deviations. Using a polynomial regression, the mean is found to be given approximately by $\tilde{A} \approx 0.01739\tau^2 - 0.00029\tau + 3.62805$ and $\tilde{B} \approx -0.00893\tau^2 - 0.000084\tau + 0.90728$, where the sums of square errors are 2.14×10^{-15} and 3.46×10^{-19} in panels (a) and (b), respectively. Note the horizontal black dashed line at $\tilde{B} = 0$ from which τ_c is derived (see text for details).

A comparison of the dynamics of the normal modes Q_1 and Q_2 of Eqs. (3.3)-(3.4) and those of the slow-time variables q_1 and q_2 of Eqs. (3.19)-(3.20) is shown in Fig. 3.6, where one can see that q_j is an envelope of Q_j for $j = 1, 2$.

Next we explain the cause of localisation with the increase of the percentage of variability τ. Note that from Eqs. (3.20), there can be transfer of energy from $q_1(t)$ to $q_2(t)$ through the nonlinear coupling coefficient $\tilde{B}$. Panel (b) in Fig. 3.5 shows that $\tilde{B}$ decreases from positive values with the increase of τ until $\tau = \tau_c$, after which it becomes negative. When $\tilde{B}$ vanishes at $\tau = \tau_c$, there is no transfer of energy and hence localisation. In the following, we will also show that when $\tilde{B} < 0$, i.e., for $\tau > \tau_c$, there might be unbounded trajectories that blow up in finite time.

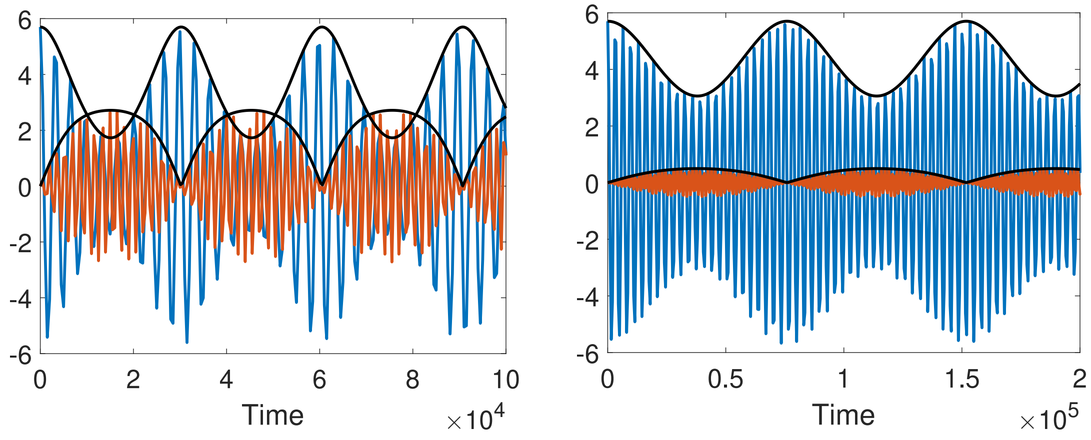

(a) **(b)**

Figure 3.6. Time evolution of the normal mode variables Q_1 (blue curve) and Q_2 (red curve) with their envelopes q_1 and q_2 (black curves) from Eqs. (3.20) for $\tau = 0\%$ in panel (a) and $\tau = 10\%$ in panel (b). Note that in both panels $\tau < \tau_c$, so trajectories do not blow up.

3.2.2 Equilibrium solutions

We start by analysing the standing wave solutions of the envelope equations (3.20). To do so, it is convenient to write q_1 and q_2 in polar form $q_1 = r_1 e^{i\phi_1}$ and $q_2 = r_2 e^{2i\phi_2}$, where $r_1 = |q_1|$, $r_2 = |q_2|$. Then, we define the new variables

$$P = r_1^2 + r_2^2, \tag{3.23a}$$

$$\Delta = r_1^2 - r_2^2, \tag{3.23b}$$

$$\theta = \phi_2 - \phi_1. \tag{3.23c}$$

Differentiating Eqs. (3.23a)-(3.23c) gives

$$\dot{P} = 2r_1\dot{r_1} + 2r_2\dot{r_2}, \tag{3.24a}$$

$$\dot{\Delta} = 2r_1\dot{r_1} - 2r_2\dot{r_2}, \tag{3.24b}$$

$$\dot{\theta} = \dot{\phi_2} - \dot{\phi_1}. \tag{3.24c}$$

Moreover, using the product rule for differentiation, we obtain

$$\dot{q_1} = \dot{r_1} e^{i\phi_1} + i r_1 \dot{\phi_1} e^{i\phi_1}, \tag{3.25a}$$

$$\dot{q_2} = \dot{r_2} e^{2i\phi_2} + 2 i r_2 \dot{\phi_2} e^{2i\phi_2}. \tag{3.25b}$$

Substituting Eqs. (3.25) into Eqs. (3.19)-(3.20) yields

$$i\dot{r_1} - r_1\dot{\phi_1} = r_1 + \widetilde{A} r_1 r_2 e^{2i(\phi_2-\phi_1)}, \tag{3.26a}$$

$$i\dot{r_2} - 2r_2\dot{\phi_2} = r_2 + \widetilde{B} r_1^2 e^{-2i(\phi_2-\phi_1)}. \tag{3.26b}$$

Collecting real and imaginary parts of Eqs. (3.26) and recalling θ in Eq. (3.23c), we have

$$\dot{r_1} = \widetilde{A} r_1 r_2 \sin(2\theta), \tag{3.27a}$$

$$\dot{r_2} = -\widetilde{B} r_2^2 \sin(2\theta), \tag{3.27b}$$

$$\dot{\theta_1} = -1 - \widetilde{A} r_2 \cos(2\theta), \tag{3.27c}$$

$$\dot{\theta_2} = -\frac{r_2 + \widetilde{B} r_1^2 \cos(2\theta)}{2r_2}. \tag{3.27d}$$

Substituting Eqs. (3.27) into Eqs. (3.24) and noting that

$$r_1 = \sqrt{\frac{P+\Delta}{2}}, \tag{3.28a}$$

$$r_2 = \sqrt{\frac{P-\Delta}{2}}, \tag{3.28b}$$

we have the following system of first order differential equations (a similar derivation can be seen in [60])

$$\dot{P} = \frac{\widetilde{A}-\widetilde{B}}{\widetilde{A}+\widetilde{B}}\dot{\Delta}, \tag{3.29a}$$

$$\dot{\Delta} = \frac{\sqrt{2(P-\Delta)}\sin(2\theta)(P+\Delta)\left(\widetilde{A}+\widetilde{B}\right)}{2}, \tag{3.29b}$$

$$\dot{\theta} = -\frac{2\widetilde{A}\cos(2\theta)(\Delta-P)+\widetilde{B}\cos(2\theta)(\Delta+P)-\sqrt{2(P-\Delta)}}{2\sqrt{2(P-\Delta)}}. \tag{3.29c}$$

From Eq. (3.29a), we define the constant of motion C as

$$C = P - \frac{\widetilde{A}-\widetilde{B}}{\widetilde{A}+\widetilde{B}}\Delta.$$

First, we will study the stability of the equilibrium points of the reduced system given in Eqs. (3.29b), (3.29c). Then we will discuss the stability of the equilibrium points of its corresponding system in Eqs. (3.19)-(3.20). To study the reduced system of Eqs. (3.29b), (3.29c), we restrict the phase difference θ in the interval $0 \leq \theta < \pi$ and obtain two equilibrium points, namely (θ_j, Δ_j), $j = 1,2$. The θ_j equilibria depend on $\tilde{A}$ and $\tilde{B}$, and are given by

1. if $\tilde{A} > 0$ and $\tilde{B} > 0$ or $\tilde{A} < 0$ and $\tilde{B} < 0$, then $\theta_1 = 0$ and $\theta_2 = \pi/2$,
2. if $\tilde{A} > 0$ and $\tilde{B} < 0$, then $\theta_1 = \theta_2 = \pi/2$, and
3. if $\tilde{A} < 0$ and $\tilde{B} > 0$, then $\theta_1 = \theta_2 = 0$.

Furthermore, the Δ_j equilibrium points, for $j = 1,2$, are

$$\Delta_j = \frac{\left(6\widetilde{A}^2C - 3\widetilde{A}\widetilde{B}C - (-1)^j\sqrt{1+6\widetilde{A}\left(\widetilde{A}+\widetilde{B}\right)C} - 1\right)\left(\widetilde{A}+\widetilde{B}\right)}{18\widetilde{A}^2\widetilde{B}}. \tag{3.30}$$

Next, we study the stability of the equilibrium points, which is determined by the eigenvalues of the Jacobian matrix of Eqs. (3.29b), (3.29c), evaluated at the equilibrium points, i.e., by

$$\lambda_{1,2}^{(j)} = \pm \frac{\sqrt{-3-18\widetilde{A}^2C-18\widetilde{A}\widetilde{B}C+6(-1)^j\sqrt{1+6\widetilde{A}\left(\widetilde{A}+\widetilde{B}\right)C}}}{3}. \tag{3.31}$$

Equation (3.30) implies that the equilibrium points exist when

$$1+6\widetilde{A}\left(\widetilde{A}+\widetilde{B}\right)C \geq 0. \tag{3.32}$$

Using the initial conditions in Eq. (3.21), Eq. (3.32) becomes

$$1+12\widetilde{A}\widetilde{B}r_1^2 \geq 0.$$

Therefore, the threshold for the existence of the equilibrium points is given by

$$1+12\widetilde{A}\widetilde{B}r_1^2 = 0,$$

which is the blue curve in Fig. 3.7. The solid and dashed lines represent the curve below and above the line $\widetilde{A}+\widetilde{B}=0$, respectively. The black dashed line represents the line $\widetilde{A}+\widetilde{B}=0$.

When the equilibrium points exist, the eigenvalues given in Eq. (3.31) are either real or purely imaginary, indicating that the equilibrium points are saddle nodes or centres. Using the initial conditions in Eqs. (3.21), the thresholds that separate between real and purely imaginary eigenvalues are

$$1 + 12\widetilde{A}\widetilde{B}r_1^2 = 0, \tag{3.33}$$

$$1 - 4\widetilde{A}\widetilde{B}r_1^2 = 0. \tag{3.34}$$

We plot in Fig. 3.7, Eqs. (3.33) and (3.34) as blue and red curves, respectively.

System (3.29) with parameter values $\widetilde{A}$ and $\widetilde{B}$ above the red curve in the first quadrant or below the red curve in the third quadrant in Fig. 3.7 has two equilibria given in Eq. (3.30), which are both centres, and are therefore stable. Conversely, if both parameters lie between the two red curves, then one equilibrium is a centre while the other is a saddle node.

Next, we will discuss the stability of the equilibrium points of Eqs. (3.19)-(3.20). As this system can be transformed into Eqs. (3.29b) and (3.29c) in terms of Δ and θ, we utilise Eqs. (3.29b) and (3.29c) to describe the dynamics of Eqs. (3.19)-(3.20). Equations (3.29) are obtained from Eqs. (3.19)-(3.20) by using Eqs. (3.23), where both r_1 and r_2 are non-negative real numbers. Equations (3.29) require $P - \Delta > 0$ in order to have real solutions, whereas Eq. (3.23) requires $P - \Delta \geq 0$ and $P + \Delta \geq 0$, otherwise r_1 and r_2 are complex numbers. The region that fulfils these two inequalities is referred to as the well-defined region, and it is represented by the shaded area in Fig. 3.7. For instance, the well-defined region in the first quadrant is bounded. There are two equilibrium points in the region above the red curve, while there is only one in the region below it. This means that Eqs. (3.19)-(3.20) and (3.29) have two equilibrium points in the region above the red curve, whereas they share only one equilibirum point in the region below it as Δ_2 lies outside the shaded region. To determine the boundary for Δ in the well-defined region, we solve the inequalities $P-\Delta > 0$ and $P+\Delta \geq 0$, which depend on $\widetilde{A}$ and $\widetilde{B}$, as follows:

- if $\frac{\widetilde{A}-\widetilde{B}}{\widetilde{A}+\widetilde{B}} \geq 1$, then $\Delta > \max\left\{\Delta^1_{\text{crit}}, \Delta^2_{\text{crit}}\right\}$, where

$$\Delta^1_{\text{crit}} = \frac{C\left(\widetilde{A}+\widetilde{B}\right)}{2\widetilde{B}} \text{ and } \Delta^2_{\text{crit}} = -\frac{C\left(\widetilde{A}+\widetilde{B}\right)}{2\widetilde{A}},$$

- if $-1 \leq \frac{\widetilde{A}-\widetilde{B}}{\widetilde{A}+\widetilde{B}} < 1$, then $\Delta^2_{\text{crit}} \leq \Delta < \Delta^1_{\text{crit}}$, and
- If $\frac{\widetilde{A}-\widetilde{B}}{\widetilde{A}+\widetilde{B}} < -1$, then $\Delta < \min\left\{\Delta^1_{\text{crit}}, \Delta^2_{\text{crit}}\right\}$.

All types of well-defined regions in $(\tilde{A},\tilde{B})$-plane are depicted in Fig. 3.7.

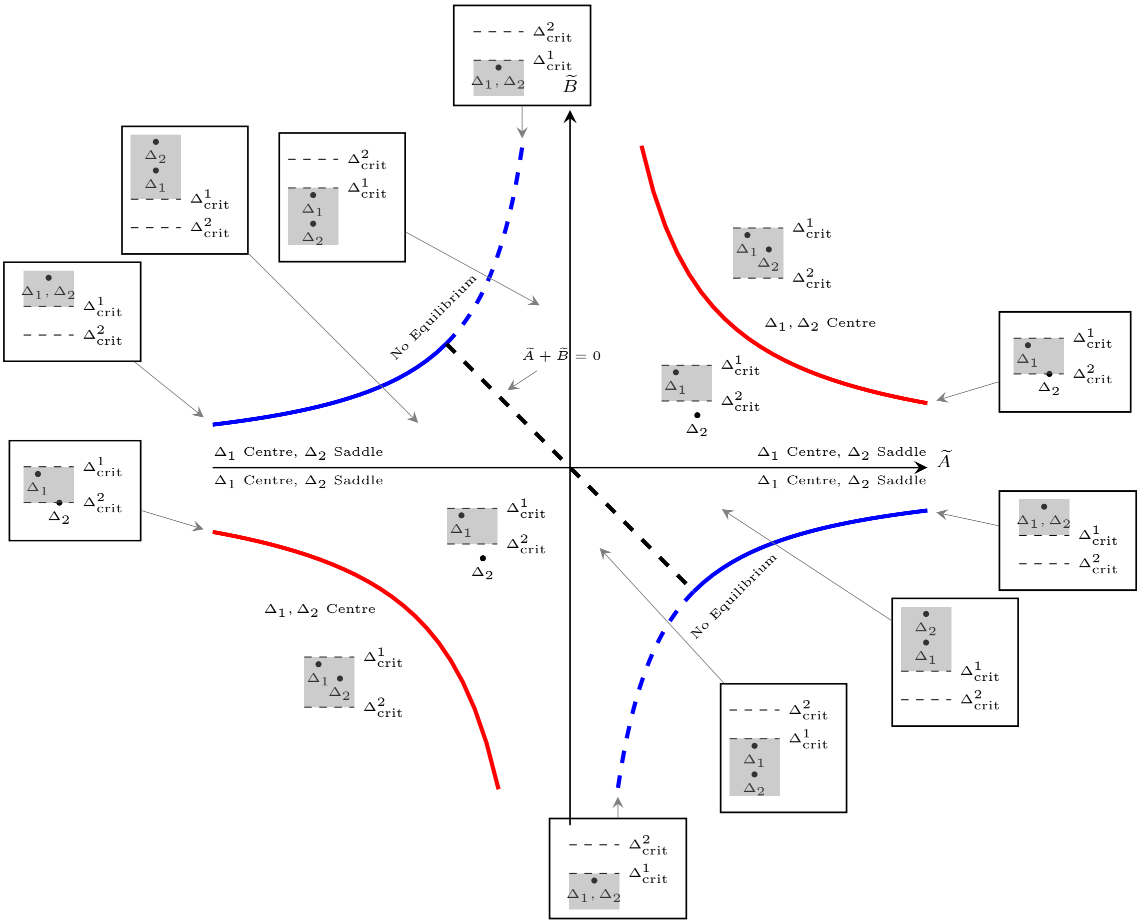

Figure 3.7. Bifurcation diagram of the equilibrium points Δ_1 and Δ_2 and the regions where the dynamics of system (3.29) is well-defined (see text for more details).

System (3.29) with parameter values above the red curve in Fig. 3.7 is bounded, with Δ^1_{crit} and Δ^2_{crit} being the upper and lower bounds, respectively. The two equilibrium points given in Eq. (3.30) are both centres, and are therefore stable. When the parameter values lie on the red curve, $\Delta_2 = \Delta^2_{\text{crit}}$. Furthermore, if the parameter values are below the red curve and $\widetilde{B} > 0$, system (3.29) is still bounded, but it only shares one equilibrium point Δ_1 with system (3.20), whereas Δ_2 does not belong to the well-defined region. Equation (3.29), on the other hand, is unbounded when $\widetilde{B} < 0$. In this case, it either extends to $\Delta \to \infty$ or $-\infty$ and depending on the value of $\frac{\widetilde{A}-\widetilde{B}}{\widetilde{A}+\widetilde{B}}$, Δ_1 can be a centre and Δ_2 a saddle node in this region. Additionally, the system has only one equilibrium point on the blue curve.

Based on the data shown Fig. 3.5, we have computed numerically the parameter values for Eqs. (3.19)-(3.20). Our findings indicate that the values of $\widetilde{A}$ are consistently positive, but $\widetilde{B}$ can have either positive or negative values. Hence, Eqs. (3.19)-(3.20) are restricted to the first and fourth quadrants in Fig. 3.7. Additionally, we present the location of the equilibrium point (θ_j, Δ_j) and their nature in Fig. 3.7. We also plot the values of Δ_j in Fig. 3.8. To better visualise Δ_2 as it approaches infinity when $\widetilde{A}$ or $\widetilde{B}$ approaches zero, we plot in Fig. 3.8 (b) $\tanh(\Delta_2/100)$ instead of Δ_2.

In the following, we illustrate the phase portrait of the reduced system of Eqs. (3.29b), (3.29c) for different percentages of variability τ, which correspond to different values of $\tilde{A}$ and $\tilde{B}$. When there is no variability (i.e., for $\tau = 0\%$), the parameter values are $\widetilde{A} = 3.63$ and $\widetilde{B} = 0.91$ and the equilibrium points are $(\theta_1, \Delta_1) = (0, 5.09)$ and $(\theta_2, \Delta_2) = (\pi/2, 4.34)$. Both are stable and the phase space in this case is shown in Fig. 3.9(a). As we can see in panel (b) in Fig. 3.5, as τ

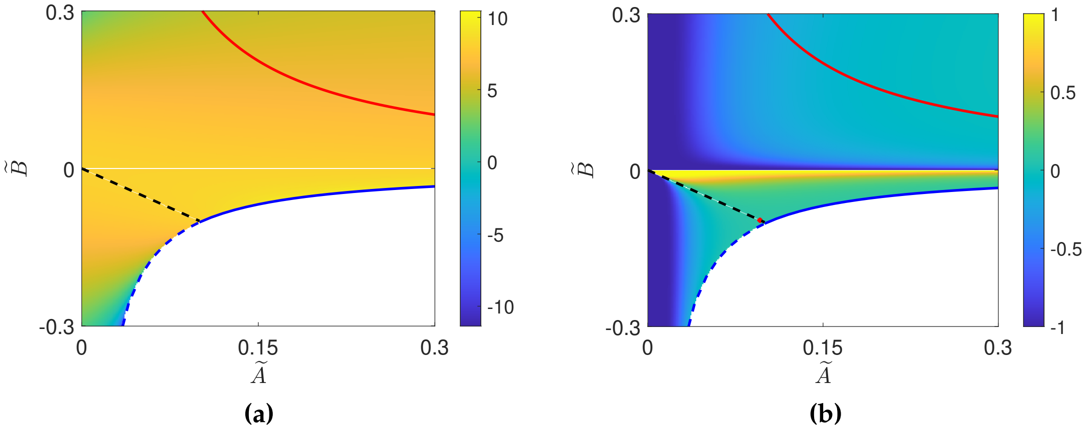

Figure 3.8. Plot of (a) Δ_1 and (b) $\tanh(\Delta_2/100)$ as a function of $\widetilde{A}$ and $\widetilde{B}$. In panel (a), the color bar denotes the values of Δ_1 and in panel (b), the values of $\tanh(\Delta_2/100)$. The black dashed, red and blue curves are discussed in the text and are the same with those in Fig. 3.7.

increases, $\widetilde{B}$ decreases and becomes negative for $\tau > \tau_c$. The parameter values for $\tau = 10\%$ variability are $\widetilde{A} = 4.97$ and $\widetilde{B} = 0.05$ and the equilibrium points are $(\theta_1, \Delta_1) = (0, 6.27)$ and $(\theta_2, \Delta_2) = (\pi/2, 4.08)$. Similar to the previous case, both equilibrium points are stable and the phase space is shown in Fig. 3.9(b). Note that for the initial conditions (3.22), we have that

$$\lim_{\widetilde{B}\to 0} \Delta^1_{\text{crit}} = r_1^2, \quad \lim_{\widetilde{B}\to 0} \Delta^2_{\text{crit}} = 0,$$

which shows that Δ becomes positive as we increase τ. Indeed, $\Delta > 0$ corresponds to energy localisation as the magnitude of q_1 remains larger than q_2.

As we can see in Fig. 3.10 for $\tau \approx 10.0833\% > \tau_c$, $\widetilde{B}$ is negative ($\widetilde{B} = -0.0015$) and the region in the (Δ, θ)-space becomes unbounded (see also Fig. 3.7). It extends to either $\Delta \to \infty$ or $-\infty$ and depends on $\widetilde{A}$. In this case, the two equilibrium points are $(\theta_1, \Delta_1) = (\pi/2, 9.1274)$, which is a (stable) center, and $(\theta_2, \Delta_2) = (\pi/2, 15.4383)$, which is a (unstable) saddle point. The plot shows that in this case, one may obtain bounded solutions as well as unbounded ones, depending on the initial condition.

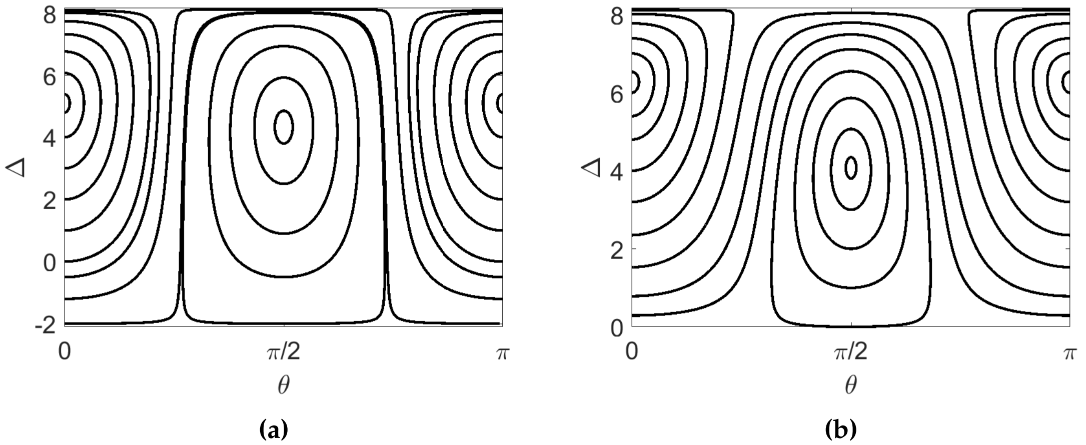

Figure 3.9. Phase portraits of the reduced system of Eqs. (3.29b), (3.29c) for (a) $\tau = 0\%$ percentage of variability and (b) $\tau = 10\%$ percentage of variability.

For example, the initial condition of Eqs. (2.45) (or Eqs. (3.21), (3.22)) results in θ and Δ values in the unbounded region in Fig. 3.10, where the trajectory is shown as the blue curve and starts at the bottom of the plot.

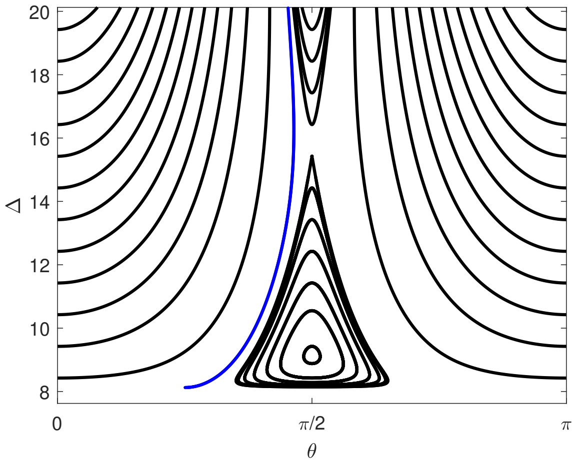

Figure 3.10. The same as Fig. 3.9, where the parameter values are $\widetilde{A} = 5.3932$ and $\widetilde{B} = -0.0015$, which correspond to $\tau \approx 10.0833\% > \tau_c$. The blue curve is the trajectory of the initial condition in Eqs. (3.21), (3.22).

3.3 Chaotic behaviour

Energy recurrences arise in the homogeneous FPUT lattice (2.38) when the system remains in the quasi-stationary state for an extremely long time, making the approach to equipartition of energy unobservable. This state is characterised by an energy concentration on low-frequency modes that appears to be stable for a very long time [61]. In the quasi-stationary state, the FPUT lattice can be viewed as the perturbation of the regular, integrable Toda lattice [62].

Here we study the effect of variability on the chaotic properties of system (3.1). Particularly, we consider lattices of $N = 4, 8, 16, 32, 64$ particles in systems (2.38) (homogeneous, no variability) and (3.1) (with variability) and use the mLE [32] and SALI [34, 35] to discriminate between regular and chaotic dynamics. We want to see if energy localisation in the first normal mode that we observed in Sec. 3.2 for $\tau = 10\% < \tau_c$ corresponds to chaotic dynamics, by increasing τ from 0 to 10%. We utilise Algorithm 2 to calculate the mLE and Algorithm 3 to compute SALI. These algorithms provide a systematic approach for obtaining these important chaotic indicators, allowing us to analyse and quantify the dynamics of the system under investigation.

First, we consider the case without variability, that is the FPUT$-\alpha$ system (2.38). We integrate the equations of motion (2.39) and its corresponding variational equations by using the tangent-map method [37] and Yoshida's fourth order symplectic integrator [26]. We have found that a time step of 0.01 keeps the relative energy error below 10^{-9}. In all our computations, the final integration time is $t = 10^8$. Here, we use the same initial condition in Eq. (2.45) for all N. This initial condition then results in different energies for different N, i.e., $E = 0.4775$ for $N = 4$, $E = 0.2714$ for $N = 8$, $E = 0.1447$ for $N = 16$, $E = 0.0747$ for $N = 32$, and $E = 0.0379$ for $N = 64$. Our results in Fig. 3.11 show that all trajectories for $N = 4, 8, 16, 32, 64$ are regular up to $t = 10^8$, corroborated by the tendency of the mLEs to converge to zero following the $1/t$ law and SALI to tend to fixed positive values, shown in panels (a) and (b), respectively. These results are in agreement with the fact that energy recurrences in the homogeneous FPUT lattice (2.38) arise when it remains in the quasi-stationary state for extremely long times, making the approach to equipartition of energy unobservable.

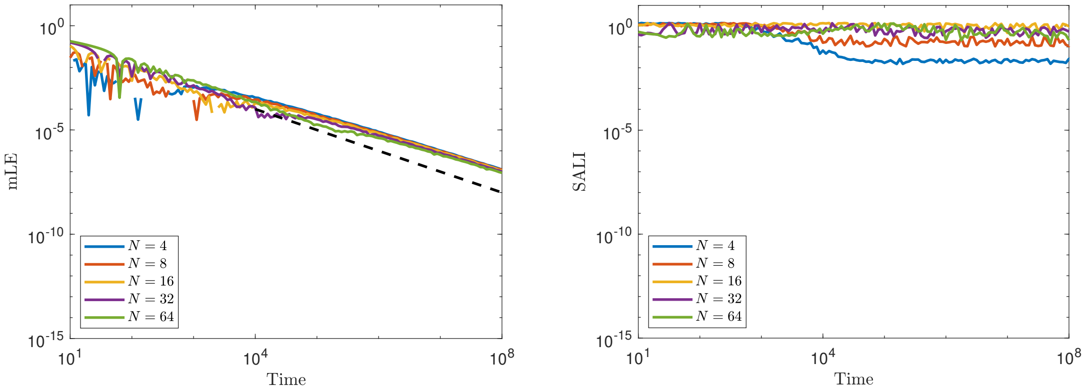

(a) **(b)**

Figure 3.11. Plot of mLE (panel a)) and SALI (panel b)) in time for a range of N values seen in the insets (denoted by different colours) in the absence of variability, i.e., of the FPUT system (2.38). Note that all axes are logarithmic. The black dashed line in panel (a) is the law $1/t$ of regular trajectories to guide the eye.

Finally, we look at the case of $\tau = 10\% < \tau_c$, for which we have observed almost energy localisation in the first normal mode in Sec. 3.2. Since in this case we only know the equations of motion (3.1), we integrated them using the DOP853 integrator [36], an explicit Runge-Kutta method of order 8 due to Dormand and Prince, to achieve good numerical accuracy. We compute the chaotic indicators for 30 realisations of the same percentage of variability $\tau = 10\%$, while keeping the initial conditions fixed for each number of particles N. For $N = 4$ and 8, all trajectories in panels (a)-(d) in Fig. 3.12 appear to be regular up to final integration time $t = 10^8$, corroborated by the tendency of the mLEs to converge to zero following the $1/t$ law and SALI to tend to fixed positive values. However, for $N = 16$, two of the 30 trajectories in panels (e), (f) in Fig. 3.13 are chaotic as their mLEs converge to positive values at $t = 10^8$ and their SALI decrease to zero exponentially fast. Figure 3.13 shows that there are more chaotic orbits than those for the smaller values of N in Fig. 3.12. We show the percentage of chaotic trajectories (out of the 30 realisations) as a function of N in Fig. 3.14, where the increase from $N = 4,8,16$ to $N = 32,64$ is apparent. These results suggest that in the case of almost complete energy localisation, variability promotes chaos in the system as the number of particles increases. However, further studies are required to determine whether the increase is monotone.

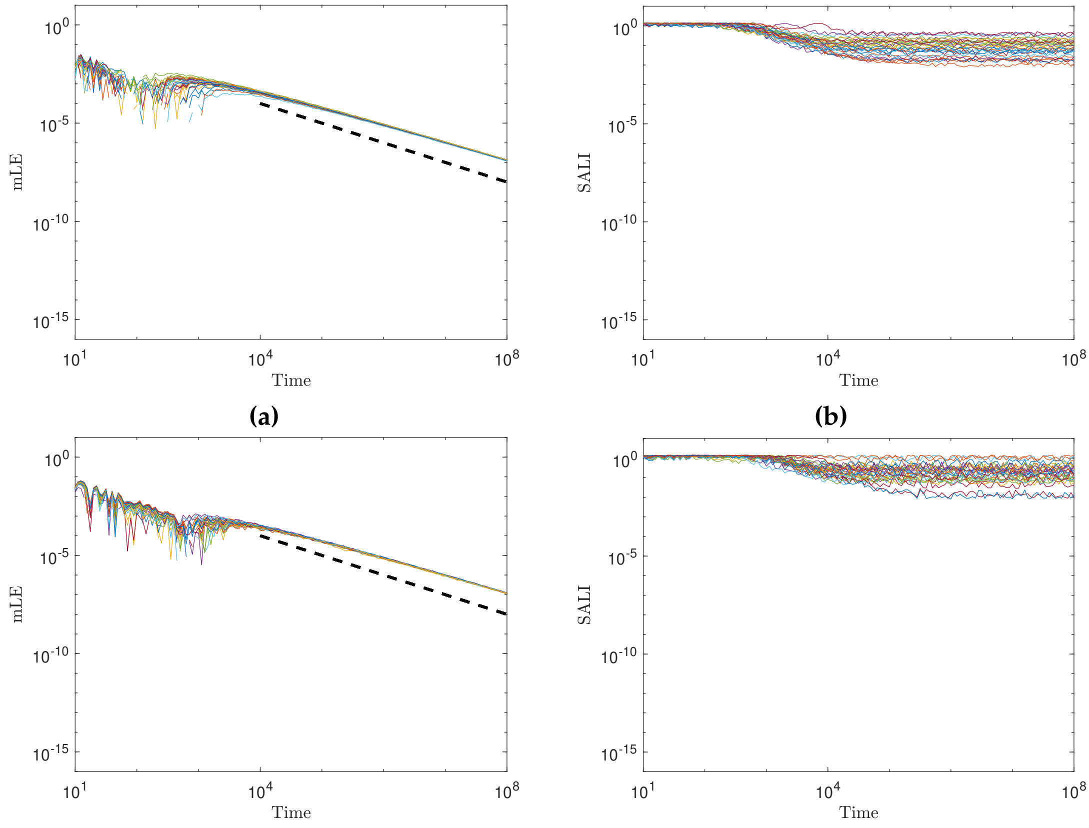

(a) **(b)** **(c)** **(d)**

Figure 3.12. Plot of mLE (panels (a), (c)) and SALI (panels (b), (d)) in time for 30 trajectories (denoted by different colors) and $\tau = 10\%$ (see Eq. (3.1)). Panels (a), (b) are for $N = 4$ and panels (c), (d) for $N = 8$. Note that all axes are logarithmic. The black dashed lines in panels (a), (c) are the law $1/t$ of regular trajectories to guide the eye.

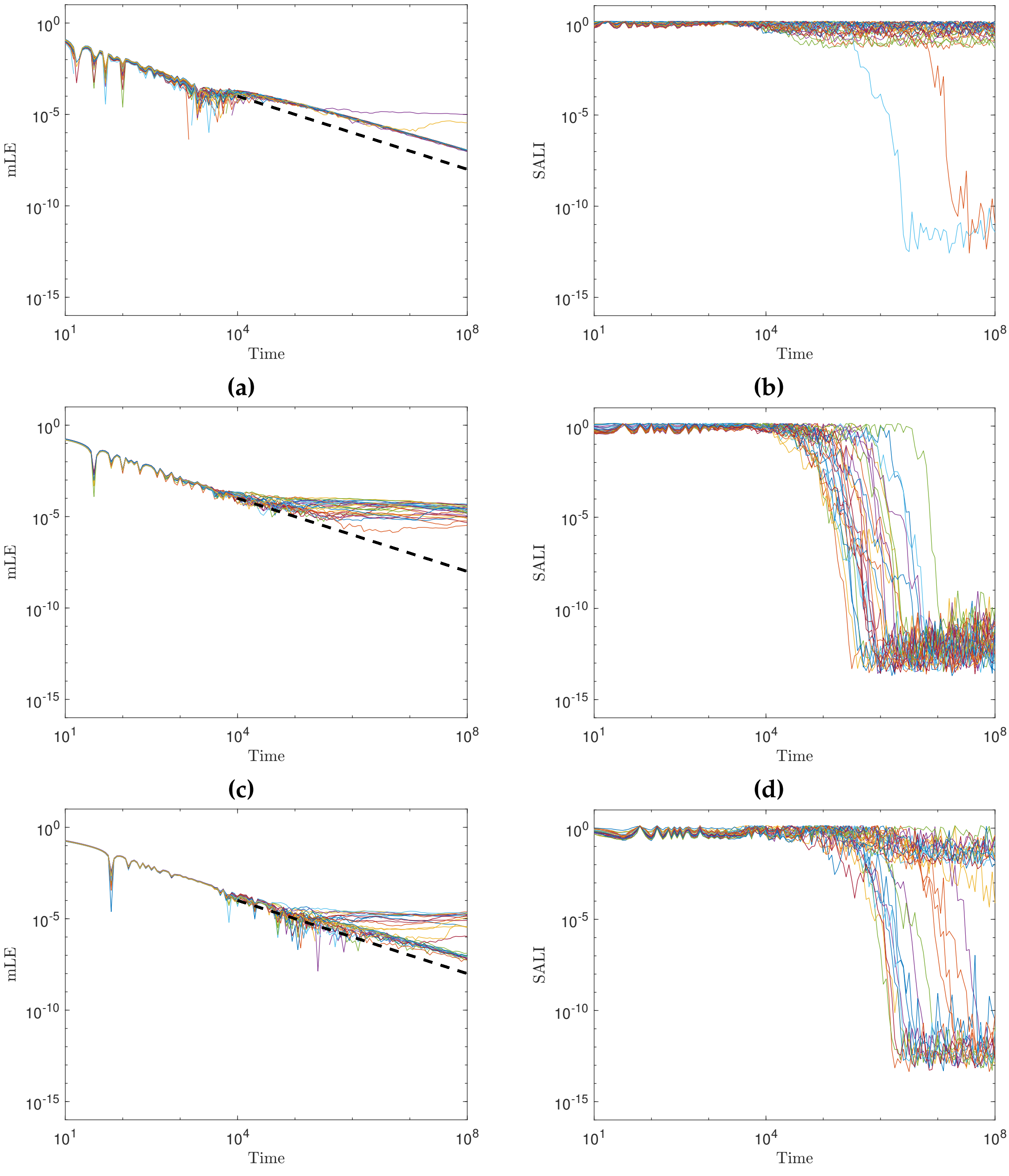

(a) **(b)**

(c) **(d)**

(e) **(f)**

Figure 3.13. Plot of mLE (panels (a), (c), (e)) and SALI (panels (b), (d), (f)) in time for 30 trajectories (denoted by different colors) and $\tau = 10\%$ (see Eq. (3.1)). Panels (a), (b) are for $N = 16$, panels (c), (d) for $N = 32$ and panels (e), (f) for $N = 64$. Note that all axes are logarithmic. The black dashed lines in panels (a), (c) are the law $1/t$ of regular trajectories to guide the eye.

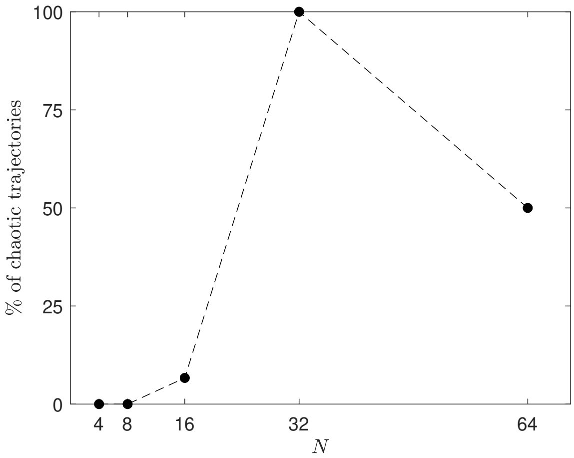

Figure 3.14. Percentage of chaotic trajectories as a function of N for 30 realisations of variability with $\tau = 10\%$. The black-dash line segments connect the black points and are there to guide the eye.

3.4 Conclusions

In this chapter, we have studied a disordered FPUT-α system, considering variability in its parameters to account for inherent manufacturing processes. By employing a two normal-mode approximation, we have successfully explained the underlying mechanism behind energy localisation and the occurrence of solution blow-ups when the percentage of variability surpasses a certain threshold, which we have computed using the theory we developed.

Furthermore, we have delved into the impact of variability on the chaotic behaviour of the system, quantifying it through the calculation of the mLE and SALI. Through numerous realisations at the same percentage of variability corresponding to energy localisation, we have observed that trajectories tend to exhibit chaotic behaviour more frequently as the number of particles N increases, provided the variability remains below the threshold.

Notably, we have not only confirmed the well-known result that variability leads to energy-recurrence breakdown and energy localization studied in [57], but we have also made a significant new discovery. By systematically increasing the percentage of variability beyond the threshold determined by our theory, we have found that the system's solutions may undergo finite-time blow-ups. This intriguing phenomenon arises because we considered the equations of motion without a Hamiltonian, which would otherwise ensure the system's energy conservation throughout the dynamics.

In the next chapter, we will delve into the investigation of the Hamiltonian model with heterogeneity, which promises to unveil further insights into the system's behaviour.

Chapter 4

Hamiltonian FPUT-α lattices with variability

In a nonintegrable Hamiltonian system, energy plays a crucial role in determining the behaviour and dynamics of the system. The Hamiltonian, which represents the total energy of the system, is a fundamental (conserved) quantity that governs the system's evolution.

The energy of a Hamiltonian system is typically composed of two components, the kinetic energy and the potential energy. The kinetic energy is associated with the system's motion, while the potential energy captures the interactions and forces within the system. One fundamental characteristic of Hamiltonian systems is the conservation of energy. The total energy, given by the Hamiltonian, remains constant throughout the system's evolution unless there are external influences or dissipation mechanisms.

Energy can be transferred between different degrees of freedom within the system. For example, in a coupled oscillator system, energy can be exchanged between different oscillators, leading to phenomena such as resonances or energy localisation [29]. Additionally, dissipation mechanisms, such as damping or friction, can cause energy to gradually dissipate from the system, leading to decreasing amplitude in time.

The energy level of a Hamiltonian system affects its trajectory in the phase space. The phase space represents the set of all possible system states, and the trajectory traces a path in this space as it evolves. Different energy levels can result in distinct trajectories, exhibiting a range of behaviours such as periodic, quasi-periodic, weakly chaotic, and chaotic.

In this chapter, our focus is on examining the disordered FPUT-α system, where variability is introduced into the Hamiltonian function [57]. We are specifically interested in understanding the impact of variability on the behaviour of the system.

One aspect we explore is the lack of energy recurrence in the system as the percentage of variability increases while maintaining a fixed energy level. Energy recurrence refers to the phenomenon where a system returns to its initial energy configuration after a certain period of time and we have seen it in Chapter 3. By systematically increasing the percentage of variability in the system, we investigate how this affects the occurrence of energy recurrence. This analysis provides insights into how the introduction of variability disrupts the regular behaviour of the system and influences its long-term energy dynamics.

Furthermore, we delve into the chaotic behaviour of the disordered FPUT-α system. To quantify chaos, we employ the concept of mLE and SALI. By calculating these chaotic indicators for varying degrees of variability in the system, we assess how the introduction of variability impacts the chaoticity in the system. This examination allows us to understand how the system's sensitivity to initial conditions and its long-term predictability are affected by the presence of variability in the Hamiltonian function. By conducting these investigations, we aim to gain a comprehensive understanding of the disordered FPUT-α system with variability. This is expected to contribute to the broader understanding of the effects of disorder and variability on the behaviour of dynamical systems in general.

4.1 Variability in the FPUT-α Hamiltonian

The impact of disorder in the one-dimensional lattices system has been studied in [63, 64]. In [63], the complex interplay between disorder and nonlinearity that determines the heat conductivity of acoustic chains has been investigated. The authors considered the FPUT-β chain of equal masses with disordered in the harmonic spring constants and additional quartic anharmonicities in the spring potential. They demonstrated that anharmonic disordered systems provide a superior approach for investigating the processes of anomalous conductivity, while also serving as more realistic models for experimental configurations. In [64], the authors investigate how heat, in the form of waves, flows across disordered chains. Unlike ideal chains, which allow heat to move freely, disorder can trap waves, resulting in Anderson localisation [54] and no heat movement. Interestingly, when the waves become nonlinear (interact in a specific way), the situation shifts. Their calculations reveal that even with disorder, heat conduction is recovered, but the amount of heat flow is substantially dependent on the temperature of the chain. Heat flow increases rapidly at low temperatures, but grows more slowly at higher degrees. This phenomenon is related to the chaotic structure of nonlinear waves, implying a complicated interaction between disorder and nonlinearity in affecting heat transport.

Anderson localisation [54] is the occurrence of wave localisation in disordered systems. In a highly organised crystalline arrangement, waves, such as those linked to electrons in a solid, can propagate unhindered with minimal scattering. Nevertheless, the introduction of disorder into the system, such as contaminants or faults, might cause the waves to undergo localisation, resulting in their confinement to certain regions rather than their uniform distribution across the material. Anderson localisation arises when the level of disorder is sufficiently high to impede the propagation of waves across extended distances. Consequently, the waves become restricted to specific areas, resulting in a limited ability to transfer particles or energy across the material.

In Chapter 3, we studied the system with variability where the equation of motion are given by Eq. (3.1). Although it recovers the FPUT-α Hamiltonian system in the absence of variability, the system with variability given by Eq. (3.1) is not a Hamiltonian system. In this chapter, we consider the FPUT-α Hamiltonian system with variability whose Hamiltonian function is

$$H(x,p) = \frac{1}{2}\sum_{j=0}^{N}\frac{p_j^2}{t_j} + \sum_{j=0}^{N}\frac{1}{2}\left(t_{j+1}x_{j+1} - t_j x_j\right)^2 + \frac{\alpha}{3}\left(t_{j+1}x_{j+1} - t_j x_j\right)^3 = E \tag{4.1}$$

with fixed boundary conditions $x_0 = x_{N+1} = 0$ and $p_0 = 0$. Here, the variabilities t_j are picked at random from a Gaussian distribution in the following way: for a tolerance $\tau\%$, the values of t_j were drawn from a Gaussian distribution with mean 1 and standard deviation $\sigma = 1/3 \times 0.01\tau$. As a result, the values of t_j fall in the range $[1-0.01\tau, 1+0.01\tau]$. The equations of motion follow as

$$\begin{aligned}
\dot{x}_j &= \frac{p_j}{t_j} \\
\dot{p}_j &= t_j\Big(t_{j-1}x_{j-1} - 2t_jx_j + t_{j+1}x_{j+1}\Big) \\
&\quad + \alpha t_j\Big((t_{j+1}x_{j+1} - t_jx_j)^2 - (t_jx_j - t_{j-1}x_{j-1})^2\Big)
\end{aligned}$$

or, combining both in one, as

$$\begin{aligned}
\ddot{x}_j =& t_{j-1}x_{j-1} - 2t_jx_j + t_{j+1}x_{j+1} \\
&+ \alpha\Big((t_{j+1}x_{j+1} - t_jx_j)^2 - (t_jx_j - t_{j-1}x_{j-1})^2\Big).
\end{aligned} \tag{4.2}$$

These can be written in matrix form as

$$\ddot{\mathbf{x}} = S\mathbf{x} + \alpha\mathbf{F}(\mathbf{x}), \tag{4.3}$$

where

$$\ddot{\mathbf{x}} = \begin{bmatrix} \ddot{x}_1 \\ \ddot{x}_2 \\ \ddot{x}_3 \\ \vdots \\ \ddot{x}_N \end{bmatrix}, \ \mathbf{x} = \begin{bmatrix} x_1 \\ x_2 \\ x_3 \\ \vdots \\ x_N \end{bmatrix}, \ S = \begin{bmatrix} -2t_1 & t_2 & 0 & & \dots & 0 \\ t_1 & -2t_2 & t_3 & & & 0 \\ \vdots & & & \ddots & & \vdots \\ 0 & & \dots & t_{N-2} & -2t_{N-1} & t_N \\ 0 & & & 0 & t_{N-1} & -2t_N \end{bmatrix},$$

and $\mathbf{F}$ is some nonlinear vector function. Let

$$V = [v_1 \ v_2 \ \cdots \ v_N] \tag{4.4}$$

denote a matrix where its columns are the eigenvectors of S with $||v_i|| = 1$, $i = 1,\dots,N$ and the corresponding eigenvalues $\lambda_1,\lambda_2,\cdots,\lambda_N$. For convenience, let

$$\lambda_k = -\hat{\omega}_k^2,\ k = 1,\dots,N. \tag{4.5}$$

Note that $t_j = 1$ for all j in the FPUT-α system without variability, so S becomes a tridiagonal matrix. In this case, V is similar to A and $\lambda_k = -\omega_k^2, k = 1,\dots,N$, given in Eq. (2.43)[20].

Introducing the (linear) normal-modes transformation

$$\mathbf{x} = M\mathbf{Q}, \tag{4.6a}$$

$$\mathbf{p}' = M\mathbf{P}, \tag{4.6b}$$

where $p'_j = p_j/t_j$, $M = kV$, and $k = c\hat{\omega}_1/\sqrt{2E}$ for some constant $c \in \mathbb{R}$, the equation of motion (4.3) becomes

$$\ddot{\mathbf{Q}} = D\mathbf{Q} + \alpha M^{-1}\hat{\mathbf{F}}(\mathbf{Q}), \tag{4.7}$$

where D is a diagonal matrix with the diagonal entries given by the eigenvalues of S and $\hat{\mathbf{F}}$ is a nonlinear vector function. Similarly to the approach in Chapter 3, the energy of normal mode k is defined as

$$E_k = \frac{1}{2}\left(P_k^2 + \hat{\omega}_k^2 Q_k^2\right), \tag{4.8}$$

where $\hat{\omega}_k$ is given by Eq. (4.5).

Next, we investigate the influence of variability on the evolution of the normal-mode energy (4.8) at a fixed energy level. In the same spirit as the original FPUT-α experiment, we choose initial conditions in the physical space such that only the lowest normal-mode is excited. The initial energy employed in our computations is equal to the initial energy of the original FPUT-α system in Eq. (2.38) under the initial conditions (2.45) for each number of particle N. Then, the initial conditions of Eq. (4.2) are chosen by finding a constant $c \in \mathbb{R}$ such that

$$\mathbf{x}(0) = cv_1, \quad \mathbf{p}(0) = 0, \tag{4.9}$$

satisfy Eq. (4.1) for a fixed energy E. In this context, v_1 refers to the first column of matrix V defined in Eq. (4.4). We note that in the normal-mode space, the initial conditions read as

$$Q_1(0) = \frac{\sqrt{2E}}{\hat{\omega}_1}, \quad Q_k(0) = 0, k = 2, \ldots, N, \quad P_j(0) = 0,\ j = 1, \ldots, N. \tag{4.10}$$

The time evolution of the solutions to system (4.2) with initial conditions (4.9) and its associated normal mode energy E_k of the first four modes for $N = 32$ particles and three different percentages of tolerance, namely $\tau = 5\%, \tau = 50\%$ and $\tau = 95\%$, are shown in Fig. 4.1. The initial energy of the system is $E = 0.07471$, which is similar to the initial energy in Fig. 2.5. Comparing panel (b) in Fig. 2.5 with panels (b), (d), (f) in Figs. 4.1, we can see that the recurrence is weakening due to the effect of variability, as evidenced by the declining peak of the mode energy E_1. Then as the variability increases, it becomes more difficult to transmit energy from the lowest to the higher modes, resulting in the localisation of energy, shown

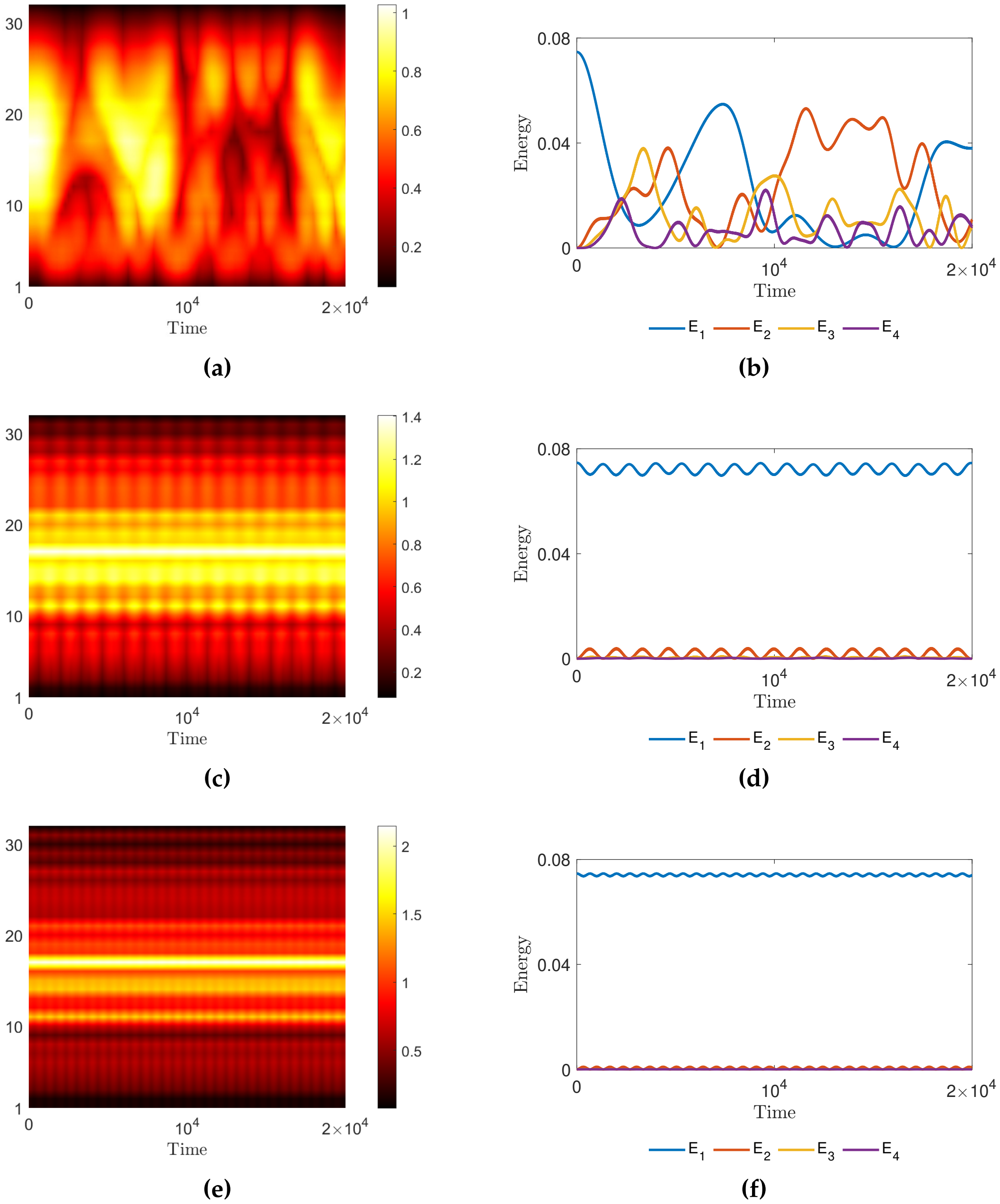

(a) **(b)**

(c) **(d)**

(e) **(f)**

Figure 4.1. Dynamics of $x_j(t)$ with its corresponding normal-mode energy in time for the system in Eq. (4.2) using the initial condition in Eq. (4.9) for $N = 32$. Panels (a) and (b) are for $\tau = 5\%$ tolerance, panels (c) and (d) for $\tau = 50\%$ and panels (e) and (f) for $\tau = 95\%$. The colour bars in panels (a), (c), (e) denote the peak of the oscillation envelope of $x_j(t)$ in time. Note that the ranges in the vertical axes in panels (a), (c), (e) are from 1 to $N = 32$.

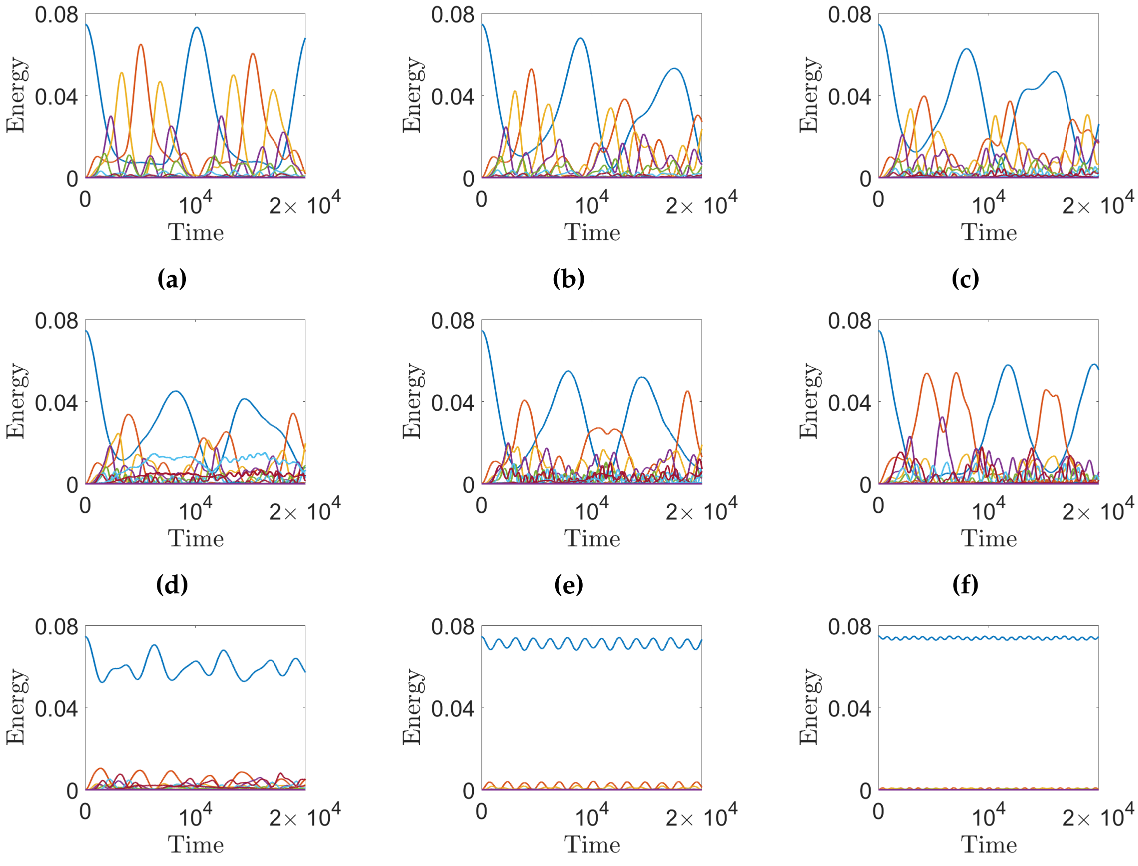

(a) (b) (c) (d) (e) (f) (g) (h) (i)

Figure 4.2. The harmonic energy for $N = 32$ with (a) 0% (b) 10% (c) 20% (d) 30% (e) 40% (f) 50% (g) 60% (h) 70% (i) 80% tolerance.

in panels (d) and (f) in Fig. 4.1. We also provide the evolution of normal mode energy for $N = 32$ and $N = 64$ with several difference tolerances in Figs. 4.2-4.3. Moreover, the corresponding eigenvectors and eigenvalues from Eqs. (4.4)-(4.5) are shown in Figs. 4.4-4.5.

In the next section, we will explain why the energy exchange across modes decreases as the percentage of variability grows. As a result, energy localisation takes place in the energy-mode space. The plots of normal-mode energies show that in the event of energy localisation, the majority of the mode coordinates vanish in time. Thus, rather than working in the real (physical) space, it will give a great advantage if we work in the normal-mode coordinate system given in Eq.

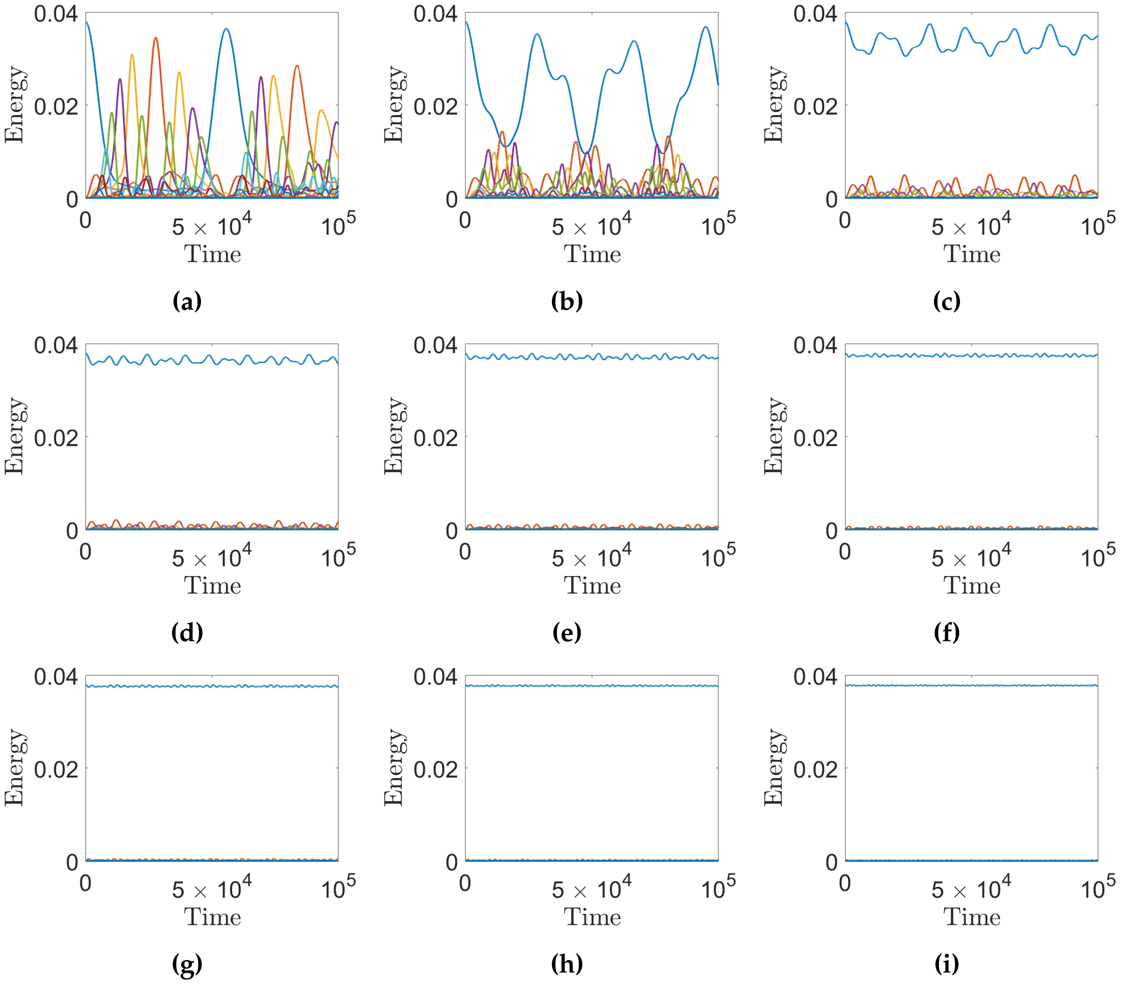

(a) **(b)** **(c)**

(d) **(e)** **(f)**

(g) **(h)** **(i)**

Figure 4.3. The harmonic energy for $N = 64$ with (a) 0% (b) 10% (c) 20% (d) 30% (e) 40% (f) 50% (g) 60% (h) 70% (i) 80% tolerance.

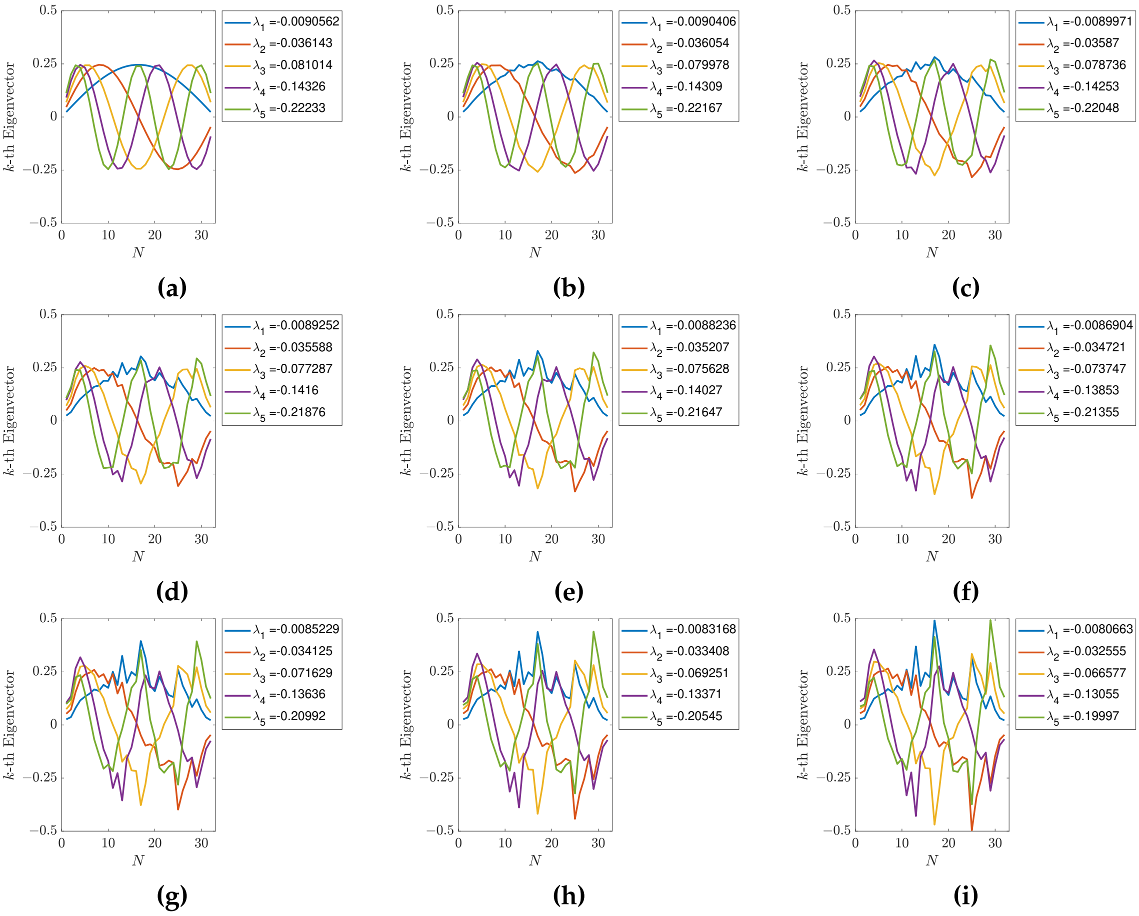

Figure 4.4. The eigenvectors and the corresponding eigenvalues of Fig. 4.2 for $N = 32$ with (a) 0% (b) 10% (c) 20% (d) 30% (e) 40% (f) 50% (g) 60% (h) 70% (i) 80% tolerance

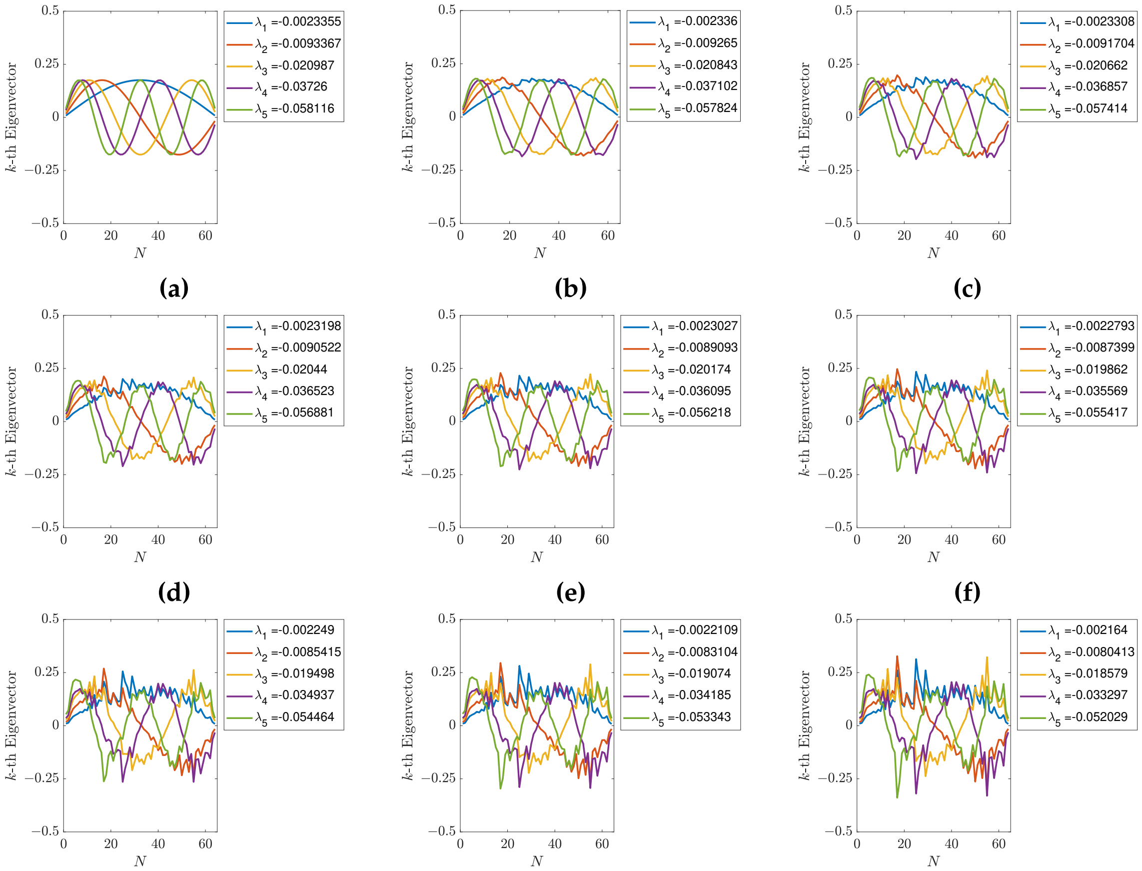

(a) **(b)** **(c)**

(d) **(e)** **(f)**

(g) **(h)** **(i)**

Figure 4.5. The eigenvectors and the corresponding eigenvalues of Fig. 4.3 for $N = 64$ with (a) 0% (b) 10% (c) 20% (d) 30% (e) 40% (f) 50% (g) 60% (h) 70% (i) 80% tolerance

(4.7), as we can approximate system (4.7) by taking only the first few modes into account. We present in Fig. 4.6 the normal-mode energy from the approximation of Eq. (4.7) using only 2, 4, and 8 normal modes, while all other modes are fixed at 0, and different percentages of variability to demonstrate numerically that this approximation can be justified.

In terms of recurrence period, we can observe in Fig. 4.6 that using 4 and 8 modes produces dynamics that are nearly identical to those seen in Fig. 2.5 in the absence of variability. We can detect energy recurrence and localisation even with 2 modes as the percentage of variability grows. We can see from panels (d) and (f) in Fig. 4.1 and panels (g) and (j) in Fig. 4.6 that a two normal-mode system yields an adequate approximation to Eq. (4.7). Therefore, we will look at these two normal-mode approximations in the following section.

4.2 Two normal-mode system

The majority of high-order modes are negligible when energy localisation takes place as illustrated in Fig. 4.1. Therefore, similar to Sec. 3.2, we set all high-order normal-modes to zero, except the first two, in order to obtain a two normal-mode system. In particular, we set $Q_k(t) = 0$ for $k = 3,4,\dots,N$ in Eq. (4.7). This gives us the following system

$$\ddot{Q}_1 = -\hat{\omega}_1^2 Q_1 + \epsilon\Big(A_1 Q_1^2 + A_2 Q_2^2 + A_3 Q_1 Q_2\Big), \tag{4.11a}$$

$$\ddot{Q}_2 = -\hat{\omega}_2^2 Q_2 + \epsilon\Big(B_1 Q_1^2 + B_2 Q_2^2 + B_3 Q_1 Q_2\Big), \tag{4.11b}$$

where A_i, $B_i \in \mathbb{R}$, $i = 1,2,3$ and $\hat{\omega}_k$ is given in Eq. (4.5).

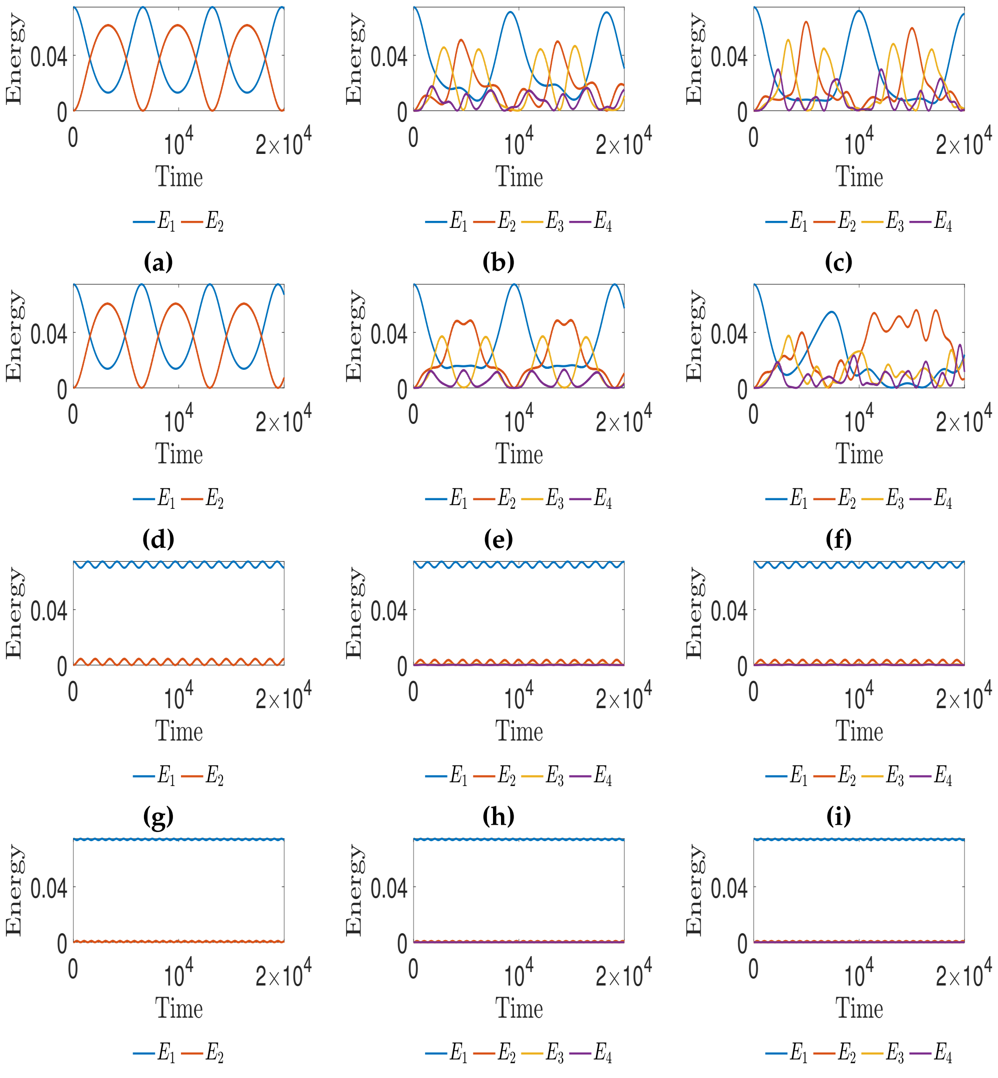

(a) (b) (c) (d) (e) (f) (g) (h) (i) (j) (k) (l)

Figure 4.6. The evolution of normal-mode energy as obtained from integrating Equation (4.7) using different numbers of normal modes. In panels (a), (d), (g), and (j), only two normal modes are used, in panels (b), (e), (h), and (k), four modes are used, and in panels (c), (f), (i), and (l), eight modes are used. Each row represents different tolerance, i.e. 0% ((a)-(c)), 5% ((d)-(f)), 50% ((g)-(i)), and 95% ((j)-(l)). The first four modes, except for the two modes system, are plotted in all panels, but they are only activated for 0% and 5% tolerance in panels (a) and (f). For 95% tolerance, all modes except the first are essentially 0.

In [65, 66], the authors studied the localisation property of FPUT lattices in normal-mode space (or q-space). They found that time-periodic states can be exponentially localised in q-space. These time-periodic solutions, called q-breathers, are obtained by continuing the simple harmonic motion exhibited by the q-th normal-mode in the uncoupled case. For small values of the coupling parameters or the initial energy, the distribution of energy in q-space remains localised in only a few modes. Therefore, the variability in FPUT lattices leads to q-breathers because the energy remains localised in q-space.

Furthermore, the authors in [59, 67] expand the idea of q-breathers by considering classes of special solutions lying on tori of any low dimension s, that is solutions with s independent frequencies, representing the continuation of motions resulting from exciting s modes of the uncoupled case. Such tori are referred to as q-tori. For $N = 32$, it has been reported in [67] that the original FPUT system lies on a 5-dimensional torus.

The Poincaré-Lindstedt method has been employed to derive such solutions on q-tori. According to this approach, the incommensurable frequencies, indicative of the q-tori's dimension, are considered as minor corrections to the normal mode frequencies, as outlined in [59]. These corrected frequencies are subsequently validated through numerical verification using the GALI method [68]. In this context, we can interpret our two-normal-mode system in Eq. (4.11) as a two-frequency solution that lies on a two-dimensional torus.

In the following, we employ the multiple-time scale expansion approach to provide approximations for the solutions of Eq. (4.11). This approach serves as a tool to explain the energy localisation mechanism as we increase the percentage of variability.

4.2.1 Multiple-time scale approximation

We consider the following asymptotic series

$$Q_1 = X_0(t,T) + \epsilon X_1(t,T) + \ldots, \tag{4.12a}$$

$$Q_2 = Y_0(t,T) + \epsilon Y_1(t,T) + \ldots, \tag{4.12b}$$

where $\hat{\omega}_2 = 2\hat{\omega}_1 + \epsilon$, $|\epsilon| \ll 1$, and $T = \epsilon t$ is a slow-time variable to approximate the solutions of Eq. (4.11). Following similar procedures as in Sec. 3.2.1, the leading-order approximation to Eqs. (4.12) are given by

$$X_0 = q_1(T)e^{i\hat{\omega}_1 t} + q_1^*(T)e^{-i\hat{\omega}_1 t}, \quad Y_0 = q_2(T)e^{i\hat{\omega}_2 t} + q_2^*(T)e^{-i\hat{\omega}_2 t}, \tag{4.13}$$

where $q_1(T)$ and $q_2(T)$ satisfy the following system of ordinary differential equations:

$$i\frac{dq_1(T)}{dT} = q_1(T) + \widetilde{A}q_1^*q_2, \tag{4.14a}$$

$$i\frac{dq_2(T)}{dT} = q_2(T) + \widetilde{B}q_1^2, \tag{4.14b}$$

Here, $\tilde{A} = A_3/(2\hat{\omega}_1)$ and $\tilde{B} = B_1/(2\hat{\omega}_2)$. Recalling Eqs. (4.10), the initial conditions of system (4.14) are

$$q_1(0) = \frac{Q_1(0)}{2},\ q_2(0) = 0. \tag{4.15}$$

Our numerical computations show that both $\tilde{A}$ and $\tilde{B}$ in Eq. (4.14), which are a function of τ, are either positive or negative for fixed τ. However, Eq. (4.14) is invariant when $\tilde{A}$ and $\tilde{B}$ have the same sign, as we can use the transformation $\hat{q}_2 = -q_2$. Therefore, we plot these parameters when both $\tilde{A}$ and $\tilde{B}$ are positive only as a function of τ for $N = 32$ particles and 100 realisations in Fig. 4.7. These realisations have been computed by fixing τ and opting for 100 sets of $N = 32$ randomly generated numbers from the Gaussian distribution with mean 1 and standard deviation $\sigma = 1/3 \times 0.01\tau$. Thus, the t_js in the 100 sets lie in the interval $[1 - 0.01\tau, 1 + 0.01\tau]$.

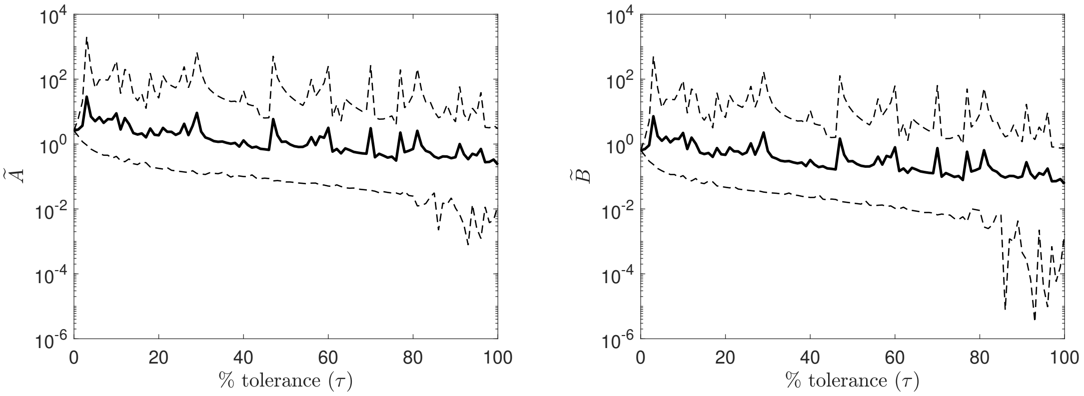

(a) **(b)**

Figure 4.7. The parameter values $\tilde{A}$ and $\tilde{B}$ as a function of τ obtained numerically for $N = 32$. The solid black curve is the parameter mean over 100 sets of variability at the same percentage, and the upper and lower black dashed curves are their maximum and minimum values, respectively. Note the logarithmic axis on the vertical axis and both $\tilde{A}$ and $\tilde{B}$ are always positive (see discussion in the text).

We compare the dynamics of the normal modes Q_1 and Q_2 of Eq. (4.11) and its slow-time variable approximations q_1 and q_2 of Eqs. (4.14) in Fig. 4.8, where it can be shown that q_j is an envelope of Q_j for $j = 1, 2$.

Next we describe the mechanism of energy localisation when the percentage of variability τ increases. It is worth noting that as $q_2(0) = 0$, the energy transmission from $q_1(t)$ to $q_2(t)$ is made possible due to the nonlinear coupling coefficient $\tilde{B}$.

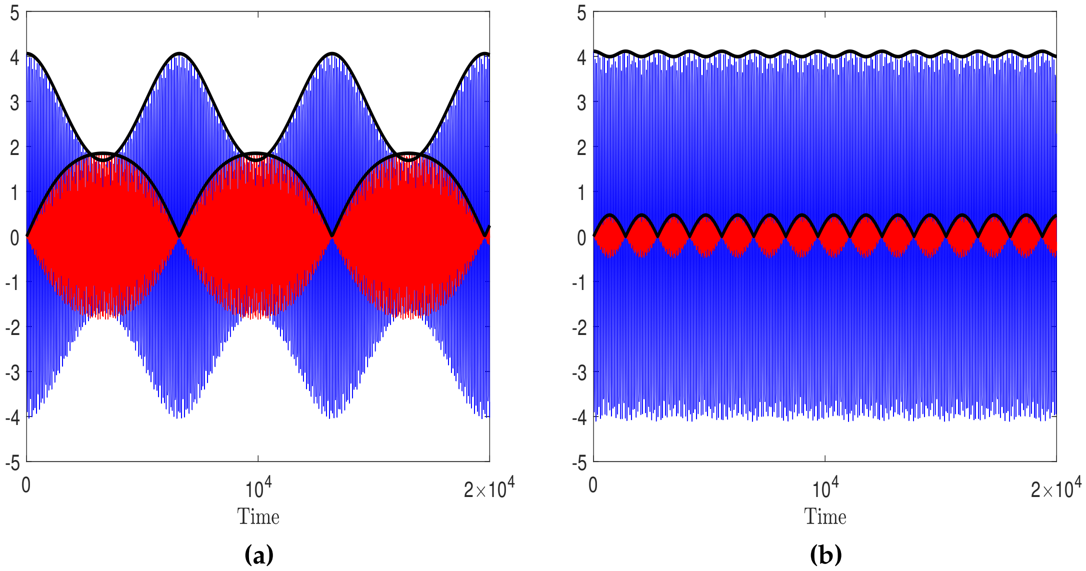

Figure 4.8. Evolution of the normal-mode variables Q_1 (blue curve) and Q_2 (red curve) in time with their envelopes q_1 and q_2 (black curves) from Eqs. (4.14) for $\tau = 0\%$ in panel (a) and $\tau = 50\%$ in panel (b).

Therefore, we will analyse the role of $\tilde{B}$ in the localisation of energy as we increase τ.

4.2.2 Equilibrium solutions

Since Eq. (4.14) is identical to Eqs. (3.19)-(3.20), we follow the same method as in Section 3.2.2 to analyse the equilibrium solutions. The bifurcation diagram is once more illustrated in Figs. 3.7 or 4.9, while the equilibrium points Δ_j, $j = 1,2$ are plotted in Fig. 4.10. Similar to Fig. 3.8, we represent in Fig. 4.10 (b) $\tanh(\Delta_2/100)$ in place of Δ_2 to effectively demonstrate the behaviour of Δ_2 as it approaches infinity when either $\widetilde{A}$ or $\widetilde{B}$ approach zero.

According to Fig. 4.7, we have obtained numerically the parameter values for Eq. (4.14) and have found that they are either both positive or negative. Therefore, this equation can only occupy the first and third quadrants in Fig. 4.9. If both paramater values are positive (negative), then for a small percentage of variability

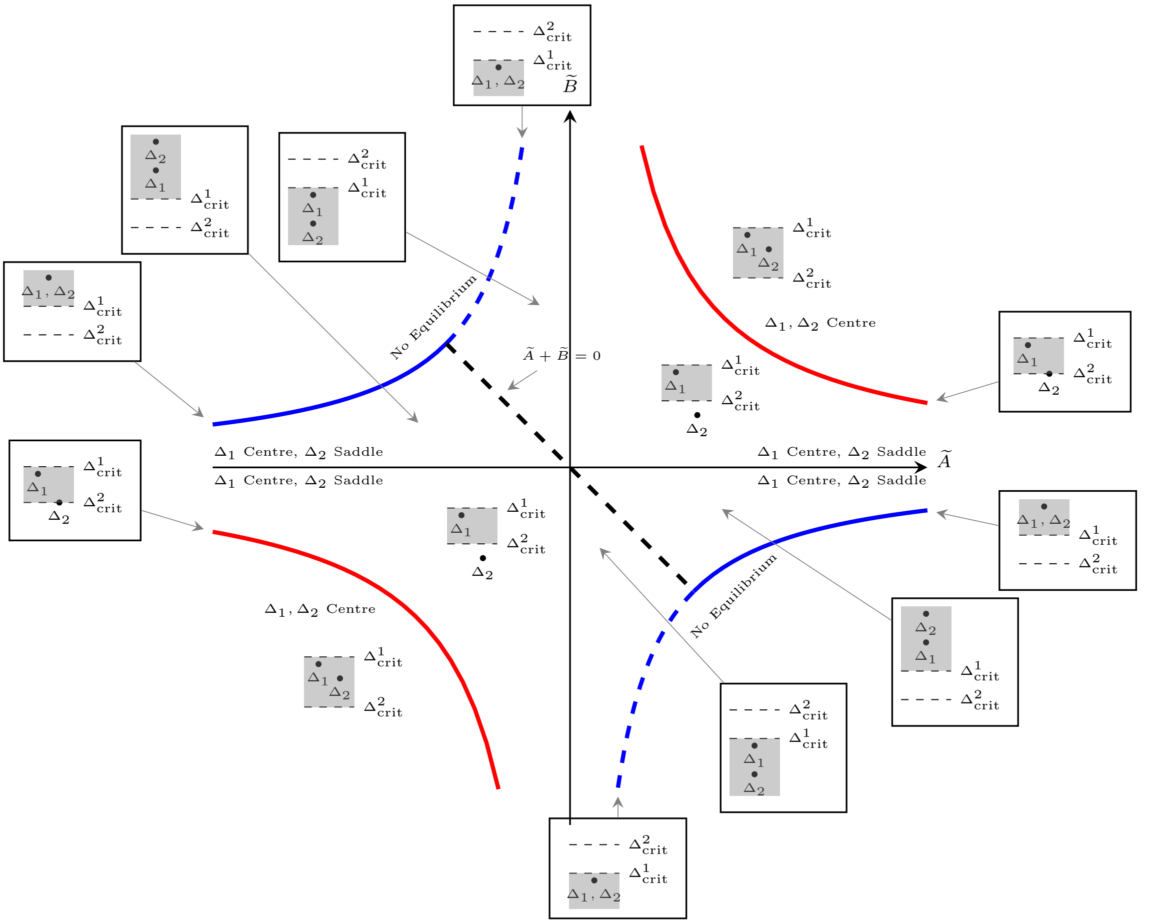

Figure 4.9. Bifurcation diagram of the equilibrium points Δ_1 and Δ_2 in the $(\widetilde{A},\widetilde{B})$-space. The well-defined region for system (4.14) is shown as the shaded area (see text for more details).

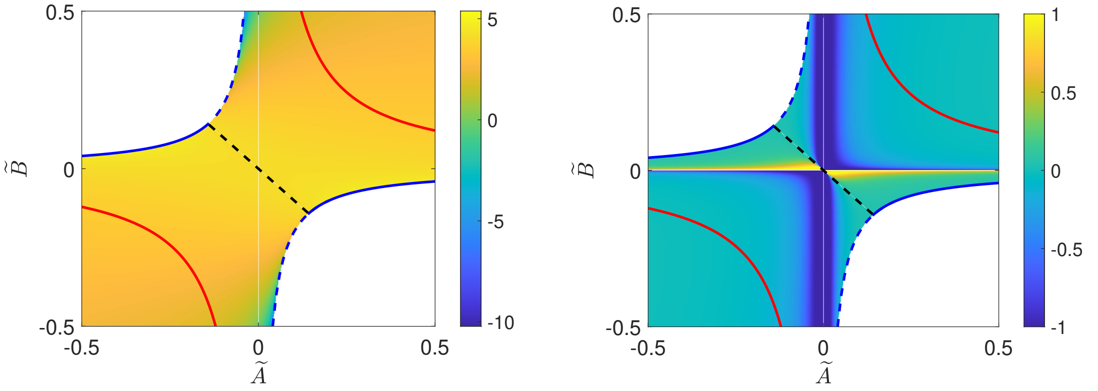

(a) **(b)**

Figure 4.10. The colour plot of Δ_1 (in panel (a)) and $\tanh(\Delta_2/100)$ (in panel (b)) as a function of $\widetilde{A}$ and $\widetilde{B}$. Note that the red, black dashed, and blue curves are the same curves with those in Fig. 4.9.

both of them will be located above (below) the red curve in Fig. 4.9. In this case, Eq. (4.14) will have two equilibrium points where both of them are centres, hence stable. Upon increasing the percentage of variability further, both parameter values are decreasing and at some percentage, they cross the red curve. In this case, Eq. (4.14) will only have one stable equilibrium point, which is a centre. The phase space for these two different cases are shown in Fig. 4.11. For $\tau = 0\%$ or in the absence of variability, the parameter values are $\widetilde{A} = 2.58$ and $\widetilde{B} = 0.65$. The two stable equilibrium points are $(\theta_1, \Delta_1) = (0, 2.74)$ and $(\theta_2, \Delta_2) = (\pi/2, 1.98)$, which are shown in Fig. 4.11a. For $\tau = 50\%$, the parameter values are $\widetilde{A} = 0.13$ and $\widetilde{B} = 0.03$. The stable equilibrium point is $(\theta_1, \Delta_1) = (0, 4.16)$, which is shown in Fig. 4.11b. We can also determine the boundary of the well-defined region as

$$\lim_{\widetilde{B}\to 0} \Delta^1_{\text{crit}} = r_1^2, \quad \lim_{\widetilde{B}\to 0} \Delta^2_{\text{crit}} = 0, \tag{4.16}$$

where we have used the initial conditions (4.15) in the computations of the two limits. Equation (4.16) implies that Δ in the well-defined region is positive definite as $\widetilde{B} \to 0$. Recalling Eq. (3.23b), we conclude that $\Delta > 0$ corresponds to energy localisation as the magnitude of q_1 is always greater than q_2.

4.3 Chaotic indicators

The FPUT-α system can be viewed as as a truncation of the regular, integrable Toda system [69]. As a result, the non-integrable FPUT-α system acts similarly to the integrable Toda system for a period of time before exhibiting the expected non-integrable system behaviour [70]. The length of this period, also known as

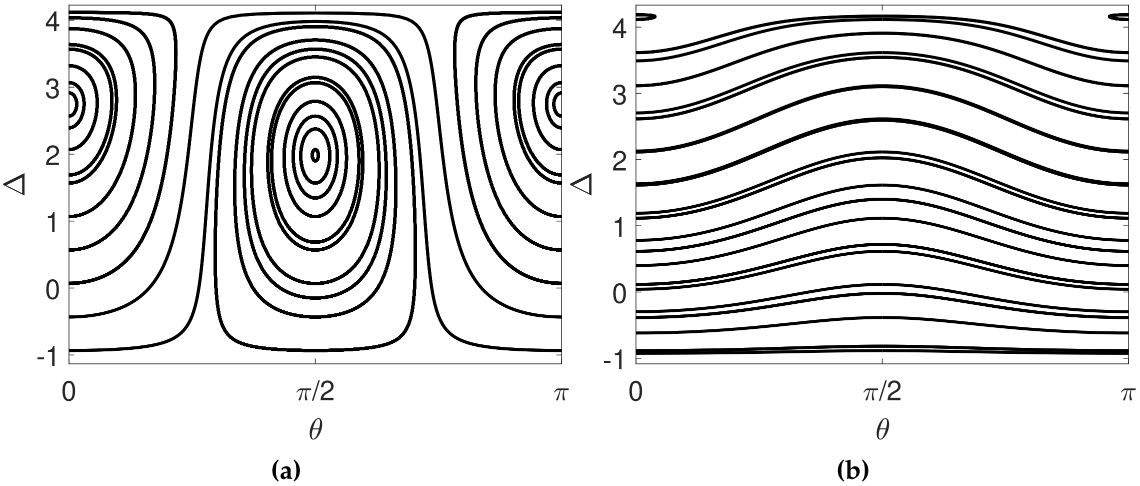

(a) **(b)**

Figure 4.11. Phase portraits of the (Δ, θ) system given by Eqs. (3.29b), (3.29c) for $\tau = 0\%$ in panel (a) and $\tau = 50\%$ in panel (b).

the lifetime of the metastable state, depends on the energy E and the number of particles N [12]. For a small initial energy, the FPUT-α system persists in the metastable state for a long time, causing energy thermalisation to be difficult to observe.

It has been shown in [12] that the lifetime of the metastable state t_m follows the scaling law $t_m = 0.023 \times (E\alpha^2)^{-4.9}$. Therefore, we expect to observe the regular dynamics of the FPUT-α system (2.38) for $t \leq t_m$. At the same energy level, we also study the system (4.1) and see how variability affects the chaotic properties of this system. Particularly, we look at lattices of $N = 4, 8, 16, 32$ particles in systems (4.1) and utilise the mLE [32] and SALI [34, 35] to distinguish between regular and chaotic dynamics. We employ Algorithm 2 to calculate the mLE and Algorithm 3 to compute SALI.

For each number of particles N, the initial conditions are given in Eq. (4.9), where the initial energy is similar to that in the case without variability which has been studied in Chapter (3.3). We compute the mLE and SALI for 40 realisations of variability for $\tau = 5\%$, 50%, and 95%. The corresponding plots are shown in Figs. 4.12 and 4.13.

For $N = 4$, all trajectories with $\tau = 5\%$, 50%, and 95% in panels (a)-(c) of Figs. 4.12 seem to be regular up to the final integration time $t = 10^8$, which is shown by the mLEs' tendency to converge to zero following the $1/t$ law. We observe similar behaviour for $N = 8$ and a tolerance level of $\tau = 5\%$. However, when the tolerance level increases to 50% and 95%, we observe three and four chaotic trajectories, respectively. This is evident from the tendency of the mLE to converge to positive values for these trajectories, as shown in Figs. 4.12(d)-(f). Additionally, SALI exhibits a sudden decrease to very small values, further indicating the chaotic behaviour of these trajectories, as depicted in Figs. 4.13(a)-(c).

The number of chaotic trajectories increases significantly for $N = 16$ and 32. The percentage of chaotic trajectories (out of 40 realisations) as a function of N is illustrated in Fig. 4.14, where the increase is evident for $\tau = 5\%$ and 50%. Nevertheless, when $\tau = 95\%$, the proportion of chaotic trajectories only increases for $N = 4, 8, 16$, and then decreases for $N = 32$. These results imply that a small percentage of tolerance has less effect on chaotic behaviour than a bigger percentage for small N, and this trend is reversed as N increases.

Now we want to study how energy localisation relates to the chaotic character of its trajectory. In the absence of variability, the appearance of super recurrence when we integrate Eq. (2.39) for a long time has been reported in [10, 11, 71, 72]. Therefore, the energy recurrence is an attribute of a regular trajectory according to Fig. 3.11. In the case with variability, system (4.1) contains chaotic and regular trajectories, which depend on N and τ. We find that either energy recurrence or

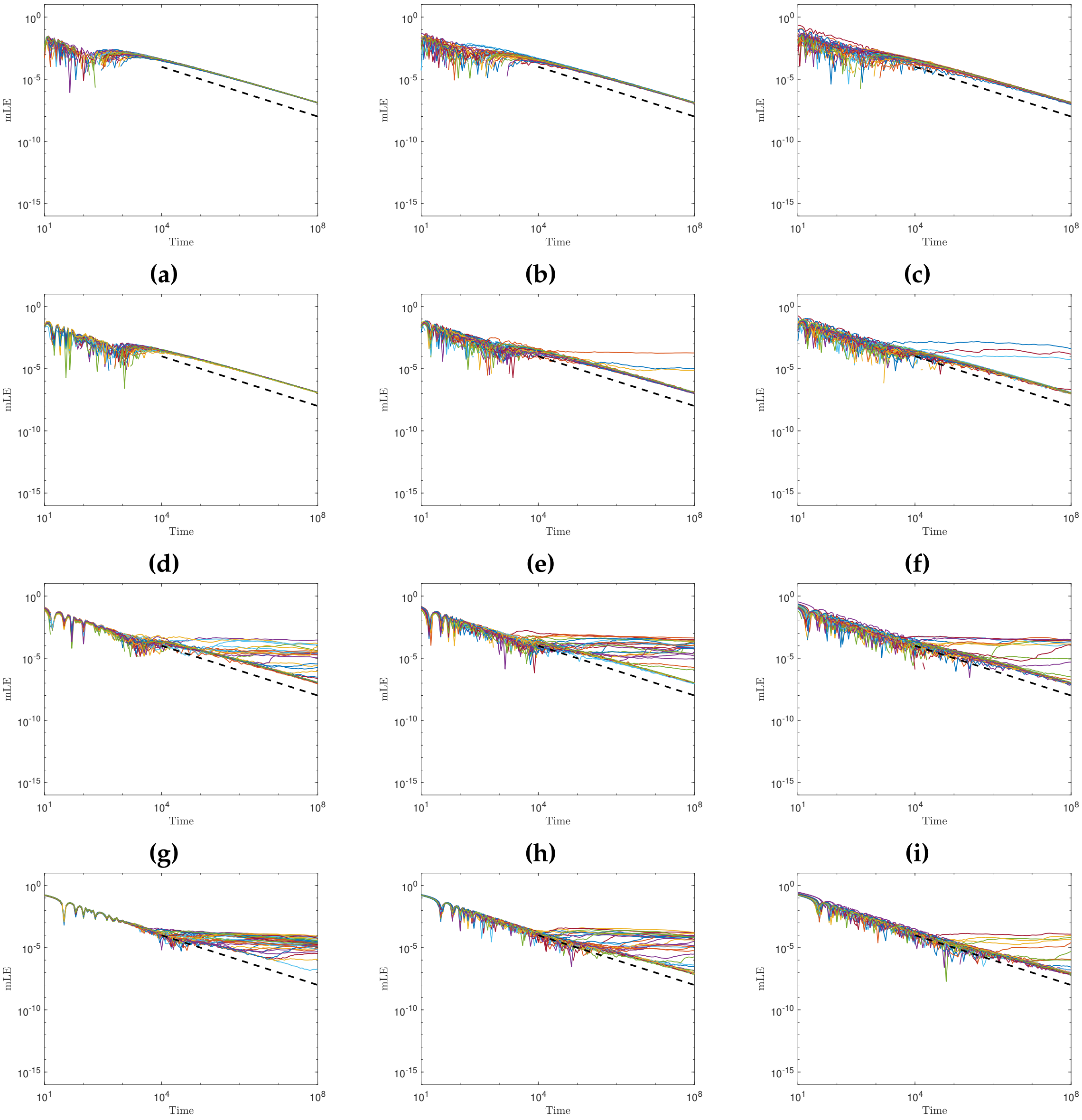

(a) **(b)** **(c)**

(d) **(e)** **(f)**

(g) **(h)** **(i)**

(j) **(k)** **(l)**

Figure 4.12. Plot of the maximum Lyapunov exponent for 40 trajectories with $N = 4$ in panels (a)-(c), $N = 8$ in panels (d)-(f), $N = 16$ in panels (g)-(i), and $N = 32$ in panels (j)-(l). The tolerance is 5% in panels (a), (d), (g), (j), 50% in panels (b), (e), (h), (k), and 95% in panels (c), (f), (i), (l).

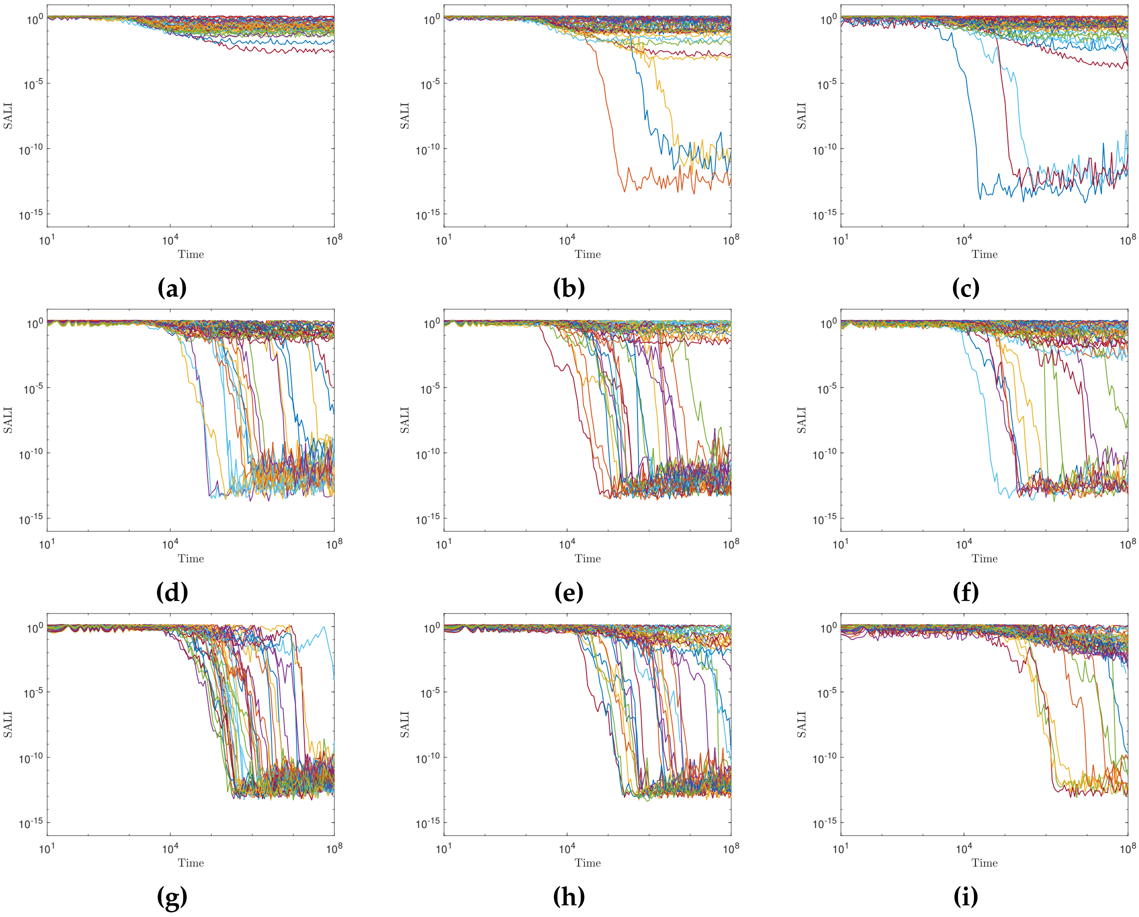

(a) **(b)** **(c)**

(d) **(e)** **(f)**

(g) **(h)** **(i)**

Figure 4.13. Plot of the SALI for 40 trajectories with $N = 8$ in panels (a)-(c), $N = 16$ in panels (d)-(f), $N = 32$ in panels (g)-(i). The tolerance is 5% in panels (a), (d), (g), 50% in panels (b), (e), (h), and 95% in panels (c), (f), (i).

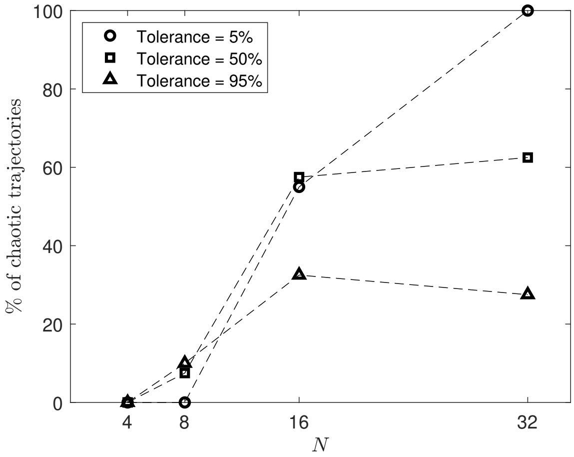

Figure 4.14. Percentage of chaotic trajectories as a function of N for 40 realisations of variability with 5%,50%, and 95% tolerance. The black-dash line segments connect the black points and are there to guide the eye.

energy localisation takes place when the trajectory is regular. In contrast, chaotic trajectory corresponds to the thermalisation of energy. In Fig. 4.15, we illustrate a particular instance of mLE and its corresponding normal mode energy for $N = 16$ and $\tau = 5\%$, $50\%, 95\%$ resulting from regular and chaotic trajectories. We use a similar initial energy as in Fig. 3.10, i.e. $E = 0.1447$.

The super recurrence can be seen in panel (b) in Fig. 4.15 with period of about 7×10^7, while panel (d) shows the localisation of energy in the first few normal modes. This localisation is getting stronger (no energy is transferred to other normal modes) if we consider the regular trajectory with higher percentage of tolerance τ. Furthermore, the thermalisation of energy as a consequence of chaotic trajectories is shown in panel (f) in Fig. 4.15, where the energy is shared among all normal modes.

4.4 Conclusions

In this chapter, we focused on the disordered FPUT-α system with variability at a fixed energy level. To understand the phenomenon of energy localisation as the percentage of variability increases, we have employed a two normal-mode approximation technique, which has been solved using multiple-scale expansion methods. Through this approach, we have successfully explained the underlying mechanism behind energy localisation in the system. Additionally, this two normal-mode system can be viewed as the two-frequency solution on q-tori because it has two incommensurable frequencies.

Furthermore, we have investigated the influence of variability on the chaotic behaviour of the system by calculating the maximum Lyapunov exponent and

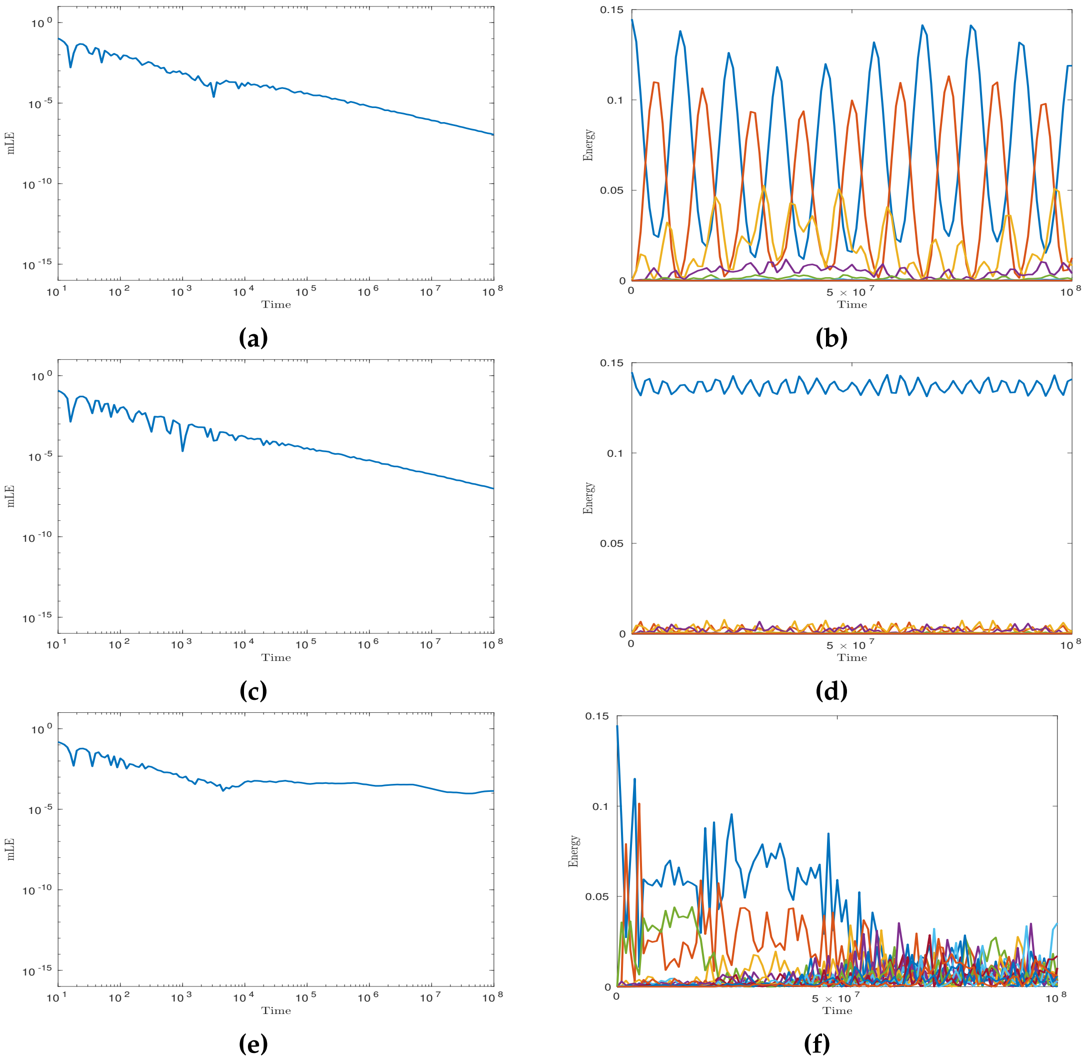

(a) **(b)**

(c) **(d)**

(e) **(f)**

Figure 4.15. The maximum Lyapunov exponent (mLE) and its corresponding normal mode energy for $N = 16$ and tolerance $\tau = 5\%$ in panels (a)-(b), $\tau = 50\%$ in panels (c)-(d), and $\tau = 95\%$ in panels (e)-(f). We plot all normal mode energy E_k, $k = 1, \ldots, 16$ in panels (b), (d), (f).

the Smaller Alignment Index for many realisations at the same percentage of variability. Our findings reveal interesting patterns. For tolerance levels of 5% and 50%, the likelihood of observing chaotic trajectories increases as the number of particles N is increased. However, at a tolerance level of 95%, the percentage of chaotic trajectories exhibits a growth trend for $N = 4, 8, 16$, but a slight decline for $N = 32$. This suggests a complex relationship between the number of particles, the tolerance level, and the occurrence of chaotic behaviour.

Moreover, we have explored the connection between energy localisation and the chaotic nature of the trajectories of the system. Our analysis indicates that when the trajectory exhibits regular behaviour, it can either lead to energy recurrence or energy localisation. In contrast, a chaotic trajectory tends to result in energy thermalisation, implying a more random distribution of energy among the components of the system.

Chapter 5

Analysing chaos in the standard map using q-statistics

In the previous two chapters, we have studied the chaotic behaviour of dynamical system by computing two chaotic indicators, namely maximum Lyapunov exponent and smaller alignment index (SALI). Another way to study the chaotic behaviour is by considering a probability distribution function (PDF) which can be derived from the system's trajectories. This PDF is then analysed by using q-statistics which has been subject to intense research [44, 73–76].

The statistical characterisation of dynamical systems is based on the analysis of the distribution of a statistical variable derived from their trajectories. In the case of chaotic systems, the probability distribution function (PDF) of this variable tends to a Gaussian distribution, indicating a chaotic behaviour. On the other hand, systems can also display PDFs that can be approximated by a q-Gaussian distribution, which signifies a certain level of regularity and determinism.

In the context of the standard map, previous studies [18, 43] have demonstrated that the PDF of the system depends on the initial conditions. When the initial conditions are chosen randomly from the chaotic sea in the phase space, the resulting distribution can be well fitted by a Gaussian. However, if the initial conditions are randomly selected from the stability island, the distribution converges to a q-Gaussian.

This chapter focuses on analysing the probability distribution of trajectories of the standard map for different parameter values, specifically exploring both chaotic and regular cases. Our goal is to obtain the parameters that best fit the PDFs by solving a multi-objective optimisation problem. To achieve this, we employ a genetic algorithm approach, which allows us to determine the optimal set of parameters for the q-Gaussian distribution that accurately describes the numerical data obtained from the standard map trajectories.

5.1 Dynamics of the standard map

We consider the standard map, which is defined by

$$p_{i+1} = p_i - K \sin x_i \tag{5.1a}$$

$$x_{i+1} = x_i + p_{i+1} \tag{5.1b}$$

where p_i and x_i are taken modulo 2π. This is a one parameter map with parameter K and can exhibit chaotic behaviour for a wide range of parameter values. The phase spaces of this map for four typical values of K are shown in Fig. 5.1. All black regions are the areas in the phase space that are occupied by chaotic trajectories.

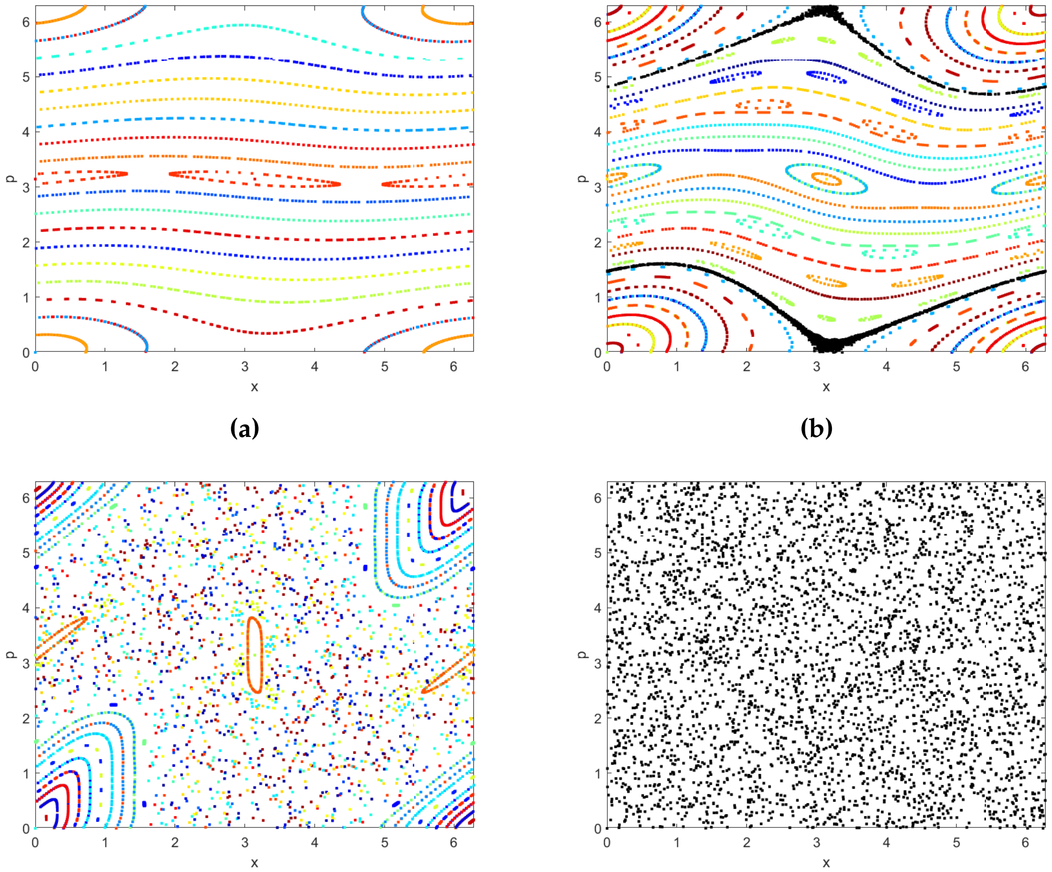

(a) **(b)** **(c)** **(d)**

Figure 5.1. Phase portraits of the standard map for (a) $K = 0.2$, (b) $K = 0.6$, (c) $K = 2$, (d) $K = 10$. As K increases, chaos prevails.

These areas are getting bigger as we increase K. Moreover, Fig. 5.2 shows the corresponding mLE when the initial conditions for Eq. (5.1) are taken from the phase space. In addition, we also plot SALI for the same initial conditions in Fig. 5.3.

Next, we study the stability of the fixed points of the standard map. The fixed points are given by

$$p_i = p_i - K \sin x_i$$

$$x_i = x_i + p_i$$

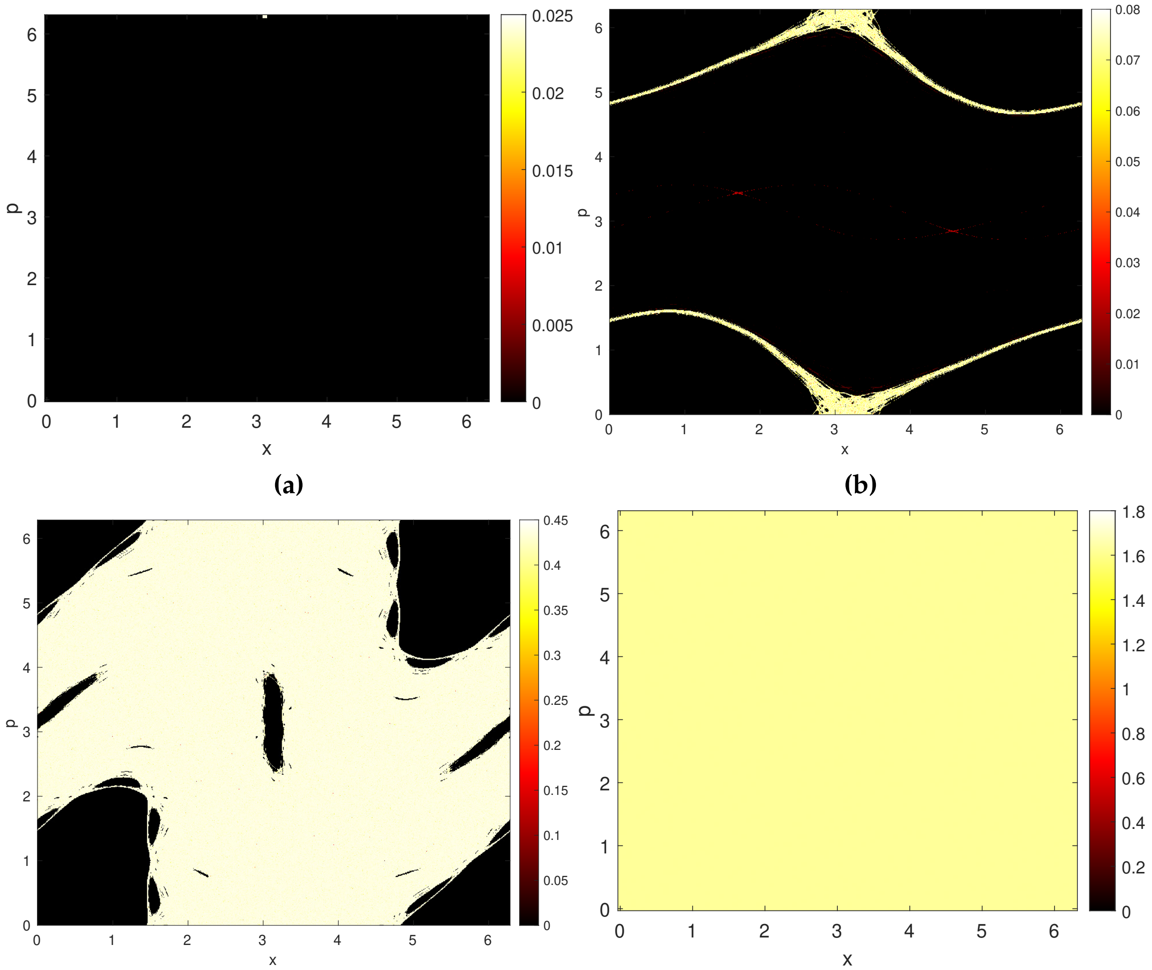

(a) **(b)**

(c) **(d)**

Figure 5.2. Maximum Lyapunov exponents of the phase portrait of the standard map for (a) $K = 0.2$, (b) $K = 0.6$, (c) $K = 2$, (d) $K = 10$. In each case, the mLEs are calculated for 10^6 initial conditions which are evenly distributed on the whole phase space and each initial condition is iterated 10^7 times. The colour bar represents the value of the mLE associated with a trajectory originating from the initial conditions (x,p).

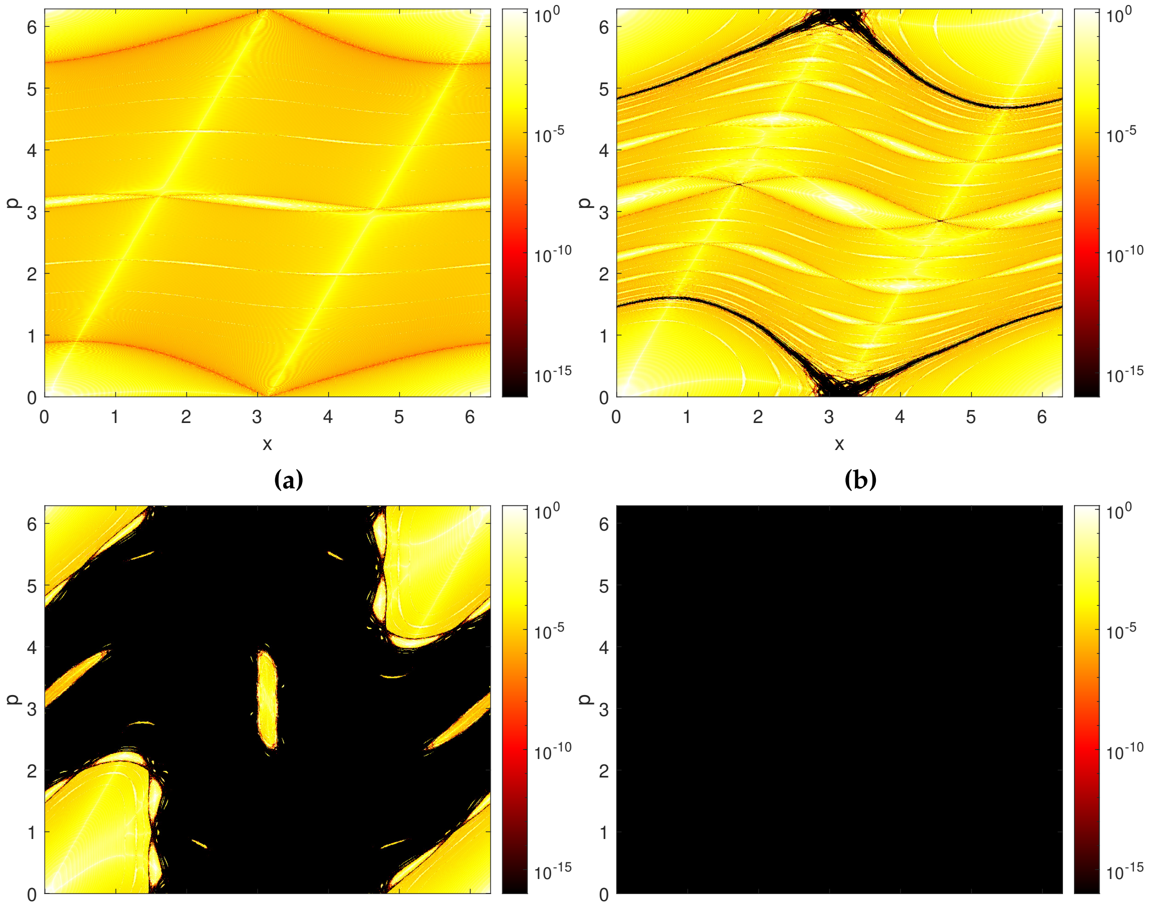

(a) **(b)**

(c) **(d)**

Figure 5.3. SALI plots of the phase portrait of the standard map for (a) $K = 0.2$, (b) $K = 0.6$, (c) $K = 2$, (d) $K = 10$. In each case, the SALIs are calculated for 10^6 initial conditions and each initial condition is iterated 500 times. The colour bar represents the value of SALI associated with a trajectory originating from the initial conditions (x, p).

which yield the set of simultaneous equations

$$\sin(x_i) = 0,$$

$$p_i = 0 \mod 2\pi.$$

Therefore, the fixed points are given by

$$x^* = n\pi, \tag{5.2}$$

$$p^* = 2m\pi, \tag{5.3}$$

where $n, m \in \mathbb{Z}$.

The Jacobian matrix of the standard map, evaluated at the fixed points (x^*, p^*) given by the Eqs. (5.2)-(5.3), is

$$J = \begin{bmatrix} \frac{\partial x_{i+1}}{\partial x_i} & \frac{\partial x_{i+1}}{\partial p_i} \\ \frac{\partial p_{i+1}}{\partial x_i} & \frac{\partial p_{i+1}}{\partial p_i} \end{bmatrix} = \begin{bmatrix} 1 - K\cos x^* & 1 \\ -K\cos x^* & 1 \end{bmatrix}.$$

Note that $\det(J) = 1$ and $\mathrm{tr}(J) = 2 - K\cos x^* = 2 - K(-1)^n$, where $n \in \mathbb{Z}$. The eigenvalues of matrix J are given by

$$\lambda_{1,2} = \frac{\mathrm{tr}(J)}{2} \pm \sqrt{\frac{\mathrm{tr}(J)^2}{4} - \det(J)}. \tag{5.4}$$

From Eq. (5.4), the eigenvalues are real when $\mathrm{tr}(J) \leq -2$ or $\mathrm{tr}(J) \geq 2$, and are complex otherwise. If n is odd and $K > 0$, then $\mathrm{tr}(J) = 2 + K > 2$, so both eigenvalues are real with $|\lambda_1| > 1$ and $|\lambda_2| < 1$. Hence, the fixed points are unstable [77, 78]. If n is even, then $\mathrm{tr}(J) = 2 - K$, so the fixed points are stable for $0 \leq K \leq 4$ (complex eigenvalues with $\left|\lambda_{1,2}\right| \leq 1$) and unstable for $K > 4$ (real eigenvalues with $|\lambda_1| > 1$ and $|\lambda_2| < 1$).

5.2 Gaussian and q-Gaussian distributions

The Gaussian distribution function is given by

$$G(x) = G(0)e^{-bx^2} \tag{5.5}$$

for some parameter $b \in \mathbb{R}$. If we use the transformation $\widetilde{x} = xG(0)$, $\widetilde{G}(\widetilde{x}) = G(x)/G(0)$, and $\widetilde{b} = b/G(0)^2$, the Gaussian distribution in Eq. (5.5) can be written as

$$\widetilde{G}(\widetilde{x}) = e^{-\widetilde{b}\widetilde{x}^2}. \tag{5.6}$$

This transformation has the effect to normalise the Gaussian distribution function so that $\widetilde{G}(0) = 1$. Solving

$$\int_{-\infty}^{\infty} \widetilde{G}(\widetilde{x}) d\widetilde{x} = 1,$$

we obtain $\widetilde{b} = \pi$. Therefore, the Gaussian distribution in Eq. (5.6) is characterised by the parameter value $\widetilde{b} = \pi$.

Next, the q-Gaussian distribution function in general form is given by

$$G_q(x) = a \exp_q(-b_q x^2)$$

where

$$\exp_q(x) = (1 + (1-q)x)^{1/(1-q)}.$$

Using the same transformation as before, we have $\widetilde{x} = xG_q(0)$, $\widetilde{G}(\widetilde{x}) = G_q(x)/G_q(0)$, and obtain

$$\widetilde{G}_q(\widetilde{x}) = \exp_q\left(-\widetilde{b}\widetilde{x}^2\right). \tag{5.7}$$

Equation (5.7) is equivalent to

$$\widetilde{G}_q(\widetilde{x}) = (1-(1-q)b_q x^2)^{1/(1-q)}. \tag{5.8}$$

Note that the distribution in Eq. (5.8) converges to a Gaussian distribution (5.6) in the limit of $q \to 1$.

5.3 Probability distribution function of the standard map orbits

In this section, we explain the procedure to obtain the numerical probability distribution function (PDF) of a variable which is generated from the orbits of the standard map for a particular parameter K. The numerical PDF will be used to characterise the chaotic behaviour of the map.

To begin with, we choose randomly the initial condition $x_0^{(j)}$, for $j = 1,2,\ldots,M$. All these initial conditions are then iterated up to N number of iterations, and we define the random variables X_j as

$$X_j = \sum_{i=1}^{N} (x_i^{(j)} - \langle x \rangle), \quad j = 1, 2, \cdots, M, \tag{5.9}$$

where M is the number of randomly chosen initial conditions. $\langle x \rangle$ denotes the average over M and N, and is given by

$$\langle x \rangle = \frac{1}{M} \frac{1}{N} \sum_{j=1}^{M} \sum_{i=1}^{N} x_i^{(j)}.$$

To generate the numerical PDF, we first create the histogram of the random variables X_j where each bin in the histogram represents the relative probability. Then, we create a curve which serves as a numerical PDF of X_j. We present the Matlab function to create this numerical PDF in Algorithm 5.1, where the inputs to the function are the random variables X_j and the desired bin width. It is important to note that the resulting histogram has been normalised so that it is symmetric about the y-axis and centred at zero.

```
function [x,y]=pdf_binedges(y,binwidth)
    left_edges=[-binwidth/2:-binwidth:min(y)-binwidth];
    right_edges=[binwidth/2:binwidth:max(y)+binwidth];
    binedges=[fliplr(left_edges) right_edges];
    h=histogram(y,'Normalization','pdf','BinEdges',binedges);
    x=(h.BinEdges(1:end-1)+h.BinEdges(2:end))/2*max(h.Values);
    y=h.Values/max(h.Values);
end
```

Algorithm 5.1: Matlab code for generating a normalised PDF.

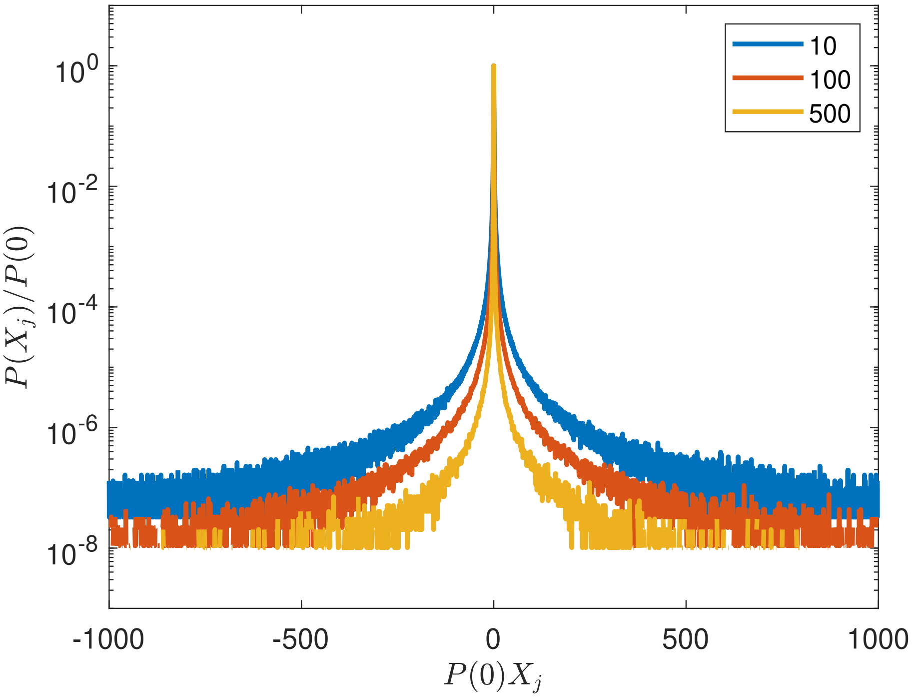

Figure 5.4. The normalised probability distribution function of the variable X_j for three different bin widths, namely for 10 (blue curve), 100 (red curve), and 500 (yellow curve). In all curves, $P(0)$ is set to be the height of the central bin which include 0.

To compute the PDF, we must carefully determine the bin width, as different bin widths will result in distinct PDF. Figure 5.4 illustrates the normalised PDF of X_j with various bin width, which has been constructed by using the Matlab code in Algorithm 5.1. In this case, we take the map parameter $K = 0$ and choose randomly 10^8 initial conditions that are iterated 2^{22} times. The severe fluctuation on both tails of the PDF is due to the fact that we can only consider a finite number of initial conditions N. These tails will become smoother as N increases. Therefore, we must limit our domain to an interval in which the PDF does not contain highly fluctuated tails. We show the PDF in a shorter interval in Fig. 5.5.

The probability distribution function of X_j for several K values has been studied in [18]. The authors chose the value of K to accommodate the fact that the phase plane contains both regular and chaotic orbits, as illustrated in Figs. 5.2-5.3. The authors obtained the same q value for the q-Gaussian distribution when they fitted

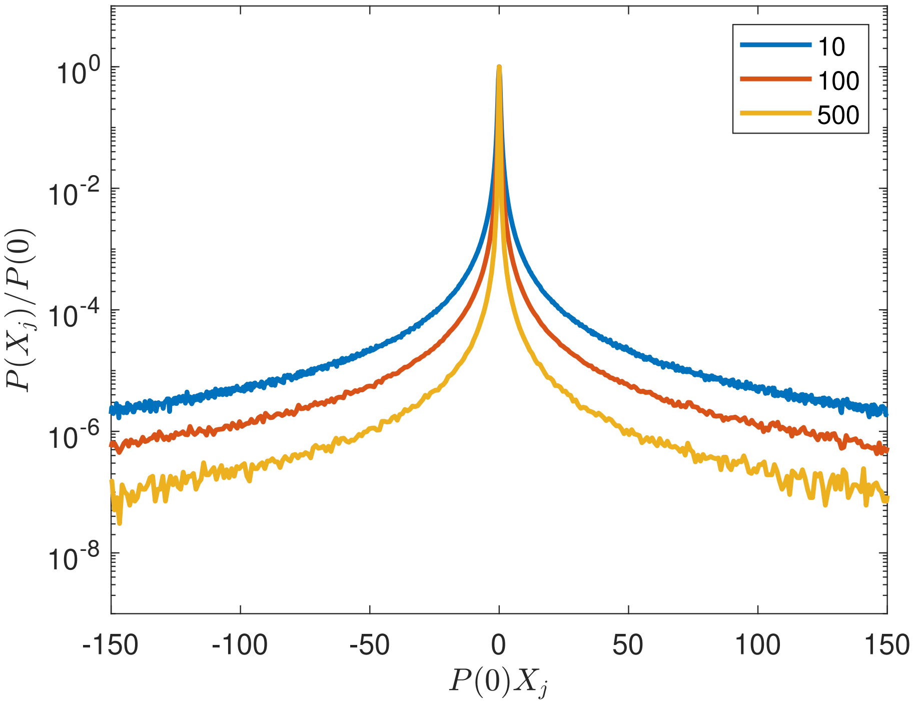

Figure 5.5. The normalised probability distribution function of the variable X_j, similar to that shown in Fig. 5.4 but for a smaller interval.

the numerical PDF with its corresponding distribution, which is $q \approx 1.935$. In their study, they observed the numerical PDF is either a Gaussian, a q-Gaussian, or a mixed PDF which is a linear combination of a Gaussian and a q-Gaussian distribution. We reproduce the results in their paper in Figs. 5.6-5.7 by using the same number of trajectories and also plot its corresponding distribution using the obtained distribution parameters. We choose the bin width appropriately to align with the distribution function.

The process of fitting the numerical PDF with its appropriate distribution is described in the following section. We will focus on the case where the numerical PDF is well approximated by the Gaussian in the chaotic case and the q-Gaussian in the regular and weakly chaotic cases.

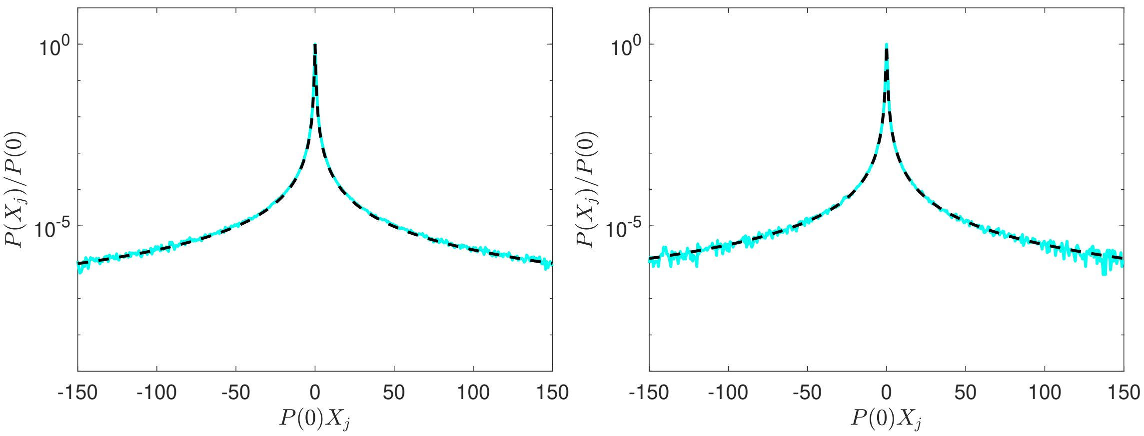

(a) **(b)**

Figure 5.6. Numerical PDF (blue curve) and a q-Gaussian distribution (black curve) for $K = 0.2$ (panel (a)) and $K = 2$ (panel (b)), where the initial conditions are taken from a stability island only. The number of initial conditions are 4×10^7 and 10^7 in panel (a) and (b), respectively. In both cases, the map is iterated 2^{22} times. The q-Gaussian distribution is given in Eq. (5.8) with parameter values $q = 1.935$ and $b_q = 21$ in panel (a) and $q = 1.935$ and $b = 15.5$ in panel (b).

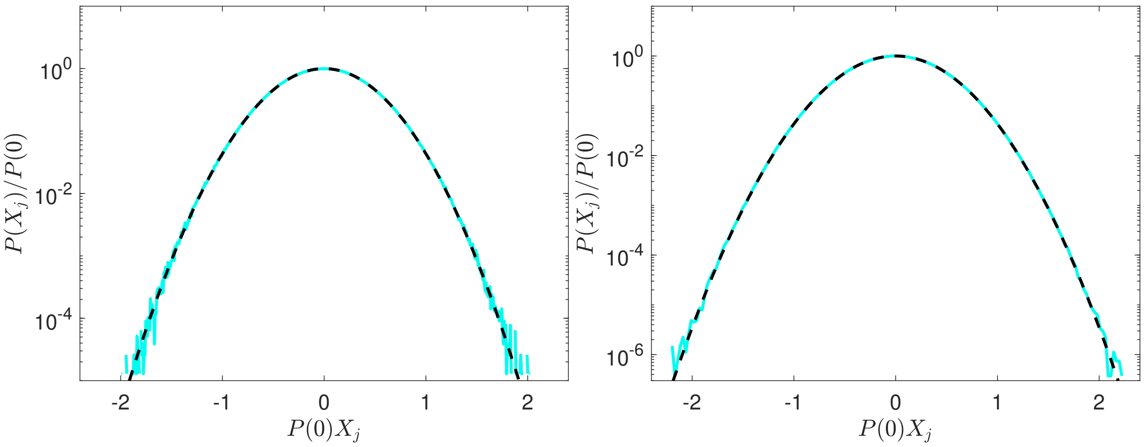

(a) **(b)**

Figure 5.7. Numerical PDF (blue curve) and a q-Gaussian distribution (black curve) for $K = 10$ (panel (a)) and $K = 2$ (panel (b)), where the initial conditions are taken from the chaotic sea only. The number of initial conditions in both cases are 10^7 and the map is iterated 2^{22} times. The q-Gaussian distribution is given in Eq. (5.8) with parameter values $q = 1$ and $b_q = 3.14$ in both panels, which points to a Gaussian PDF.

5.4 Fitting method

The numerical PDFs can vary significantly depending on the number of bins used to compute them, as we discussed in the previous section. As a result, we need to select the optimum PDF from all of the available PDFs, which meets certain criteria. In this context, our criteria are (1) the PDF must best fit the Gaussian function for the chaotic case and the q-Gaussian function for the regular case with the smallest possible error and (2) the PDF must have an area of 1.

Here, we describe the procedure to determine the parameters for the Gaussian and q-Gaussian functions by using a curve fitting approach. For easy reference, we rewrite the q-Gaussian distribution function as

$$G_q(x) = a\left(1 - b(1-q)x^2\right)^{\frac{1}{1-q}}, \tag{5.10}$$

where a, b, q are the distribution parameters. We aim to have as little inaccuracy as possible when fitting the q-Gaussian distribution into the numerical PDF. At the same time, we need to identify the parameters that would give us the area under its function equal 1, which is a property of PDFs. We see this as a multi-optimisation problem. Therefore, we define two objective functions $f_1(x)$ and $f_2(x)$ as follow

$$f_1(x) = \int_{\Omega(\epsilon)} \left|P(x) - G_q(x)\right| \, dx, \tag{5.11}$$

$$f_2(x) = \left|1 - \int_{-\infty}^{\infty} G_q(x) \, dx\right|, \tag{5.12}$$

where

$$\Omega(\epsilon) = [-L, -L+\epsilon] \cup [L-\epsilon, L].$$

In this context, $2L$ represents the length of the interval for the numerical PDF under consideration. Furthermore, ϵ specifies the tail length of the numerical PDF. The first objective function $f_1(x)$ measures the distance between $P(x)$ and $G_q(x)$, while the second objective function $f_2(x)$ measures how close the area under $G_q(x)$ is to 1. Our goal now is to find the distribution parameters (a, b, q) for Eq. (5.10) that minimise these two functions with respect to all possible numerical PDFs, that dependant on the bin width, as described in Sec (5.3).

Since $\Omega(\epsilon) = [-L, L]$ when $\epsilon = L$, the formula in Eq. (5.11) is the $\mathcal{L}_1$ norm in the interval $[-L, L]$ [79]. We use this norm as the error function to measure the distance between $P(x)$ and $G_q(x)$ that we want to minimise. We choose this norm because it gives us the most satisfactory results compared to other norm functionals or to other goodness of fit measures such as sum of squares due to error (sse) or root mean squared error (rmse). When $0 < \epsilon < L$, especially when ϵ is sufficiently small, the first objective function $f_1(x)$ can be seen as the distance between $P(x)$ and $G_q(x)$ on both tails. In our method, we solve the multi-objective optimisation problem by starting with a small value of ϵ, i.e. fit $P(x)$ with $G_q(x)$ on both tail, and gradually increase ϵ until it covers the whole interval, i.e. $\epsilon = L$.

Let

$$\Lambda = \Big\{(x_i, y_i) : y_i = P(x_i), \text{ where } P \text{ is a numerical PDF of variable } X \text{ given in Eq. (5.9) for all possible bin widths } w\Big\}.$$

We consider the multi-objective optimisation problem

$$\min\{f_1(x) \text{ and } f_2(x)\} \tag{5.13}$$

where we want to minimise at the same time both $f_1(x)$ and $f_2(x)$ subject to

$$P(x) \in \Lambda, \tag{5.14}$$

$$\epsilon \in [0, L]. \tag{5.15}$$

This multi-objective optimisation problem is solved using a procedure described in Algorithm 5. This algorithm relies largely on a genetic algorithm [80]. The solver is called *gamultiobj* which is a function available in the global optimisation toolbox in Matlab [81]. The solver will produce a set of non-inferior solutions, which are solutions that cannot be improved in one objective without worsening it in another.

An individual in the *gamultiobj* function is the vector with coordinate (a, b, q) where a, b, q are the parameters for the q-Gaussian distribution given in Eq. (5.10). A population consists of a collection of individuals. The first step in the *gamultiobj* algorithm is creating an initial population, which is set to 500 in our computations. This initial population is uniformly chosen within the individual bounds. As we consider the normalised PDF, we take a in the small interval around 1 and $b > 0$. Additionally, the values of q lie on the interval [1,3] [40]. After the initial population has been generated, the *gamultiobj* algorithm carries out iterations according to the following main steps: [81]

1. Select parents for the next generation using the selection function on the current population.
2. Create children from the selected parents by mutation and crossover.
3. Score the children by calculating their objective function values and feasibility.
4. Combine the current population and the children into one matrix, the extended population.
5. Compute the rank and crowding distance for all individuals in the extended population.
6. Trim the extended population to have a population with the same number as the initial population by retaining the appropriate number of individuals of each rank.

The selection, mutation, and crossover operators are binary tournament, Gaussian mutation, and crossover scattered, respectively. We stop the iteration if it exceeds the maximum number of iterations, which is set to 10^4. In addition, we also set the function tolerance to 10^{-4} as the second stopping criteria. We have experimented with various combinations of the maximum number of iterations and the function tolerance. This option offers the most optimal numerical fitting and computational efficiency.

In our computations, L is set to 150 for regular cases and 2 for chaotic cases. In addition, we select the bin width within the interval $[1,150]$, as the bin width less than 1 will result in a highly fluctuated curve and the bin width larger than 150 will lead to a curve that will be far from the optimum solution.

Algorithm 5 q-Gaussian distribution fitting procedure.

```
Input: Variables $X_j$ as given in Eq. (5.9), length of the fitting interval $L$, bin width minimum $w_{\text{min}}$, bin width maximum $w_{\text{max}}$.
Output: $q$-Gaussian distribution parameters $(a,b,q)$, objective functions value $f_1(x)$ and $f_2(x)$.
$\mathcal{S} \leftarrow \emptyset$
for $\epsilon = 0$ to $L$ do
    for $w = w_{\text{min}}$ to $w_{\text{max}}$ do
        Generate numerical PDF with bin width $w$.
        Solve Eq. (5.13) subject to (5.14)-(5.15) using genetic algorithm multi-objective solver.
        Store all solutions $(a,b,q)$ in $\mathcal{N}$.
    end for
    for $k = 1$ to length($\mathcal{N}$) do
        $f_1^L(x) \leftarrow f_1(x)$ for $x \in \Omega(L)$, using parameters $\mathcal{N}(k)$
        $\mathcal{P}(k) \leftarrow f_1^L(x) + f_2(x)$, using parameters $\mathcal{N}(k)$.
    end for
    Compute $\min\{\mathcal{P}\}$. Store the corresponding set of parameter from $\mathcal{N}$ to $\mathcal{S}$.
end for
for $k = 1$ to length($\mathcal{S}$) do
    for $\epsilon = 0$ to $L$ do
        $f_1^{\text{opt}}(x) \leftarrow f_1(x)$ for $x \in \Omega(\epsilon)$, using parameters $\mathcal{S}(k)$
        $\mathcal{P}^{opt}(k) \leftarrow f_1^{\text{opt}}(x)$, using parameters $\mathcal{S}(k)$.
    end for
end for
Compute $\min\{\mathcal{P}^{opt}\}$. Report the corresponding set of parameter from $\mathcal{S}$ as the optimum solution $\mathcal{S}^{\text{opt}}$.
Compute $f_1(x)$ and $f_2(x)$ using set of parameters in $\mathcal{S}^{\text{opt}}$.
```

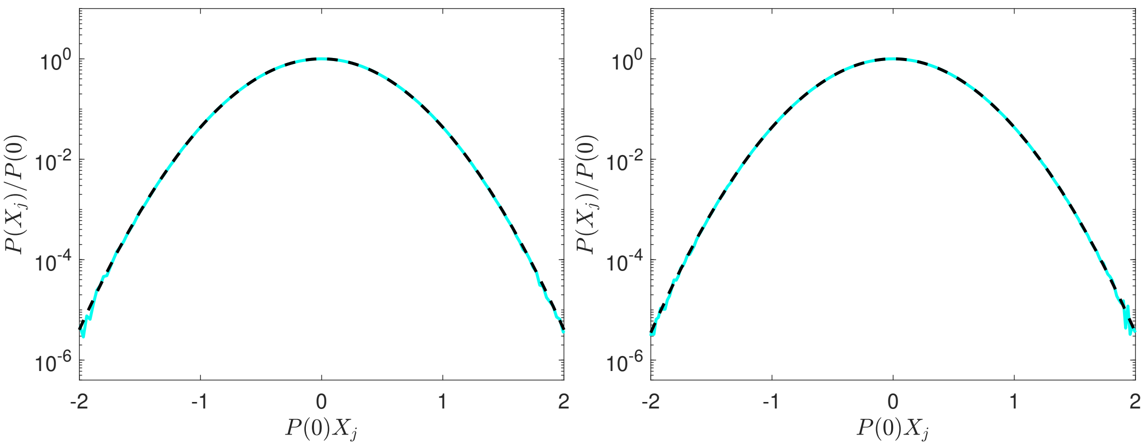

(a) $K = 2$ Chaotic only

(b) $K = 10$

Figure 5.8. The numerical PDF of the standard map (turquoise curve) and its corresponding q-Gaussian function (dashed black curve) for $K = 2$ (panel (a)) and $K = 10$ (panel b). Note that the initial conditions of all trajectories are located in the chaotic region. The Gaussian distribution parameters are $b = 3.14673$ and $q = 1.00218$ in panel (a) and $b = 3.14208$ and $q = 1.00021$ in panel (b).

5.5 Results

5.5.1 Chaotic case

In the case of chaotic dynamics, we expect to see a Gaussian distribution given by Eq. (5.6). The parameters that we acquire for Eq. (5.10) for $K = 10$ are $b = 3.14208$ and $q = 1.00021$. These values are quite similar to the Gaussian distribution parameter values that are given in Eq. (5.6), which are $b = pi$ and $q = 1$. For $K = 2$ where the initial conditions are taken from the chaotic sea, the Gaussian distribution parameter values are $b = 3.14673$ and $q = 1.00218$, which again give an excellent agreement with the parameters of the theoretical Gaussian distribution. Figure 5.8 shows the plot of the numerical PDFs with their respective Gaussian distribution where the parameters were obtained numerically. The values of the objective function for $K = 2$ are $f_1(x) = 1.20393 \times 10^{-3}$ and $f_2(x) = 8.83192 \times 10^{-7}$, and for $K = 10$ are $f_1(x) = 8.0878 \times 10^{-4}$ and $f_2(x) = 7.0957 \times 10^{-9}$.

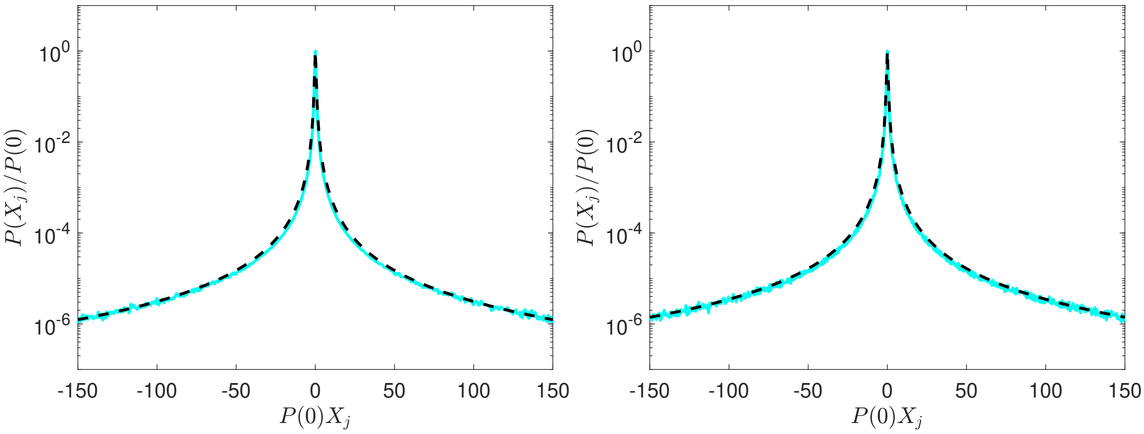

(a) $K = 0.2$ **(b)** $K = 2$ Stable only

Figure 5.9. The numerical PDF of the standard map and its corresponding q-Gaussian function for $K = 0$, $K = 0.2$ and $K = 2$. Note that the initial conditions of all trajectories are located in a stable region.

5.5.2 Regular case

First, we report the result for $K = 0.2$. The q-Gaussian distribution parameter values are given by $a = 1$, $b = 8.10219$ and $q = 1.88153$. The optimum objective function values are $f_1(x) = 5.74158 \times 10^{-02}$ and $f_2(x) = 1.11022 \times 10^{-15}$.

For $K = 2$ where all the initial conditions are taken randomly from the region of a stability island, the parameters of the q-Gaussian distribution are $a = 1$, $b = 8.23001$ and $q = 1.89159$. The optimum objective function values are $f_1(x) = 6.74877 \times 10^{-2}$ and $f_2(x) = 4.77706 \times 10^{-9}$. Figure 5.9 shows the plot of the numerical PDF with its corresponding q-Gaussian distribution for $K = 0.2$ and $K = 2$.

Now, we turn our attention to the case when $K = 0$. This is an example of an integrable map and has been reported in [82] to obey the q-Gaussian distribution with $q = 2$. Here, we consider two cases with different number of initial conditions, namely with $M = 10^8$ and $M = 10^9$ initial conditions. The parameter values for $M = 10^8$ are $a = 1$, $b = 8.42148$ and $q = 1.90619$. The optimum objective function values are $f_1(x) = 6.14898 \times 10^{-02}$ and $f_2(x) = 3.64456 \times 10^{-8}$. Next, for $M = 10^9$ we

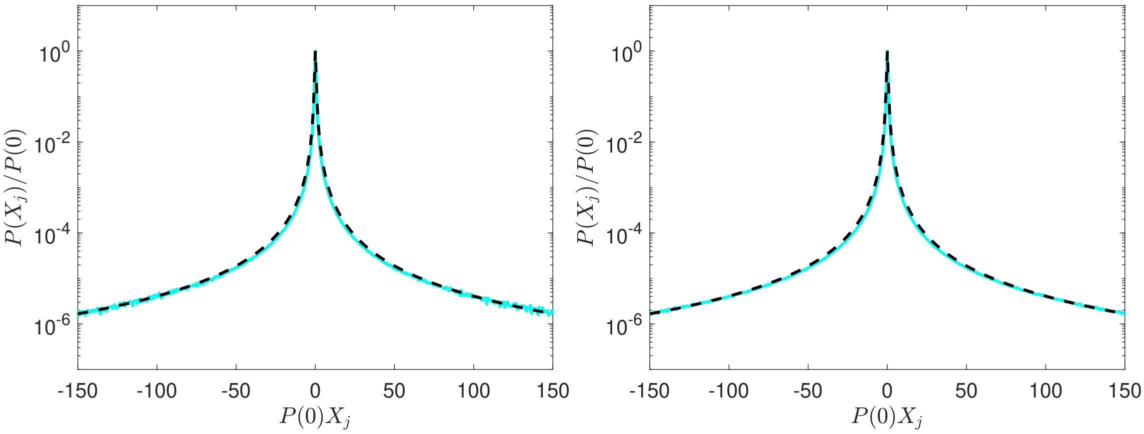

(a) $K = 0$ with 10^8 initial conditions

(b) $K = 0$ with 10^9 initial conditions

Figure 5.10. The numerical PDF of the standard map and its corresponding q-Gaussian function for $K = 0$ for (a) $M = 10^8$ initial conditions and (b) for $M = 10^9$ initial conditions.

obtain $a = 1$, $b = 8.46807$ and $q = 1.90966$. The optimum objective function values are $f_1(x) = 5.56503 \times 10^{-02}$ and $f_2(x) = 5.67387 \times 10^{-7}$. We present the corresponding plot in Fig. 5.10.

It is worth noting that the q values here is very close to the analytical value provided in [82]. Furthermore, as we increase the number of orbits utilised to generate the variables X_j, as described in equation (5.9), the corresponding value of q also increases, even though by a small margin. This observation might mean that obtaining an accurate distribution with $q = 2$ might require an extremely high number of orbits.

5.6 Conclusion

In this chapter, we have examined the PDF derived from the standard map in both chaotic and regular cases. The aim was to develop a comprehensive procedure for determining the parameters of the q-Gaussian function, which serves as an effective tool for fitting the numerical PDF obtained from regular and chaotic areas of the phase space of the standard map.

To accomplish this, we employed a multi-objective optimisation approach utilising a genetic algorithm. This approach allowed us to address the challenge of finding the optimal set of parameters for the q-Gaussian function, which would result in a well-fitted representation of the numerical PDF. By formulating the problem as a multi-objective optimisation task, we were able to simultaneously consider multiple objectives, such as minimising the difference between the fitted q-Gaussian function and the numerical PDF, while also fulfilling the property of a probability distribution function.

Through the utilisation of the genetic algorithm, we iteratively searched for the optimal set of parameters that yielded the best fit to the numerical PDF. This involved generating candidate solutions (individuals) with different parameter combinations and evaluating their fitness based on the defined objectives. The genetic algorithm's ability to explore the parameter space and converge towards promising solutions allowed us to obtain a set of parameters for the q-Gaussian function that provided a highly accurate fit to the numerical PDF from phase space of the standard map.

By employing this procedure, we were able to effectively model the statistical properties of the regular and chaotic phase space of the standard map and obtain a comprehensive understanding of its behaviour. The well-fitted q-Gaussian function serves as a valuable tool for analysing and characterising the probability distribution within the phase space, enhancing our understanding of the dynamics and statistical properties of the standard map.

Chapter 6

Conclusions and future work

6.1 Conclusions

This thesis presents initially a comprehensive and systematic study of the disordered FPUT-α lattice system, focusing on two different models. Firstly, we investigate the system with disorder in the nonlinear coupling terms. The motivation behind this study is rooted to the observation that in the absence of variability, introducing nonlinearity alone does not ensure energy equipartition. By incorporating disorder into the nonlinear coupling terms, we demonstrate its impact on breaking the recurrence phenomenon. Furthermore, we discover the existence of a tolerance threshold, beyond which the system's solution experiences blow-up within a finite time. To explain the localisation of energy, we derive a two normal-mode system that explains the underlying mechanism and provide a bifurcation diagram illustrating the system's parameters. In terms of chaotic behaviour, we find that introducing variability enhances the possibility of observing chaotic trajectories. This highlights how disorder in the system can significantly alter the nature of solutions from regular to chaotic.

The second model studied is the FPUT-α Hamiltonian with variability. At a fixed energy level, we observe that increasing the percentage of variability leads to energy localisation. We also derive a two normal-mode system when energy localization occurs and provide a bifurcation diagram in the parameter space, further elucidating on the localisation phenomenon. The chaotic behaviour of this system exhibits a complex nature as we vary the lattice size and percentage of variability. Generally, we observe that variability enhances the likelihood of observing chaotic trajectories for small lattice sizes. However, the behaviour becomes more intricate for medium lattice sizes, and there appears to be a reversal of the effect for large lattice sizes.

In addition to the FPUT-α system, we also applied q-Statistics to study the chaotic behaviour of the standard map for both chaotic and regular cases. We developed a systematic procedure to obtain the parameters of the q-Gaussian function that best fits the numerical probability distribution of the standard map. Employing a genetic algorithm approach, we successfully solved the multi-objective optimisation problem and determined the optimal parameters of the q-Gaussian function.

6.2 Future work

The field of nonlinear dynamics has witnessed substantial advancements since the pioneering experiments conducted by Fermi, Pasta, Ulam, and Tsingou in 1950s.

As a result, numerous avenues for future investigations have emerged, reflecting the extensive potential for further research in this field.

In the realm of 1D lattice systems, there are exciting opportunities for future research in exploring the disordered FPUT-β lattice system, which exhibits a distinct nature compared to the FPUT-α model. There are two key areas of investigation that can be pursued.

Firstly, investigating the impact of introducing variability in the FPUT-β lattice system as the initial energy of the system is gradually increased. This exploration can shed light on how the behaviour of the system, such as energy redistribution, recurrence phenomenon, and chaotic dynamics, is influenced by varying degrees of variability.

Next, exploring the effects of exciting different modes to initiate the FPUT-β lattice system. This analysis can provide insights into the system's response, energy localisation, mode coupling, and the emergence of patterns and structures as different modes are selectively excited.

In the field of q-Statistics, there is a promising option for future research that involves analysing the probability distribution function in the weakly chaotic region of the standard map. The identification of the region in the phase space of the standard map that corresponds to weakly chaotic behaviour is a fundamental component of this research. This can be performed by applying well-established chaotic indicators such as the Lyapunov exponent or Smaller Alignment Index (SALI). Such indicators may identify the specific trajectories associated with weakly chaotic dynamics. Then, we can investigate the probability distribution of this system using a method similar to that used in this thesis.

Bibliography

[1] E. Fermi, J. Pasta, and S. Ulam, “Los Alamos report LA-1940,” *Fermi, Collected Papers*, vol. 2, pp. 977–988, 1955.

[2] J. Ford, “The Fermi-Pasta-Ulam problem: Paradox turns discovery,” *Physics Reports*, vol. 213, no. 5, p. 271–310, 1992.

[3] T. Dauxois, M. Peyrard, and S. Ruffo, “The Fermi–Pasta–Ulam ‘numerical experiment’: history and pedagogical perspectives,” *European Journal of Physics*, vol. 26, no. 5, p. S3, 2005.

[4] G. P. Berman and F. M. Izrailev, “The Fermi-Pasta-Ulam problem: Fifty years of progress,” *Chaos*, vol. 15, no. 1, 2005.

[5] N. J. Zabusky and M. D. Kruskal, “Interaction of" solitons" in a collisionless plasma and the recurrence of initial states,” *Physical Review Letters*, vol. 15, no. 6, p. 240, 1965.

[6] C. Antonopoulos, T. Bountis, and C. Skokos, “Chaotic dynamics of N-degree of freedom hamiltonian systems,” *International Journal of Bifurcation and Chaos*, vol. 16, no. 6, pp. 1777–1793, 2006.

[7] C. Antonopoulos and T. Bountis, “Detecting order and chaos by the linear dependence index (LDI) method,” *Romai Journal*, vol. 2, no. 2, pp. 1–13, 2006.

[8] C. Danieli, B. M. Manda, M. Thudiyangal, and C. Skokos, “Computational efficiency of numerical integration methods for the tangent dynamics of many-body Hamiltonian systems in one and two spatial dimensions,” *Mathematics in Engineering*, vol. 1, no. 3, pp. 447–488, 2019.

[9] C. H. Skokos and T. Manos, “The Smaller (SALI) and the Generalized (GALI) alignment indices: Efficient methods of chaos detection,” in *Chaos Detection and Predictability*, pp. 129–181, Springer, 2016.

[10] J. L. Tuck and M. T. Menzel, “The superperiod of the nonlinear weighted string (FPU) problem,” *Advances in Mathematics*, vol. 9, no. 3, pp. 399–407, 1972.

[11] S. D. Pace and D. K. Campbell, “Behavior and breakdown of higher-order Fermi-Pasta-Ulam-Tsingou recurrences,” *Chaos: An Interdisciplinary Journal of Nonlinear Science*, vol. 29, no. 2, p. 23132, 2019.

[12] K. A. Reiss and D. K. Campbell, “The Metastable State of Fermi–Pasta–Ulam–Tsingou Models,” *Entropy*, vol. 25, no. 2, p. 300, 2023.

[13] M. Toda, “Vibration of a chain with nonlinear interaction,” *Journal of the Physical Society of Japan*, vol. 22, no. 2, pp. 431–436, 1967.

[14] U. Tirnakli, C. Beck, and C. Tsallis, "Central limit behavior of deterministic dynamical systems," *Physical Review E - Statistical, Nonlinear, and Soft Matter Physics*, vol. 75, no. 4, pp. 1–6, 2007.

[15] N. G. Van Kampen, *Stochastic processes in physics and chemistry*, vol. 1. Elsevier, 1992.

[16] U. Tirnakli, C. Tsallis, and C. Beck, "Closer look at time averages of the logistic map at the edge of chaos," *Physical Review E - Statistical, Nonlinear, and Soft Matter Physics*, vol. 79, no. 5, pp. 1–9, 2009.

[17] C. Tsallis and U. Tirnakli, "Nonadditive entropy and nonextensive statistical mechanics–some central concepts and recent applications," in *Journal of Physics: Conference Series*, vol. 201, p. 012001, IOP Publishing, 2010.

[18] U. Tirnakli and E. P. Borges, "The standard map: From Boltzmann-Gibbs statistics to Tsallis statistics," *Scientific Reports*, vol. 6, pp. 2–9, 2016.

[19] U. Tirnakli and C. Tsallis, "Extensive numerical results for integrable case of standard map," *Nonlinear Phenomena in Complex Systems*, vol. 23, no. 2, pp. 149–152, 2020.

[20] D. Kulkarni, D. Schmidt, and S.-K. Tsui, "Eigenvalues of tridiagonal pseudo-Toeplitz matrices," *Linear Algebra and its Applications*, vol. 297, pp. 63–80, 1999.

[21] T. Stuchi, "Symplectic integrators revisited," *Brazilian Journal of Physics*, vol. 32, pp. 958–979, 2002.

[22] K. E. Atkinson, W. Han, and D. E. Stewart, *Numerical Solution of Ordinary Differential Equations*. Berlin: John Wiley & Sons, Ltd, 2011.

[23] F. Neri, "Lie algebras and canonical integration, Department of Physics, University of Maryland, preprint (1988),"

[24] J. F. Boudreau and E. S. Swanson, *Applied computational physics*. Oxford University Press, 2017.

[25] R. D. Ruth, "A canonical integration technique," *IEEE Trans. Nucl. Sci.*, vol. 30, no. CERN-LEP-TH-83-14, pp. 2669–2671, 1983.

[26] H. Yoshida, "Construction of higher order symplectic integrators," *Physics Letters A*, vol. 150, no. 5-7, pp. 262–268, 1990.

[27] C. Skokos, "The Lyapunov characteristic exponents and their computation," in *Dynamics of Small Solar System Bodies and Exoplanets*, pp. 63–135, Springer, 2010.

[28] A. M. Lyapunov, "The general problem of the stability of motion," *International Journal of Control*, vol. 55, no. 3, pp. 531–534, 1992.

[29] T. Bountis and H. Skokos, *Complex Hamiltonian dynamics*, vol. 10. Springer Science & Business Media, 2012.

[30] A. Pikovsky and A. Politi, *Lyapunov exponents: a tool to explore complex dynamics*. Cambridge University Press, 2016.

[31] H. Haken, "At least one Lyapunov exponent vanishes if the trajectory of an attractor does not contain a fixed point," *Physics Letters A*, vol. 94, no. 2, pp. 71–72, 1983.

[32] G. Benettin, L. Galgani, A. Giorgilli, and J.-M. Strelcyn, "Lyapunov characteristic exponents for smooth dynamical systems and for Hamiltonian systems; a method for computing all of them. Part 1: Theory," *Meccanica*, vol. 15, no. 1, pp. 9–20, 1980.

[33] C. Skokos, "Alignment indices: a new, simple method for determining the ordered or chaotic nature of orbits," *Journal of Physics A: Mathematical and General*, vol. 34, no. 47, p. 10029, 2001.

[34] C. Skokos, C. Antonopoulos, T. C. Bountis, and M. N. Vrahatis, "How does the Smaller Alignment Index (SALI) distinguish order from chaos?," *Progress of Theoretical Physics Supplement*, vol. 150, pp. 439–443, 2003.

[35] C. Skokos, C. Antonopoulos, T. C. Bountis, and M. N. Vrahatis, "Detecting order and chaos in Hamiltonian systems by the SALI method," *Journal of Physics A: Mathematical and General*, vol. 37, no. 24, p. 6269, 2004.

[36] "DOP853 integrator." http://www.unige.ch/~hairer/software.html.

[37] C. Skokos and E. Gerlach, "Numerical integration of variational equations," *Physical Review E*, vol. 82, no. 3, p. 36704, 2010.

[38] J. Laskar and P. Robutel, "High order symplectic integrators for perturbed Hamiltonian systems," *Celestial Mechanics and Dynamical Astronomy*, vol. 80, no. 1, pp. 39–62, 2001.

[39] M. Hénon and C. Heiles, "The applicability of the third integral of motion: some numerical experiments," *The Astronomical Journal*, vol. 69, p. 73, 1964.

[40] C. Tsallis, *Introduction to nonextensive statistical mechanics: approaching a complex world*. Springer Science & Business Media, 2009.

[41] C. Tsallis, "Possible generalization of Boltzmann-Gibbs statistics," *Journal of statistical physics*, vol. 52, pp. 479–487, 1988.

[42] S. Umarov, C. Tsallis, and S. Steinberg, "On a q-central limit theorem consistent with nonextensive statistical mechanics," *Milan Journal of Mathematics*, vol. 76, no. 1, pp. 307–328, 2008.

[43] U. Tirnakli and C. Tsallis, "Extensive numerical results for integrable case of standard map," *Nonlinear Phenomena in Complex Systems*, vol. 23, no. 2, pp. 149–152, 2020.

[44] C. G. Antonopoulos, C. Skokos, T. Bountis, and S. Flach, "Analyzing chaos in higher order disordered quartic-sextic Klein-Gordon lattices using q-statistics," *Chaos, Solitons & Fractals*, vol. 104, pp. 129–134, 2017.

[45] V. Rumyantsev, S. Fedorov, K. Gumennyk, and M. Sychanova, "Dispersion characteristics of electromagnetic excitations in a disordered one-dimensional lattice of coupled microresonators," *Physica B: Condensed matter*, vol. 461, pp. 32–37, 2015.

[46] Y. Lahini, A. Avidan, F. Pozzi, M. Sorel, R. Morandotti, D. N. Christodoulides, and Y. Silberberg, "Anderson localization and nonlinearity in one-dimensional disordered photonic lattices," *Physical Review Letters*, vol. 100, no. 1, p. 013906, 2008.

[47] A. Bovier, *Statistical mechanics of disordered systems: a mathematical perspective*, vol. 18. Cambridge University Press, 2006.

[48] B. Li, H. Zhao, and B. Hu, "Can disorder induce a finite thermal conductivity in 1d lattices?," *Physical Review Letters*, vol. 86, no. 1, p. 63, 2001.

[49] T. Liu and H. Guo, "Topological phase transition in the quasiperiodic disordered Su–Schriffer–Heeger chain," *Physics Letters A*, vol. 382, no. 45, pp. 3287–3292, 2018.

[50] S. Longhi, D. Gatti, and G. Della Valle, "Non-Hermitian transparency and one-way transport in low-dimensional lattices by an imaginary gauge field," *Physical Review B*, vol. 92, no. 9, p. 094204, 2015.

[51] M. Kastner, "Monte Carlo methods in statistical physics: Mathematical foundations and strategies," *Communications in Nonlinear Science and Numerical Simulation*, vol. 15, no. 6, pp. 1589–1602, 2010.

[52] M. E. Newman and G. T. Barkema, *Monte Carlo methods in statistical physics*. Clarendon Press, 1999.

[53] A. Weiße and H. Fehske, "Exact diagonalization techniques," *Computational many-particle physics*, pp. 529–544, 2008.

[54] P. W. Anderson, "Absence of diffusion in certain random lattices," *Physical Review*, vol. 109, no. 5, p. 1492, 1958.

[55] P. Sierant, D. Delande, and J. Zakrzewski, "Many-body localization due to random interactions," *Physical Review A*, vol. 95, no. 2, p. 021601, 2017.

[56] J. Naudts and K. Michel, "Lattice dynamics of a partially disordered crystal: A simple model," *Physical Review B*, vol. 18, no. 2, p. 667, 1978.

[57] H. Nelson, M. A. Porter, and B. Choubey, "Variability in Fermi-Pasta-Ulam-Tsingou arrays can prevent recurrences," *Phys. Rev. E*, vol. 98, p. 62210, dec 2018.

[58] C. M. Bender and S. A. Orszag, *Advanced mathematical methods for scientists and engineers I: Asymptotic methods and perturbation theory*. Springer Science & Business Media, 2013.

[59] H. Christodoulidi, C. Efthymiopoulos, and T. Bountis, "Energy localization on q-tori, long-term stability, and the interpretation of Fermi-Pasta-Ulam recurrences," *Physical Review E*, vol. 81, no. 1, p. 016210, 2010.

[60] J. Pickton and H. Susanto, "Integrability of PT-symmetric dimers," *Physical Review A*, vol. 88, no. 6, p. 63840, 2013.

[61] L. Berchialla, L. Galgani, and A. Giorgilli, "Localization of energy in FPU chains," *Discrete and Continuous Dynamical Systems*, vol. 11, no. 4, pp. 855–866, 2004.

[62] A. Ponno, H. Christodoulidi, C. Skokos, and S. Flach, "The two-stage dynamics in the Fermi-Pasta-Ulam problem: From regular to diffusive behavior," *Chaos: An Interdisciplinary Journal of Nonlinear Science*, vol. 21, no. 4, p. 043127, 2011.

[63] M. Ivanchenko and S. Flach, "Disorder-induced mobility edges and heat flow control in anharmonic acoustic chains," *Europhysics Letters*, vol. 94, no. 4, p. 46004, 2011.

[64] S. Flach, M. Ivanchenko, and N. Li, "Thermal conductivity of nonlinear waves in disordered chains," *Pramana*, vol. 77, pp. 1007–1014, 2011.

[65] S. Flach, M. Ivanchenko, and O. Kanakov, "q-Breathers and the Fermi-Pasta-Ulam problem," *Physical Review Letters*, vol. 95, no. 6, p. 064102, 2005.

[66] S. Flach, M. Ivanchenko, and O. Kanakov, "q-breathers in Fermi-Pasta-Ulam chains: Existence, localization, and stability," *Physical Review E*, vol. 73, no. 3, p. 036618, 2006.

[67] H. Christodoulidi and C. Efthymiopoulos, "Low-dimensional q-tori in FPU lattices: Dynamics and localization properties," *Physica D: Nonlinear Phenomena*, vol. 261, pp. 92–113, 2013.

[68] C. Skokos, T. C. Bountis, and C. Antonopoulos, "Geometrical properties of local dynamics in Hamiltonian systems: The Generalized Alignment Index (GALI) method," *Physica D: Nonlinear Phenomena*, vol. 231, no. 1, pp. 30–54, 2007.

[69] S. V. Manakov, "Complete integrability and stochastization of discrete dynamical systems," *Soviet Journal of Experimental and Theoretical Physics*, vol. 40, no. 2, pp. 269–274, 1975.

[70] G. Benettin and A. Ponno, "Time-scales to equipartition in the Fermi–Pasta–Ulam problem: finite-size effects and thermodynamic limit," *Journal of Statistical Physics*, vol. 144, pp. 793–812, 2011.

[71] G. P. Drago and S. Ridella, "Some more observations on the superperiod of the non-linear FPU system," *Physics Letters A*, vol. 122, no. 8, pp. 407–412, 1987.

[72] D. S. Sholl and B. I. Henry, "Recurrence times in cubic and quartic Fermi-Pasta-Ulam chains: A shifted-frequency perturbation treatment," *Physical Review A*, vol. 44, no. 10, p. 6364, 1991.

[73] C. G. Antonopoulos, T. Bountis, C. Skokos, and L. Drossos, "Complex statistics and diffusion in nonlinear disordered particle chains," *Chaos: An Interdisciplinary Journal of Nonlinear Science*, vol. 24, no. 2, 2014.

[74] C. G. Antonopoulos, T. Bountis, and L. Drossos, "Coupled symplectic maps as models for subdiffusive processes in disordered hamiltonian lattices," *Applied Numerical Mathematics*, vol. 104, pp. 110–119, 2016.

[75] C. G. Antonopoulos and H. Christodoulidi, "Weak chaos detection in the Fermi–Pasta–Ulam-α system using q-Gaussian statistics," *International Journal of Bifurcation and Chaos*, vol. 21, no. 08, pp. 2285–2296, 2011.

[76] C. Antonopoulos, T. Bountis, and V. Basios, "Quasi-stationary chaotic states in multi-dimensional hamiltonian systems," *Physica A: Statistical Mechanics and its Applications*, vol. 390, no. 20, pp. 3290–3307, 2011.

[77] S. N. Rasband, *Chaotic dynamics of nonlinear systems*. John Willey & Sons, Inc, 1990.

[78] O. Galor, *Discrete dynamical systems*. Springer Science & Business Media, 2007.

[79] E. M. Stein and R. Shakarchi, *Functional analysis: introduction to further topics in analysis*, vol. 4. Princeton University Press, 2011.

[80] K. Deb, “Multi-objective optimisation using evolutionary algorithms: an introduction,” in *Multi-objective evolutionary optimisation for product design and manufacturing*, pp. 3–34, Springer, 2011.

[81] The MathWorks Inc., “gamultiobj Algorithm.” https://uk.mathworks.com/help/gads/gamultiobj-algorithm.html, 2023.

[82] A. Bountis, J. J. P. Veerman, and F. Vivaldi, “Cauchy distributions for the integrable standard map,” *Physics Letters A*, vol. 384, no. 26, p. 126659, 2020.

[83] F. Verhulst, *Nonlinear differential equations and dynamical systems*. Springer Science & Business Media, 2006.

Appendix: Duffing equation

We compare the solution to Duffing equation using Poincaré-Lindstedt series [83] and multiple-scale analysis [58]. The undamped, unforced Duffing equation is given by

$$\ddot{x} + x + \epsilon x^3 = 0, \tag{1}$$

for $t > 0$, with $0 < \epsilon \ll 1$. Consider the initial conditions

$$x(0) = 1, \quad \dot{x} = 0. \tag{2}$$

The solution to this problem using Poincaré-Lindstedt method is given by [83]

$$x(t) = \cos\left(\left(1 + \frac{3}{8}\epsilon\right)t\right) + \mathcal{O}(\epsilon^2). \tag{3}$$

Now, we will solve the problem using multiple-scale analysis [58]. Let

$$x(t) = x_0(T, t) + \epsilon x_1(T, t) + \mathcal{O}(\epsilon^2), \tag{4}$$

with $T = \epsilon t$ being the long time scale in multiple-scale expansion. At ϵ^0 we have

$$\frac{\partial^2 x_0}{\partial t^2} + x_0 = 0, \tag{5}$$

and the general solution is given by

$$x_0 = A(T)e^{it} + A^*(T)e^{-it}. \tag{6}$$

At ϵ^1 we have

$$2i\frac{\partial^2 x_0}{\partial T \partial t} + \frac{\partial^2 x_1}{\partial t^2} + x_1 + x_0^3 = 0, \tag{7}$$

$$2i\frac{\partial A}{\partial T}e^{it} - 2i\frac{\partial A^*}{\partial T}e^{-it} + \frac{\partial^2 x_1}{\partial t^2} + x_1 + x_0^3 = 0 \tag{8}$$

Noting that

$$x_0^3 = A^3 e^{3it} + A^{*3} e^{-3it} + 3A^2 e^{2it} A^* e^{-it} + 3A e^{it} A^{*2} e^{-2it} \tag{9}$$

and applying the standard solvability condition to avoid the secular terms, we obtain

$$\frac{\partial A}{\partial T} = \frac{3}{2} i A^2 A^*. \tag{10}$$

The solution to Eq. (10) is given by

$$A(T) = A(0)e^{3/2iTA^2(0)}. \tag{11}$$

Substituting Eq. (11) into Eq. (6), we obtain

$$x(t) = 2A(0)\cos((1 + 3/2\epsilon A^2(0))t) + O(\epsilon^2). \tag{12}$$

where we have used $T = \epsilon t$ in this equation. Using initial condition $x(0) = 1$, we obtain $A(0) = 1/2$, and the solution becomes

$$x(t) = \cos\left(\left(1 + \frac{3}{8}\epsilon\right)t\right) + O(\epsilon^2). \tag{13}$$

Note that Eq. (13) is similar to Eq. (3), which shows that multiple-scale method also gives frequency correction in the solution as in the Poincaré-Lindstedt method.